Transmission-mode Imaging in the Environmental Scanning Electron Microscope (ESEM)

Lech Staniewicz

Churchill College
University of Cambridge

This dissertation is submitted for the degree of
Doctor of Philosophy.

November 2011

Declarations

This dissertation is the result of my own work and includes nothing which is the outcome of work done in collaboration except where specifically indicated in the text.

This dissertation does not exceed the word limit of 60,000 words as specified by the Degree Committee for Physics and Chemistry.

Furthermore, I declare that I have not and am not currently submitting this work for any other degree, diploma or similar qualification from a university or other such place of higher learning.

The data and results obtained from studying *E. coli*, *C. necator*, and *S.* Typhimurium (Chapter 8) have been accepted for publication in Scanning, titled "The application of STEM and in-situ controlled dehydration to bacterial systems using ESEM".

Acknowledgements

This project was funded by the EPSRC (grant number EP/P50385X/1) and by a CASE studentship from FEI Company. It was carried out in the Biological and Soft Systems sector of the Cavendish Laboratory.

The polystyrene-block-polyisoprene copolymers were synthesised, characterised and provided by Dr. Patrick Fairclough of the Department of Chemistry, University of Sheffield. *E. coli* stocks, along with live cultures of *S.* Typhimurium and *C. jejuni* were provided by Dr. Andrew Grant, School of Veterinary Medicine, University of Cambridge. *C. necator* was provided by Nick Thomson, BSS Group, Department of Physics, University of Cambridge.

This thesis is as much a product of my supervisors, Prof. Athene Donald and Dr. Debbie Stokes, as it is of my own. Without their red ink, and that of Andrew Grant for the bacteria chapter, it would be in a very sorry state. I would also like to thank the staff of BSS and the technicians for the Electron Microscopy suite. Without their experience and assistance when things went wrong, I would not have gotten far at all.

Abstract

Electron microscopy was first conducted in the 1930s with the advent of the TEM and later the STEM. In 1969, the first commercial SEM was released, with the possibility of retrofitting it to behave like a STEM following soon afterwards. In 1979, Danilatos and Robinson advanced electron microscopy by creating a new type of SEM which allowed a controlled quantity of gas into the sample chamber, termed ESEM. The most recent evolution in this line was the combination of ESEM and STEM in 2005, a procedure termed Wet STEM.

The focus of this work is on investigating applications of this new technique, along with the contrast mechanisms involved in forming an image. To that end, a wide variety of samples will be imaged. Clay and paint suspensions (colloids) are used to test Wet STEM's capacity to image submerged objects, as well as thin objects which are stacked together. Diblock copolymer films are used to test Wet STEM's ability to distinguish chemically similar materials without staining, the physical effects of heavy metal staining and to demonstrate the necessity of gas for the purpose of charge neutralisation.

Single cell biological samples are also investigated. Internal contrast in mammalian cells is visible without recourse to staining, but chemical fixation is required despite maintaining a high relative humidity. Bacteria are more resilient and as such are easier to image than animal cells, requiring no prior treatment. When exposed to low relative humidity, bacteria are found to collapse. The collapse pattern is observed to differ between wild-type and cytoskeletal-deficient bacteria of the same species and strain, so it is likely that dehydration-induced collapse offers information about the position and shape of the bacterial cytoskeleton.

Contents

List of Figures

List of Tables

Chapter 1

Introduction to Electron Microscopy

1.1 A History of Electron Microscopy

The idea of using electrons instead of light for the illumination and imaging of a sample is not a recent one, first carried out by Knoll and Ruska in the early 1930s when they constructed a machine which was capable of directing and focussing "cathode rays" through an object and on to an emissive phosphor screen. After the publication by de Broglie of wave-particle duality, the importance of using electrons became apparent because of their relatively small wavelength when in motion at any appreciable speed. All microscopes have a fundamental maximum resolving power - the relevant limitation in the case of optical microscopes is that of diffraction, known as the Abbe limit (Equation 1.1) [1].

$$d_0 = \frac{0.61\lambda}{nsin\alpha} \tag{1.1}$$

Here, d_0 is the minimum resolvable separation in an object, λ is the

wavelength of the radiation used to view the object with, n is the refractive index of the medium between the object and the lens and α is the half-angle subtended by the viewing lens at the object. Assuming a wavelength of 550 nm (green light, in the middle of the visible spectrum), a half-angle of 60°(the theoretical maximum is 90°, but this requires an infinitely large lens) and that the microscope is being operated in air (refractive index is very close to 1), this gives a diffraction limit of 390 nm. Immersing the object in oil can improve this slightly - a typical immersion oil will have a refractive index of around 1.5 (Cargille Type A oil has $n = 1.52$), which results in a resolution of 260 nm.

$$\lambda = \frac{h}{p} \tag{1.2}$$

Since electrons at any decent velocity have a wavelength significantly smaller than that of light, diffraction becomes much less of a problem. The wavelength of a particle, as written down by de Broglie, is given in equation 1.2 where λ is the particle's wavelength, h is Planck's constant and p is the momentum of the particle. Neglecting relativistic effects, an electron with 10 keV (1 eV $= 1.602 \times 10^{-19}$ J) of energy will have a speed of 5.93×10^{7} ms^{-1} and a wavelength of 1.2×10^{-11} m, or 0.012 nm, smaller than the size of an atom.

While diffraction is still a problem for electron microscopes, it results primarily from the objective aperture [2] (see Fig. 1.2) with few problems caused by having a wavelength comparable in size to or larger than that of the object to be viewed (high-resolution TEMs being an exception). Instead, the resolution of electron microscopes is mainly determined by other optical factors (such as astigmatism or lens aberrations - see part 1.2.2) which cause the beam to broaden and lose coherence (a factor important for diffraction imaging).

The first electron microscopes were designed in a similar manner to the

best light microscopes of the day - they operated by shining a beam of electrons through a sufficiently thin sample and collecting the transmitted beam. Images were viewed either by the use of a phosphor screen to convert moving electrons into visible light or by photographic plates for image recording. This type of electron microscope has been retrospectively called a transmission electron microscope, or TEM - this is in contrast to other methods of electron microscopy which were developed later.

The next stage of development was the addition of scanning coils to a TEM, carried out by several groups in the 1930s and 1940s [1]. This resulted in the scanning transmission electron microscope (STEM), which worked by collecting scattered and unscattered components of the point beam in a serial fashion as opposed to the entire frame at once approach of a TEM.

There are three types of electron microscope - the TEM, the STEM and the SEM. TEMs operate at high accelerating voltages (on the order of 100 keV, but can reach 1 MeV in very specialised instruments), shine the beam across the entire field of view at once and project the transmitted signal on to a collecting plate; they image samples in a parallel fashion. STEMs also operate at moderately high beam energies (100 keV is common, 200 keV in some instruments), but focus the beam to a fine point and scan it across the sample. They take the transmitted signal, but collect it serially. SEMs operate at lower beam energies (on the order of 10 keV), collect signals from the surface of bulk samples and scan a focussed beam across the sample in the same way as a STEM does.

1.2 The Scanning Electron Microscope

1.2.1 Constructing the SEM

The first commercial scanning electron microscope (SEM) became available in 1964 as the Stereoscan Mk. 1 [1]. Although the basic framework of focussing the beam into a point and raster scanning it across the sample had already been laid out in the form of the STEM, the problem lay in the collection and amplification of secondary electrons (SE, detailed in part 1.3.3) - an important signal for SEM imaging.

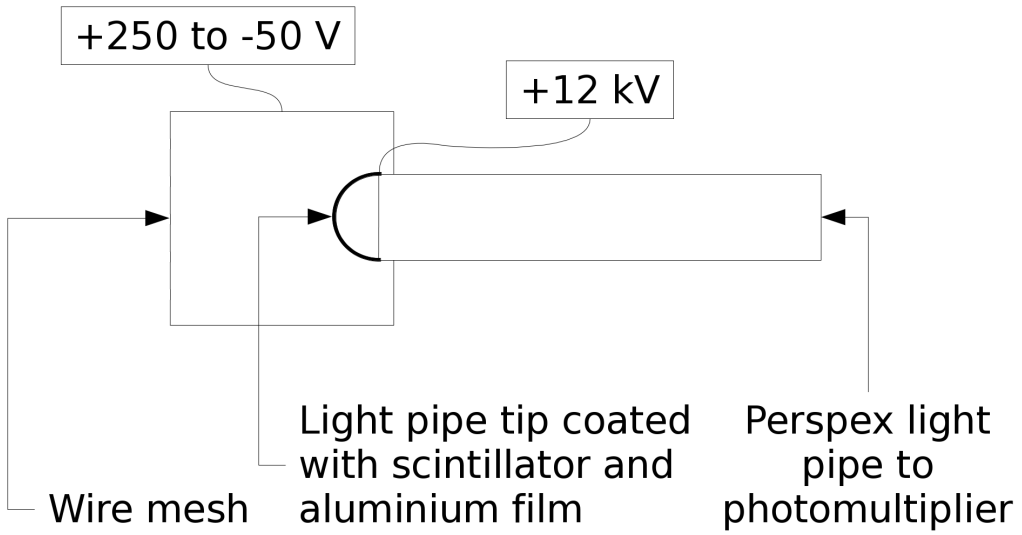

Figure 1.1: Schematic of the important components in the Everhart-Thornley detector. Information from [1].

This was solved by Everhart and Thornley in 1960 [3] who created the type of SE detector which has been used in every SEM since then (Fig. 1.1). It consists of a Perspex light guide capped with a scintillator and a thin aluminium film, placed behind a wire mesh. A selectable bias is placed on the wire mesh to attract or repel secondary electrons towards/from the scintillator and light pipe. Once electrons pass through the wire mesh, they

are attracted towards the scintillator by means of a very high potential on the aluminium film (on the order of 10 kV) - this is to provide collected electrons with enough energy to excite the scintillator. Signal collection is carried out by means of a photomultiplier situated behind the light pipe. This Everhart-Thornley SE detector, as it is known, provides a very good signal-to-noise ratio, thus its inclusion in all modern SEMs.

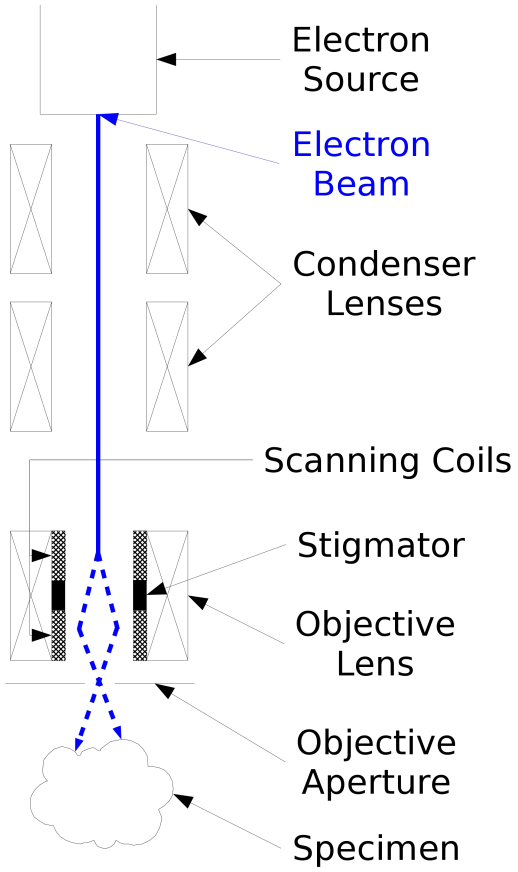

Figure 1.2: Schematic representation of the SEM's electron optics, information from [1]. The path of the electron beam is shown in blue, indicating how scanning using paired coils (part 1.2.2) functions.

Figure 1.2 illustrates the key components in the electron optics of an SEM. Signal detectors are almost always located in the same chamber as the specimen, but they are not shown here. The microscope functions by first generating a beam of electrons at the source - this is detailed further in section 1.2.3. This beam of electrons passes through a pair of lenses (condenser lenses), the purpose of which being to shrink the width of the electron beam. Optically, this is referred to as producing a demagnified

image of the source.

At this point, a compromise between resolution and beam current is made. Due to spherical aberrations inherent to all spherically-symmetric electromagnetic lenses, portions of the beam that pass through the outer parts of a lens are not focussed to the same degree as those passing through the inner part of the lens [1]. By increasing the strength of the condenser lens, its focal length is reduced and the components of the beam which have passed through its outer regions are blanked out either by the objective aperture or by impacting the walls of the electron column. Since spherical aberration serves to change the focal point of a lens into a focal range, rejecting parts of the beam which have propagated through the outer portions of the lens serves to decrease that focal range and thus allow a smaller spot.

However, rejecting the outer portions of the beam will cause fewer electrons to reach the sample. A compromise between signal level (higher beam currents give more signal) and image resolution (lower probe sizes give better resolution) must therefore be found for each sample.

The entire microscope is pumped down to and held at high vacuum for two reasons: firstly, the electron beam will scatter from any gas in the chamber, broadening the probe and reducing its energy. Secondly, the Everhart-Thornley detector presents a 12 kV potential difference hidden from the sample chamber only by means of a wire grid. If any gas were present inside the chamber, it would suffer dielectric breakdown and the resulting electrical arcs would destroy the detector. Vacuum is achieved by means of twin pumping - scroll or rotary vane pumps are used initially to achieve a rough vacuum, then an oil diffusion or turbomolecular pump is connected to the sample chamber via bypass valves and activated to bring the microscope down to operating vacuum - on the order of 10^{-2} Pa for the sample chamber whereas the electron source typically operates at a higher vacuum level (see part 1.2.3).

1.2.2 Scanning, Focussing and Stigmation

Once the source's emission has been demagnified into a smaller beam of electrons, it must then be brought to a focus on the surface of the sample, scanned across the field of view and corrected for astigmatism in the beam. Scanning is carried out by applying a magnetic or electric field across the beam to deflect it - one pair of coils or electrostatic plates is needed for horizontal and one pair for vertical deflection. Most modern electron microscopes use two sets of scanning coils [1] so that the pivot point is in the plane of the objective aperture rather than the middle of the coil - this provides a larger field of view than a single set of scanning coils (see Fig. 1.2).

The electron beam is focussed by means of another lens (the objective lens) like those that comprise the condenser system. If the optics and electron source were ideal, the electron beam would be an infinitely small point in the focal plane. However, this is not the case - the electron microscope is subject to both mutual repulsion of the electrons in the beam and to defects in the optics, both of which serve to spread the beam.

The most prominant of these defects is astigmatism - whereby due to either contamination or imperfect manufacturing, any part of the electron optics have a stronger focal length in one lateral direction than it does in another. This means that the beam will have an elliptical profile except for the one point at which the errors added by astigmatism are equal (known as the disc of least confusion) and it becomes circular once more. Astigmatism is corrected with a pair of magnetic or electric quadrupoles, stacked one on top of the other inside the objective lens (where astigmatism is most important) and rotated by 45° with respect to one another - these serve to laterally compress the beam without altering its trajectory or adjusting its focus.

Finally, the beam passes through the objective aperture (see Fig. 1.2). The purpose of this is to cut off any parts of the beam that are not focussed properly and thus would detract from image resolution. Smaller apertures

give a finer probe size due to removing the improperly focussed components of the beam and a greater depth of field, but allow less current through. They are, however, more susceptible to diffraction effects - a parallel beam passing through a hole and impacting a sample will result in a spot width of $d = \frac{1.22\lambda}{sin(\alpha)}$ [1] (where α is the angle subtended by the hole at the sample) , known as an Airy disc (since the angles involved are so small, we generally take $sin(\alpha) = \alpha$). Operating with a 30 μm objective aperture, a 10 kV beam (with an effective wavelength of 0.012 nm) and an aperture-sample distance of 10 mm results in a diffraction-limited spot size of 10 nm. Note, however, that modern SEMs contain apertures either within or immediately following lenses and as such the entire aperture will not be illuminated - this value therefore overestimates the probe size.

The two main aberrations in electron optics are chromatic and spherical. Chromatic aberration results from electron lenses having different focal lengths for electrons of different energies. The radius of blurring Δr_c of a lens is given by $\Delta r_c = C_c \alpha \frac{\Delta E}{E}$ [1] where C_c is the chromatic aberration coefficient of the lens, α is the angle subtended by the lens at the point of measurement in radians, E is the mean energy of the beam and ΔE is the deviation of the beam's energy from its mean. Chromatic aberration is minimised in practice by having a beam with as low an energy spread as possible - either with a good electron source or with a monochromator.

Such correction is not common on SEMs, however - using a Schottky emitter (part 1.2.3, energy spread 0.3 eV), a chromatic aberration coefficient of 3.4mm [1] and the same microscope parameters used to calculate the diffraction width, we get an error disc which is 0.15 nm across - small when compared to the diffraction-limited spot size.

Spherical aberration is where the focal strength of a lens depends on the distance from the axis of the lens - namely, that rays entering the lens near its edge are focussed more strongly or weakly (depending on the sign of the coefficient) than rays entering near the centre. The blurring Δr_s caused by

spherical aberration is given by $\Delta r_s = C_s\alpha^3$ [1] where C_s is the coefficient of spherical aberration (a separate constant for each lens) and α is again the angle subtended by the lens in radians at the point of measurement.

Using the same microscope parameters as for the diffraction-limited size and assuming a spherical aberration coefficient of 3.5mm [1], we get an error disc which is 0.01 nm across - utterly inconsequential when compared to diffraction. Advanced (S)TEMs will correct spherical aberration with purpose-built devices, but they are not used in SEMs and as such will not be detailed here.

1.2.3 Electron Sources

There are two main types of electron sources - thermionic and field-emission. They differ in the manner by which they produce free electrons - thermionic sources function by heating a material until it starts to emit electrons (by increasing the energy of free electrons to above the Fermi surface of the material) and field-emission sources function by applying an electric field strong enough that electrons are able to quantum-mechanically tunnel out of the emitter in significant numbers.

Thermionic sources were the first ones to be produced. They come in two main types - tungsten filament and lanthanum hexaboride (LaB_6) - both of which have an effective source size on the order of 10 μm. Tungsten filament sources are the cheapest to make and have the lowest vacuum requirements, but their lifetime is relatively poor, their energy spread is quite high and the apparent source size is quite large, resulting in lower resolution. They are fabricated by simply bending a narrow tungsten wire into a hairpin shape and heating it via ohmic resistance. LaB_6 sources are a sharpened crystal of lanthanum hexaboride which is heated indirectly. They require a higher vacuum than tungsten filaments, but give more current (LaB_6 has a lower work function than tungsten), emit from a smaller area (hence give a smaller

probe), last longer and have less energy spread (LaB_6 does not need to be heated as much as tungsten in order to emit electrons).

Electrons are extracted from thermionic sources by means of a positively-biased cylindrical electrode placed in front of the tip. An additional cylindrical electrode is placed between the anode and emitter, known as the Wehnelt electrode. It is negatively biased by a few hundred volts with respect to the cathode and its purpose is both to decrease the source size via electrostatic focussing and to smooth out the emission current.

A field-emission gun (FEG) has a much more strenuous vacuum requirement than thermionic sources do - this is to prevent damage to the tip from ion bombardment. Their advantages are that the apparent source size is much, much smaller (on the order of a few nanometres) and that the emission is much brighter (brightness is measured in units of A m^{-2} sr^{-1}, or current density per unit solid angle). Although they emit less total current than thermionic sources, the current from a field-emitter is confined within a much smaller area.

Since the required electric field is so high (on the order of 10^9 V m^{-1}), field-emission tips are made with incredibly fine points (radii less than 1 μm) so that the highly curved surface serves to enhance the field. Again, there are two types of field-emission sources. The first is known as a cold field-emission source and functions exactly as described above - a sharpened tungsten tip is placed within a high electric field (between 1 and 2 kV), which extracts electrons via quantum tunneling. The second type is a hybrid of field-emission and thermionic sources - the Schottky field emitter. It functions by again using a sharpened tip, but the tip is coated with a very thin layer of zirconium oxide to reduce its work function, and heated to around 1800K. A high electric field is then applied in the same manner as for cold field-emitters - this type would perhaps be more accurately known as a field-assisted thermionic source.

Table 1.1 shows the important points of various sources, information is taken from [1].

	Tungsten	LaB_6	Schottky	Cold FEG
Required vacuum/Pa	$<10^{-2}$	$<10^{-6}$	$<10^{-8}$	$<10^{-10}$
Max. brightness/A cm^{-2} sr^{-1})	10^6	$2x10^6$	10^8	10^9
Cathode lifetime/h	100	600	>2000	>1000
Energy spread/eV	1-2	0.5–2	0.3	0.2–0.4
Source diameter	20–50 μm	10–20 μm	15 nm	5–10 nm

Table 1.1: Some key parameters of the various different types of electron source.

1.3 Beam-Sample Interactions

Each incident electron has a certain probability of colliding and interacting with the sample, governed by its energy and the sample's composition. Beam-sample interactions can be either "elastic" or "inelastic" in nature - elastic collisions result purely in a change of the electron's path, while inelastic collisions result in the incident electron losing energy to the sample (typically with less path change than an elastic collision). Both types of collision can result in usable signals - those most commonly taken for SEM imaging are detailed below.

1.3.1 Back-scattering

The simplest interaction is elastic scattering. This process is well-described for non-relativistic electrons by the Rutherford model (eq. 1.3), where $Q(> \phi_0)$ is the probability of scattering into an angle of greater than ϕ_0 with respect to the initial path, Z is the atomic number of the scattering atom

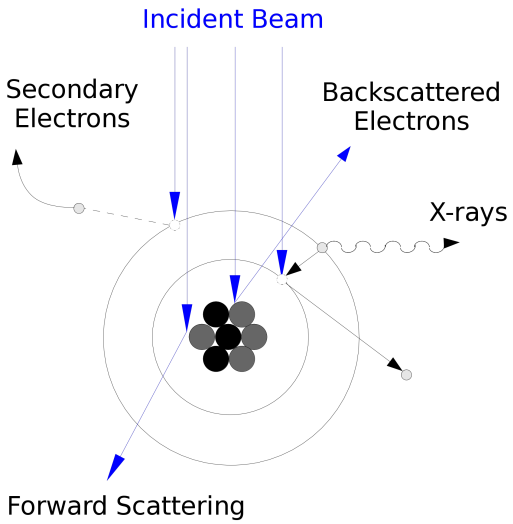

Figure 1.3: Cartoon diagram showing the various types of beam-sample interaction that result in usable signals.

and E is the energy of the incident electron in keV. The result is given in scattering events per incident electron per number of atoms in one square centimetre [2].

$$Q(>\phi_0) = 1.62 \times 10^{-20} \frac{Z^2}{E^2} cot^2 \frac{\phi_0}{2} \tag{1.3}$$

Back-scattering is defined as when an electron emerges from the sample travelling more than 90° from it's initial path. By convention, an electron is classified as "back-scattered" if it has more than 50 eV of energy after escaping the sample surface - this is to distinguish it from secondary electrons (section 1.3.3). From equation 1.3, we can see that higher atomic number elements will scatter more strongly. The nature of a backscattered signal is therefore to provide strong compositional contrast and the signal comes from a region between the surface and 30% of the total electron penetration depth [2].

Backscattered electrons (BSE) are typically collected using a photodiode positioned above the sample, but scintillator, lightpipe and photomultiplier combinations have also been used when the improved response time and dynamic range of a photomultiplier is deemed worthy of its extra cost and com-

plication over a simple semiconductor crystal. To provide additional imaging modes, backscatter detectors are often split into multiple independent segments - if the sample topography prohibits electrons from escaping in certain directions, topographic contrast can be obtained by taking one segment only or by taking the difference between segments as the imaging signal.

1.3.2 Forward Scattering

While there are several ways for an incident electron to emerge from the sample travelling in the opposite direction to the beam, equation 1.3 shows that it's more likely for an electron to scatter through a small angle. If the sample is sufficiently thin, most of the beam will go straight through and out the other side - this is the basis of TEM imaging. As with the backscattered signal, higher atomic number elements will scatter more strongly.

Forward-scattered electrons (elastic collisions generally result in a greater path deviation) are collected in a number of ways - in a TEM, they are typically passed through more lenses and apertures, then imaged using a phosphor screen which is either exposed for viewing or coupled to a CCD camera via optical fibre bundles. In dedicated STEMs, they are most commonly collected using a scintillator-photomultiplier combination.

Electrons can lose energy by interacting with atoms and either ionising or exciting them. Due to their quantum nature, each element has a defined set of allowed excitations which can leave a "fingerprint" on the transmitted beam in the form of an energy loss. Some STEMs are equipped with energy filters which can record this data, a technique known as Electron Energy Loss Spectroscopy (EELS).

1.3.3 Secondary Electrons

Secondary electrons (SE) arise from an inelastic process which occurs when incident radiation collides with a sample electron and knocks it free of its atom. Most secondary electrons are produced and escape from the sample with an energy of around 5-10 eV, but in practice the energy range of SEs goes up to 50 eV, which marks the lower bound of the BSE energy range.

Because of their low energy, SEs are only able to escape from a very small depth (less than 50 nm [2]) inside the sample before being absorbed - this means that since the beam has not had a chance to spread out before generating them, the SE signal offers a resolution potentially limited only by the probe size. As mentioned earlier (section 1.2.1), SEs are collected using an Everhart-Thornley detector. The SE signal is by far the most commonly used signal when operating an SEM because of its surface sensitivity and resolution.

Tilting the sample will alter the amount of secondary electrons produced. Steep angles result in a higher emission (Fig. 1.4), making edges appear brighter than flat surfaces. The quantity of secondary electrons emitted scales with $\frac{1}{cos\theta}$, where θ is the angle between the surface normal and the incident beam. Because of this, the SE signal exhibits strong topographical contrast.

The presence of electric fields on the sample surface will also serve to provide contrast in secondary electron imaging. Negatively-charged surfaces will serve to repel SEs away from the sample, increasing the signal. The converse is true for positively-charged surfaces, which will attract free electrons back towards the sample. Electric fields can be inherent to the sample (such as semiconductor junctions) or created when insulating samples charge up under electron irradiation.

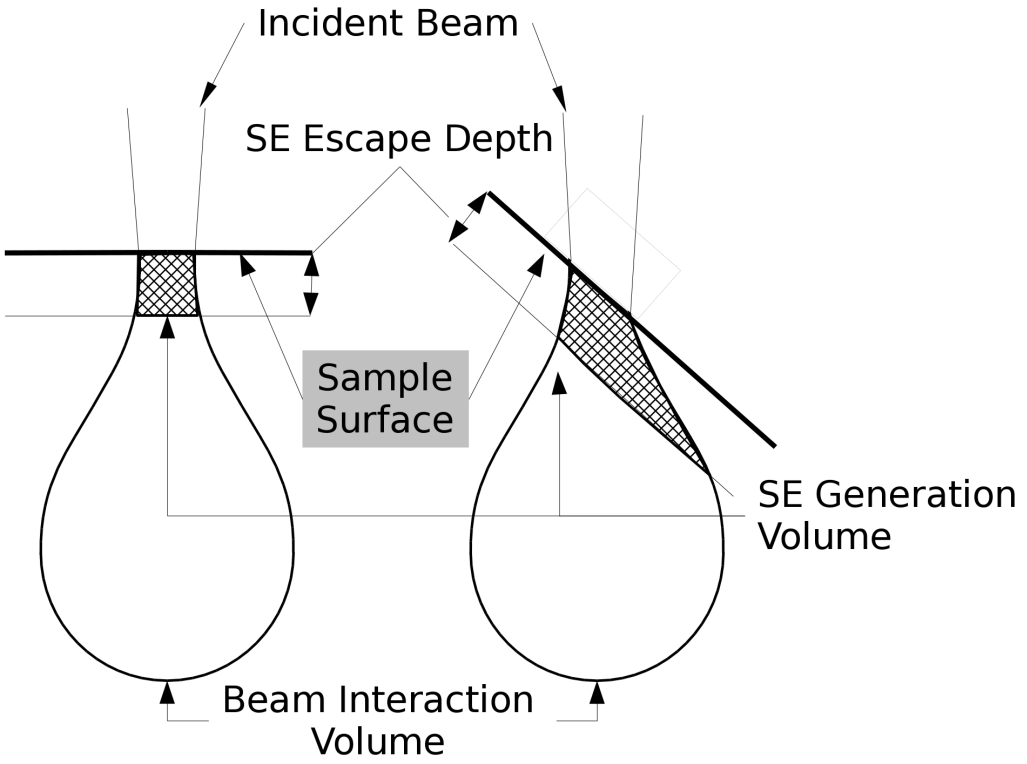

Figure 1.4: Schematic of the effect sample tilt has on SE emission. Shown are one sample which lies perpendicular to the beam (left) and one sample whose normal lies at an angle (right). The angled sample has more interaction volume within the SE escape depth and so emits more secondary electrons. Diagram is not to scale.

1.3.4 X-ray Emission

If an incident electron is able to remove a core electron from an atom, one of the electrons in a higher shell will "jump" down and fill the vacancy. Since there is a significant energy difference between electron shells, the atom will radiate a photon during this transition - having energies of 52 eV at the least (Lithium), these photons are classed as x-rays. Since x-rays have significant penetrating power when compared to an electron beam, any that are generated can escape from the sample - this means that as the beam spreads

out (Fig. 1.5), they will be generated from a larger volume and consequently exhibit poorer resolution.

The energy differences between electron shells are different for each element. This means that each element will give off a unique radiation pattern, allowing spectroscopy to be performed on the sample with a suitable detector. X-rays are detected with two main methods: wavelength-dispersive spectroscopy (WDX) and energy-dispersive spectroscopy (EDX).

WDX is carried out by placing a crystal and a Geiger counter in the sample chamber and angling the crystal so that only one wavelength of radiation can reflect from it into the Geiger counter via Bragg scattering. WDX is very precise in terms of wavelength discrimination, but each crystal will only function for a small range of wavelengths and sweeping them is time consuming.

EDX is carried out by placing a semiconductor detector in the sample chamber and connecting it to a pulse counter. Incoming x-ray photons strike the semiconductor and create electron-hole pairs which are counted by the amplifier. Since the number of pairs is directly proportional to the energy of the photon, this provides an easy method of determining the emission spectrum. EDX samples the whole frequency spectrum at once and so is faster than WDX, but the energy resolution is poorer and it is susceptible to artefacts from multiple photons arriving at once.

Because the generation of x-rays is well defined and understood, the emission spectrum can be used to quantify the relative proportions of the elements present in a sample. There are several methods of doing this; a more detailed explanation can be found in the book by Goldstein et al [2].

1.3.5 Beam-induced Sample Damage

Electron beams are a form of ionising radiation - in traditional terms, they would be known as beta rays. Electron radiation can damage samples in a number of ways:

Heating:

At the most basic level, pumping energy into a sample will cause a temperature rise. Because the electron beams used in SEMs are finely focussed, the energy is concentrated across a very small area. If the sample is unable to conduct away this extra heat, it can locally melt, boil or cook (in the case of biological specimens).

Ionisation:

Beam electrons can remove sample electrons from their atoms via collision. In conductive, regular samples, such as metals, this is not much of a problem since an electron can just flow in from elsewhere in the metal and replace it. Some heat will be produced as the metal electron falls into the vacancy produced by ionisation, but this will be conducted away. However, insulating samples may not be as resilient - organic materials in particular are subject to two additional consequences of ionisation (more detail from [4]):

Scission: this is where a linking atom or side group in one of the sample's carbon chains is ionised and disconnects from its original partner. Where there was once one long chain, there are now two shorter ones - these are more likely to dissociate from the sample under the vacuum present in the microscope. Chain scission is a cause of mass loss under irradiation in the electron microscope.

Crosslinking: this is where a carbon chain in the sample either has a side atom ionised or a double bond on its main chain broken into a single and two free valence electrons. Both of these are reactive species and will bond to neighbouring chains upon formation.

Recoil:

Heating and ionisation are both caused from electron-electron interactions. When an incident electron instead transfers energy to the nucleus of a sample atom, that whole atom will move. With sufficient energy, that atom will break its bonds and move about - causing either dislocations in crystal structures or sputtering if the atom is knocked free of the sample. Because there is so much mass difference between electrons and atoms, providing even a few eV of kinetic energy requires electrons to have an energy on the order of 100 keV. The effect is therefore more prominent in (S)TEMs, where beam energies are sufficiently high.

Also of importance to the microscopist is that of beam scattering and broadening inside the sample. Through a variety of interactions, beam electrons will be deviated from their initial path. The end result is a broad, pear-shaped interaction volume (fig. 1.5), something which has consequences for the resolution of the various emitted signals (detailed in their respective sections).

A higher beam energy or lower atomic number sample will result in the interaction volume being elongated and widened. If the sample is thin enough, the wider portion of the interaction volume will be out of the sample and so the effective resolution will increase. Conversely, a lower beam energy or higher atomic number sample will shrink the interaction volume and move more of the interactions to the surface, resulting in a more spherical interaction volume. Thick samples being imaged under SEM will usually benefit from a lower beam energy, which exhibits the dual advantages of a smaller interaction volume (thus higher resolution) and a stronger secondary electron signal, because more of the interaction volume will be within the secondary electron escape depth.

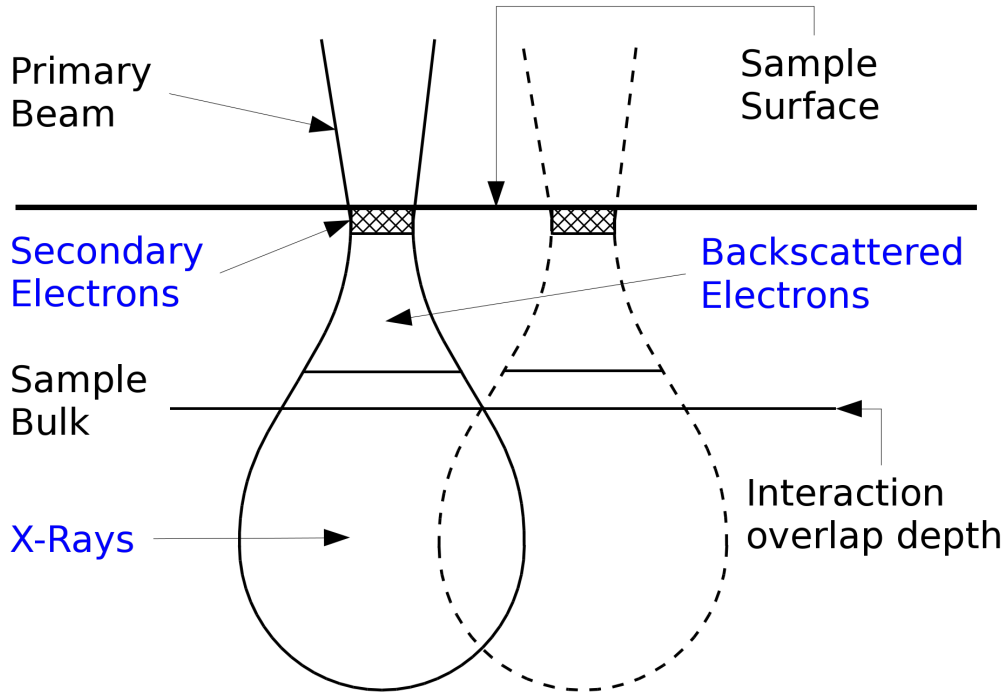

Figure 1.5: Schematic of the broadening an electron beam undergoes when it encounters a sample. Indicated are the depths where various signals (blue text) generated from inside that interaction volume can escape from. Two such beams are placed next to each other to represent scanning across a sample. When the sample is thick enough and/or adjacent scanning points sufficiently close (for instance, at high magnification), some types of signal will be generated from the same volume, causing a decline in resolution - this is indicated by the interaction overlap depth.

1.4 Sample Preparation Techniques

Because not every sample is conductive (for the SEM) or thin and with a large inherent difference in atomic number (for usage with a (S)TEM), further preparation may be required before imaging can be carried out. In addition, wet samples such as biological material may also need to be dried out before use to prevent their stored water from ruining the microscope's vacuum.

Drying can be carried out in a number of ways - freeze-drying, where the sample is frozen and the water allowed to sublimate in a low pressure environment, critical-point drying, where the sample is heated under pressure to above the critical point of water - this allows the removal of water without a potentially damaging liquid-solid interface, or simply by heating up the sample and driving off the water directly.

Making a sample conductive is used mainly for the SEM, where the charging of bulk samples becomes problematic. It is usually carried out by applying a coating of carbon or metal to the sample's surface with an evaporator or sputter coater. Metal coating also has the advantage of increasing the sample's stopping power with respect to the electron beam, allowing for finer resolution (see Fig. 1.5) due to a shrinking of the interaction volume.

(S)TEM sample preparation involves making a section of the sample thin enough to be electron-transparent - this can be carried out for hard mineral specimens by thinning a bulk sample with a dimple grinder and then finishing off with either electropolishing (which is essentially electroplating operated in reverse) or by using an ion mill to sputter away portions of the sample. Soft specimens are typically dehydrated first, then embedded in resin and thin sections cut directly with a microtome. Alternatively, a focussed ion beam can be used to directly cut out a region of interest.

Low atomic number samples are often stained by use of heavy metals to enhance the contrast - this can be carried out with broadly reactive chemicals (such as osmium tetroxide, which attacks unsaturated carbon-carbon bonds as found in cell membranes or some polymers) or selective staining with antibodies, in the case of biological material. Antibodies suitable for TEM imaging will be attached to gold nanoparticles to provide atomic number contrast, as opposed to the fluorescent labels used in light microscopy.

Because sample preparation is such a broad subject and is covered in great detail elsewhere [4, 1], it will not be given a thorough coverage here.

Chapter 2

Introduction to Environmental SEM

2.1 History and Purpose of the ESEM

While there are well-established methods of sample preparation which can allow almost any sample to be imaged in the SEM, these steps are destructive in nature. Because it will alter their appearance, historical artefacts such as pottery fragments (for instance) would not be given a metal or carbon coating, even if it is required to eliminate charging artefacts. Fragile biological materials will often suffer damage from a dehydration procedure, collapsing and warping due to loss of turgor pressure.

Because the total emission of electrons from the sample (both secondary and backscattered) is a varying function of beam energy [1], the accelerating voltage on the microscope can potentially be adjusted so that the input current precisely balances the sample's electron emission. This will eliminate charging, but removes the free choice of beam energy (higher energies may be required to excite x-rays for heavier elements, for instance). Furthermore,

any topographical or electrical inhomogeneities in the sample will still be subject to charging because of the locally different secondary electron yields.

One possible way of avoiding artefacts from dehydration is to freeze wet samples rapidly enough so that amorphous ice is formed. By doing so, the sample's outer structure will retain its shape (inner portions will be damaged when ice crystals form, since their rate of freezing will be lower). The frozen sample can be mounted on a cryogenically-cooled stage inside the SEM to both preserve the sample and prevent evaporation from damaging the microscope, then imaged normally. The drawbacks to cryo-microscopy are three-fold: firstly that ice crystals will still form inside the sample when the rate of cooling is too low to prevent their growth, so the interior of a wet sample will still be damaged; secondly, that specialised equipment is required to maintain cryogenic temperatures inside of an SEM; thirdly, that the temperature control is not perfect and as such there will be drift from thermal expansion and contraction.

The first steps toward alleviating these problems were taken in 1979 [5], when Danilatos and Robinson employed a system of pressure-limiting apertures and differential pumping to allow samples to be imaged in the presence of an atmosphere. They termed their system an "environmental scanning electron microscope", or ESEM. With a sufficiently high pressure of gas in the sample chamber, the sample could essentially be kept in its native state all the time and as such wouldn't need any preparation in the first place. Furthermore, the electron beam will ionise any gas it touches - the resulting ions will be attracted to any regions which exhibit an opposite electric charge and negate any charging artefacts that would otherwise be caused.

The first published use of the ESEM was on wool fibres [6], when Danilatos also demonstrated the ability of the instrument to work at atmospheric pressures. Due to various technical constraints, commercial ESEMs work at lower pressures than full atmospheric, the upper limit of FEI Company's (the trademark holder for ESEM) instruments being at 20 Torr (2666 Pa).

Other manufacturers have also released SEMs with the ability to allow some level of gas inside the sample chamber - known broadly as "variable-pressure SEM" or VP-SEM. The cut-off for calling something an ESEM is generally defined as the instrument having the capability to sustain liquid water - the minimum pressure required is therefore 4.5 Torr (600 Pa) at 0°C.

Since then, ESEM has been used for a multitude of different samples - oil-water emulsions [7], bread dough [8], tooth decay [9], wet cement [10] and the surface structure of unfixed cells [11]. ESEM has also been used to image active processes and systems, such as a freeze-drying process [12], catalysis reactions [13, 14] and the closure of stomatal pores in plant leaves [15].

Although any gas can be allowed into the ESEM (barring chemical attack on the microscope's internal components), the most commonly used one is water. This is from a combination of factors: it is non-toxic, readily available, provides good signal amplification (see part 2.5.1) and it can be used to keep wet specimens hydrated (see part 2.3).

2.2 Construction of the ESEM

The environmental SEM is very similar in construction to a conventional SEM - it has the same key components of an electron source, some demagnifying lenses, scanning coils and a focussing lens. The key differences lie in the addition of pressure-limiting apertures to stop gas from interfering with the electron source and beam propagation. Furthermore, the methods of signal detection inside the ESEM differ from those in conventional SEM - this is detailed in part 2.5.

ESEM is made possible by the use of differential pumping. Because the difference between the operating vacuum of an electron gun (10^{-5}–10^{-8} Pa, depending on the source type) and the pressure in the sample chamber (660 Pa for liquid water at 1°C) is so large, a single pumping stage will not be

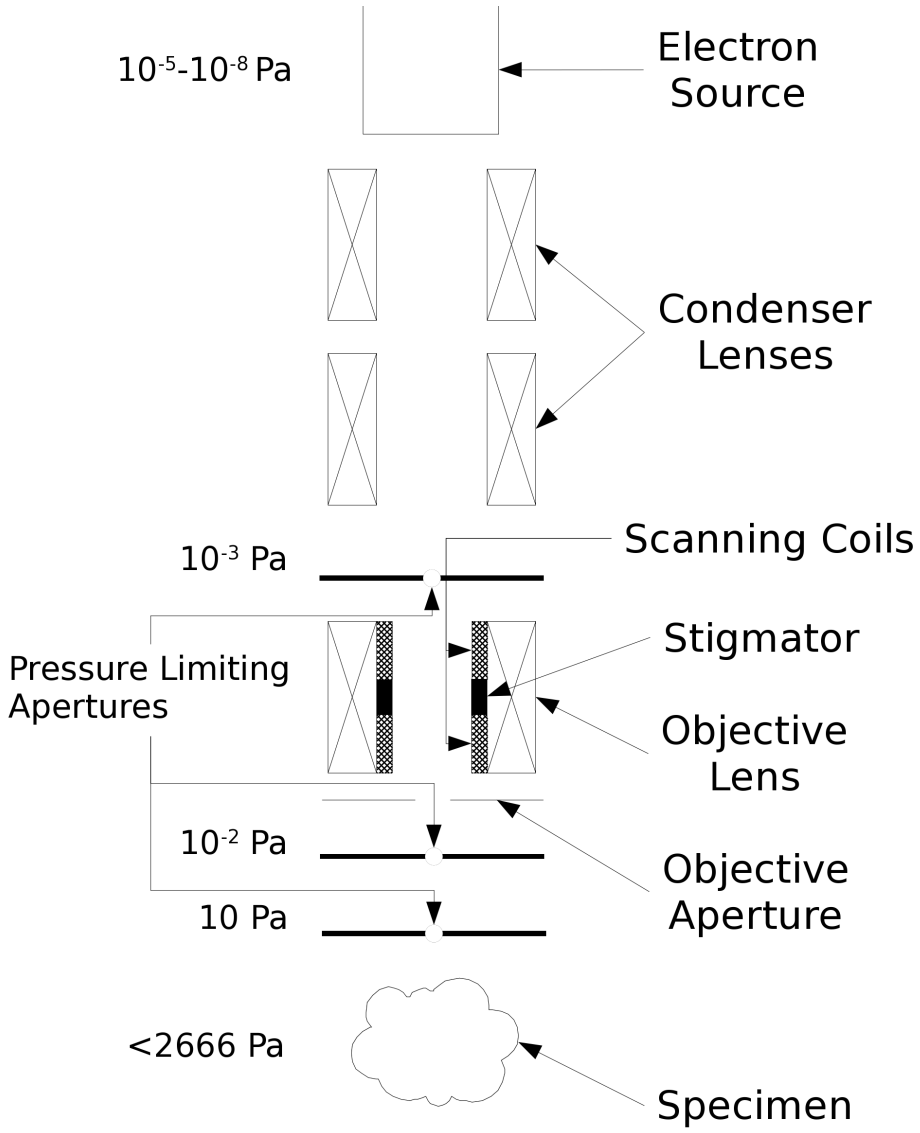

Figure 2.1: Schematic representation of the ESEM's electron optics, information from [16]. Note the additional pressure-limiting apertures when compared to Fig. 1.2; The approximate pressure in each region of the microscope is listed alongside it.

able to handle it. Instead, several pressure-limiting apertures (PLA) are installed inside the microscope column and additional pumping stages are added between them.

Figure 2.1 illustrates this. The sample chamber can hold up to 2660 Pa of gas and contains an inlet for this gas (some microscopes have two - one for water and one for an auxiliary gas). The first PLA is located at the point where the beam enters the chamber and is usually 300 or 500 μm in diameter. Directly above this first aperture is a second PLA, also 300 μm in diameter. The space in between the two is connected to a vacuum pump, reducing the pressure in this particular region to something on the order of 10 Pa.

This system of multiple apertures and pumps continues all the way up the column; each stage slowly decreasing the pressure inside the electron optics system. As the vacuum level increases, the type of pump changes - at the high-pressure regions, conventional rotary or scroll pumps are used. Above the second pressure-limiting aperture, diffusion or turbomolecular pumps can be found to provide higher vacuum levels. At the top, just below the electron gun, ion getter pumps are used to provide the very high vacuum required for the electron source to operate.

The advantage of using multiple stages like this is that after each stage, there is a sharp drop in pressure due to the confining aperture and additional pump. This effectively confines the gas to the bottom of the column so that the beam will interact with as little gas as possible before it reaches the sample. Scattering and the resultant loss of resolution is thus minimised. A thorough description of the ESEM's pressure system was published by Danilatos [17]; more information can be found there.

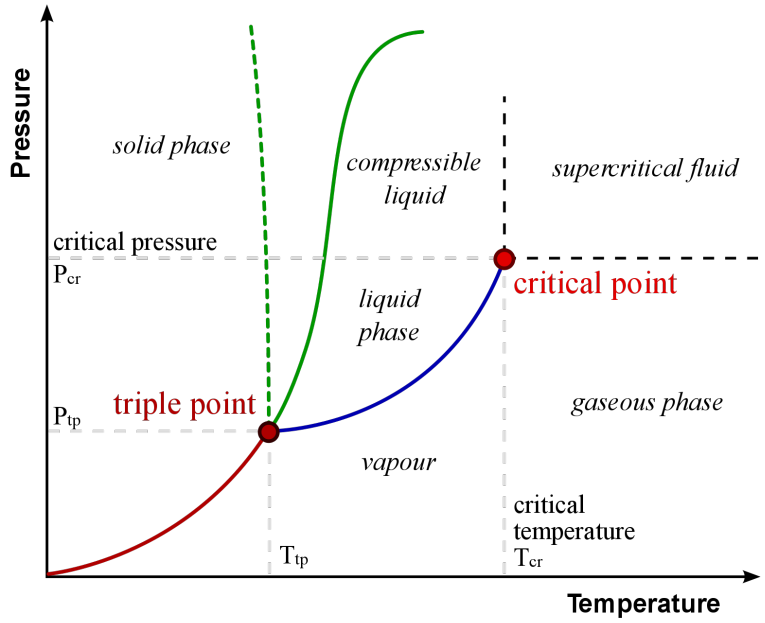

Figure 2.2: A generic phase diagram, with the dotted green line indicating water's anomalous behaviour around the liquid-solid interface (numerical values are not shown). Image sourced from [18].

2.3 Keeping Samples Hydrated

Pressure is only one part of the environmental control mechanism. To choose between liquid, solid and gas, the temperature must also be set, the exact values given by a phase diagram such as that in Fig. 2.2.

By varying the pressure and temperature at the sample, it can theoretically be maintained in any state. Practical constraints limit the range of temperatures and pressures available to the microscopist - the pressure cannot be raised above 2660 Pa in modern ESEMs and each sample stage has a limited range of allowed temperatures.

A water-cooled Peltier stage is the most commonly used way of keeping wet samples hydrated. They are capable of maintaining a chosen temperature

in the range of -25°C–55°C [19], sufficient to create solid, liquid or gas forms of water through the entire pressure range of the ESEM.

The most important parameter when imaging wet samples is the relative humidity, defined as the ratio between the partial pressure and the vapour pressure of water for the current temperature of the environment. Relative humidities which are less than 100% will cause evaporation of water, while above 100% implies condensation. To keep a sample wet, it should be imaged at exactly 100% relative humidity.

Hydrophilic surfaces, due to their affinity for water, will experience condensation at relative humidities of less than 100% and as such can be imaged at a slightly higher temperature or lower pressure than the chart in Figure 2.3 would indicate. In practice, samples are usually imaged at less than 100% relative humidity to ensure that water does not condense on the region being imaged and hamper image quality.

Note that although the microscope can pump down to and sustain any given pressure within its operating range, the composition of the gas will not necessarily be pure water. Upon the initial pumpdown, the microscope chamber will be filled with low-pressure air, the partial pressure of water will be relatively low and hydrated samples will start to dry off. This can be alleviated by two methods: the first of which is to place droplets of water alongside the sample before pumping down the microscope. These droplets will evaporate as the pressure is reduced (if they are not cooled, they will evaporate in preference to the sample's own water), contribute water vapour to the chamber atmosphere and consequently slow the evaporation of sample water [20].

The second method involves purging the microscope via a sequence of controlled pressure drops and increases [21]. By dropping the pressure by a small amount then raising it to a higher level by use of the water vapour inlet, the partial pressure of water is steadily increased up to the required

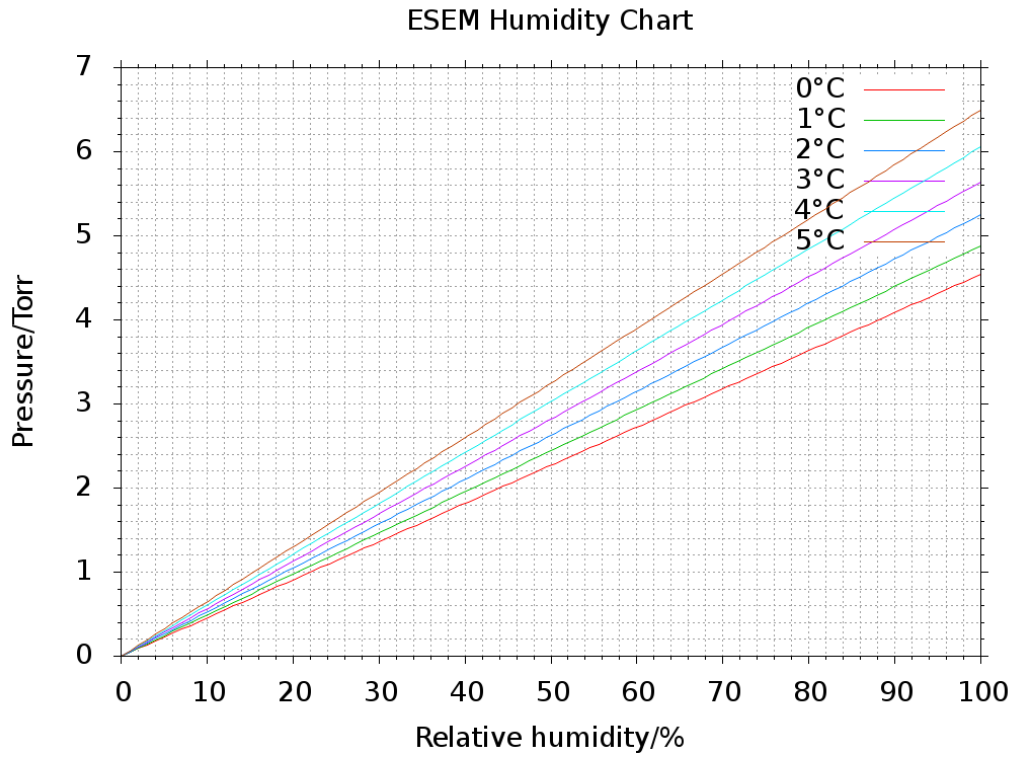

Figure 2.3: A plot of relative humidity against the partial pressure (1 Torr = 133 Pa) of water for six different temperatures.

value. Provided that the sample temperature remains low enough and that the upper and lower purge limits are both high enough, a droplet of liquid sample can be placed inside the microscope and still remain when the purge procedure is complete and the electron beam is activated.

One additional advantage of ensuring a pure water atmosphere is that water provides for better amplification [22] of the secondary electron signal (see part 2.5.1) than nitrogen (or air).

2.4 Detrimental Effects of Gas on the Microscope and Sample

2.4.1 Beam Spreading

Aside from danger to high-voltage components, the most important issue raised by having a gas inside the microscope is that it will interfere with the propagation of the electron beam, causing it to scatter and lose energy.

The amount of scattering experienced by the beam is directly proportional to the quantity of gas through which it must travel. While the system of multiple apertures and pumping stages helps keep the gas as far away from the electron source as possible, the beam will inevitably travel through some amount of gas when it enters the sample chamber.

Each individual scattering event will divert one electron from its original path. Providing that there are fewer scattering events than electrons present in the beam (each electron may scatter more than once), the overall profile will consist of the central core formed by what remains of the unscattered beam overlaid upon a large "skirt", comprised of all the scattered electrons (see Fig. 2.4). Since the "skirt" is dispersed over a relatively broad area (several microns, according to [23]), its contribution is that of an effectively constant background signal. This is referred to as the oligo-scattering regime. When the beam encounters sufficient gas such that all the electrons scatter, the net result is a broad spread of electrons instead of a fine probe - this is the multiple-scattering regime.

The quantity of gas in the path of the beam depends primarily on two things: the pressure in the final chamber (since the first PLA-pump system drops the pressure by a factor of a hundred, conditions inside the column will not be considered) and the distance between the first PLA and the sample, known as the gas path length (GPL). Note that the GPL is distinct from the

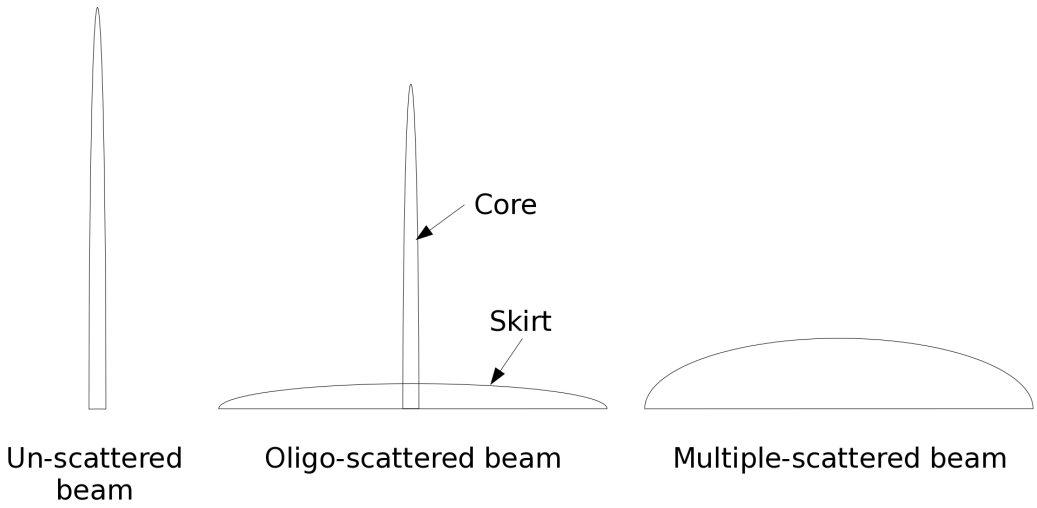

Figure 2.4: An illustration showing plots of intensity against radius (not to scale) for an unscattered beam, an oligo-scattered beam and a multiple-scattered beam.

working distance, since some apertures extend past the polepiece.

By using as low a pressure and as short a GPL as possible, beam spreading can be minimised. In order to keep wet samples hydrated at low pressures, a low temperature must also be selected (Fig. 2.3) - hence the use of a Peltier-controlled stage. Shorter GPL can be achieved by bringing the sample closer to the first PLA; usually by raising the sample stage. Specialised PLAs can be found when the working distance between the polepiece and the sample must be a fixed quantity (such as in EDX analysis) - these come in the form of cones that attach to the bottom of the objective lens assembly.

2.4.2 Sample Damage

Because ions are generated from the imaging gas by both incoming and emitted electrons (see part 2.5.1 for a more detailed explanation), another avenue of sample damage is opened. The reactive species produced will have dif-

ferent effects on different samples - ceramics and metals are usually quite resistant to chemical attack, while polymer or other carbon-based samples can be damaged by both direct irradiation and reactive chemicals [24, 25, 26].

The choice of imaging gas also plays a role in sample damage. Water, the most common imaging gas, has the capability to produce several different types of reactive species [26] under irradiation. When combined with a susceptible sample, such as polymeric or biological material, etching can occur.

However, etching may have beneficial effects. Contamination of sample surfaces is a known problem in electron microscopy; oil leakage from the vacuum system [1] being one of its many causes. The production of reactive species from the imaging gas can in fact serve to remove contaminant layers [27] and provide a "cleaner" image.

2.5 Signal Detection in the ESEM

2.5.1 Secondary Electrons in the ESEM

Although the mere presence of gas inside the chamber does not stop the generation of secondary electrons (it will, however, absorb them if left undisturbed), the Everhart-Thornley detector cannot be used inside the ESEM due to the detector's high electric field. Since secondary electrons are such an important part of SEM imaging, another method of collecting secondary electrons had to be devised to bring ESEM signal detection up to the same standards as conventional SEM.

To get around this, Danilatos devised a method which involved using the gas in a signal amplification mechanism [17]. An electrode exhibiting a moderately high voltage (the maximum is about +600V on the FEI XL30 ESEM)

is installed within the sample chamber and connected to an amplifier. Secondary electrons are accelerated towards this electrode and will ionise gas molecules upon collision once they gain sufficient energy. The electrons released from such ionising collisions are also accelerated towards the electrode, creating more current in an amplification cascade.

The final current collected by the electrode is taken as the imaging signal. The level of amplification is determined by the accelerating voltage on the electrode (and hence how quickly an electron gains enough energy to start the next level of the cascade), the distance from the detector to the sample and the chamber pressure (both of which determine how many gas molecules are available to cause amplification).

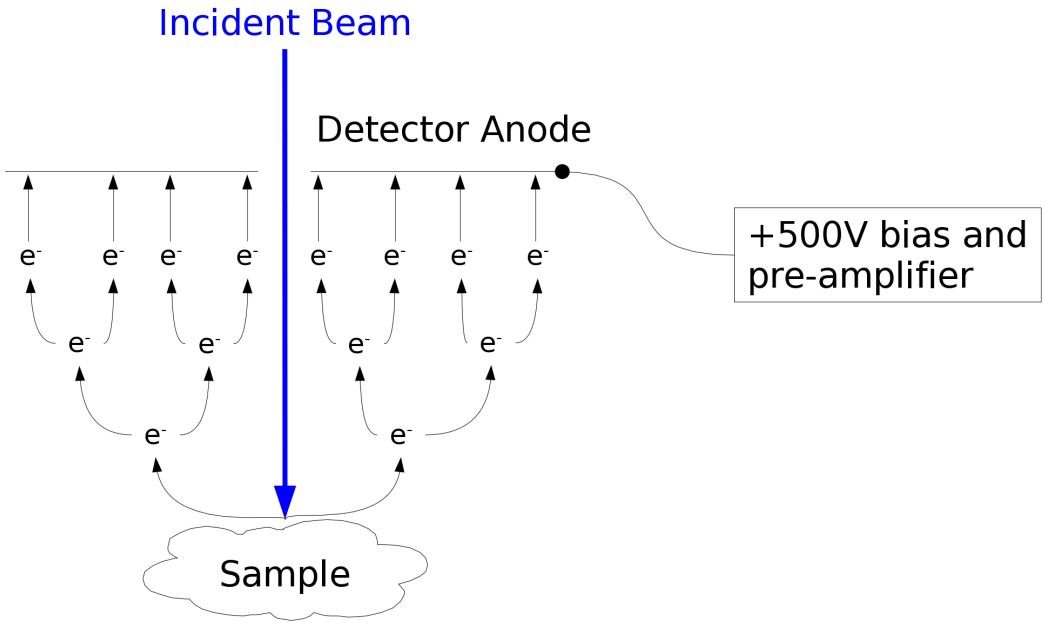

Figure 2.5: An illustration of the amplification cascade present when using an electrode-based secondary electron detector in the ESEM.

The detecting electrode itself was originally a metal cone which also served as the first pressure-limiting aperture, called the Environmental Secondary Detector (ESD). Later developments resulted in the Gaseous Secondary Elec-

tron Detector (GSED), which consisted of a thin metal ring suspended below a metal pressure limiting aperture and the needle detector [28], which consists of a finely pointed anode which can be positioned freely inside the sample chamber (hence making the anode-sample distance independent of the gas path length).

The exact differences in operation between the ESD, GSED and needle detector will not be discussed here. The GSED is described in more detail in [16], while the needle detector is detailed in [28]. To summarise, the advantage of the GSED is that its signal contains a larger secondary electron component with respect to the backscattered electron component than the ESD. The needle detector has the same advantage, but also provides higher amplification for the same anode bias and decouples the gas path length from the anode-sample spacing (and hence the amplification distance).

There are trade-offs to be made when choosing detector parameters. While increasing the electrode voltage will increase the signal amplification, too high a voltage will cause arcing in the microscope chamber, disrupting the image and potentially damaging the equipment and sample. Placing the detector further away from the sample can increase the level of amplification, but will cause lag in the signal as the electrons are repeatedly slowed by gas collisions, causing streaking on the image. Increasing the chamber pressure will scatter and broaden the probe, decreasing contrast.

Additionally, the ionisation cascade creates a large quantity of positive ions. Provided that the sample charging would ordinarily be net negative (it emits fewer secondary and backscattered electrons than the beam provides), these ions will drift down to the sample and neutralise any charging that might occur otherwise. An excess of ions can actually cause charging artefacts, but this can be corrected with the appropriate equipment [29].

2.5.2 Backscattered Electrons in the ESEM

Because backscattered electrons have energies close to that of the primary beam (several keV), backscattered electrons should be able to collide with a molecule of imaging gas and not be deviated through too great an angle. Since backscattered electron detectors do not monitor a fine probe but an overall signal, the backscattered electron signal will therefore be usable as it is.

When the ESEM was first described, the ESD had not been invented and so backscattered electrons were used to form the imaging signal [6]. Since none of the backscattered electron detectors used to date involve high voltages inside the microscope chamber, no modification was necessary. Danilatos and Robinson used a plastic lightpipe coated with a scintillator to detect backscattered electrons. When connected to a photomultiplier, the system is similar in principle to that of the Everhart-Thornley detector and as such shares its high gain and response rate.

The disadvantage of this method is that the whole assembly is quite bulky, meaning that the sample cannot be tilted through the whole range afforded to it by the stage. Just as for the high-vacuum SEM, a semiconductor detector can also be used if space is at a premium inside the sample chamber.

2.5.3 X-rays in the ESEM

When samples acquire an electric charge, the landing energy of the electron beam will be altered by the resulting electric field. Since the yield of any particular x-ray is dependent on the energy of the incident electron [30], any charging of the sample will make it difficult to quantify x-ray emissions and hence the sample composition.

Insulating samples are therefore difficult to run quantitative x-ray analysis

on. Because x-rays cannot be excited with an energy greater than that of the electron beam, it is usually not possible to choose a beam energy at which charging is minimised. The usual solution is to coat the sample with a conductive material, but this will generate a signal of its own (which can interfere with sample signals) and can absorb part of the beam.

The ESEM's charge neutralising ability removes this problem, but introduces a few of its own. Firstly is that the imaging gas will generate its own x-rays [31]. Although the emission rate is low compared to that of a solid sample, they can make a sample appear to have elements which it does not contain.

Secondly is the effect from the electron skirt. When mapping elements with the x-ray signal, the skirt will excite x-rays at locations quite distant from the point of impact of the beam [31]. This additional background signal is, by comparison, more important for EDX analysis than for imaging

Chapter 3

Wet STEM

3.1 STEM in the SEM

Although dedicated STEMs are constructed more like a TEM than an SEM (for instance: they normally operate at higher accelerating voltages, with better optics and with a cleaner vacuum [1] for the purpose of high-performance imaging and spectroscopy capabilities), the forward-scattered beam (see part 1.3.2) can still be taken as an imaging signal when using an SEM.

This procedure is not new, having been first described in 1969 [32], very shortly after the SEM's debut. Contrast in STEM arises when parts of the sample scatter the beam differently. As already stated in equation 1.3, this is primarily caused by changes in atomic number but can also arise from variations in mass-thickness.

The use of STEM, when compared to backscattered electron imaging, is greatest when samples are sufficiently thin such that there is no overlap between the interaction volume at adjacent scanning points (see Fig. 1.5). In this situation, the theoretical resolution of both techniques will be similar. Since electrons are more likely to scatter forwards than backwards, however,

such a sample will give stronger signals in STEM than with BSE (and therefore will have a higher effective resolution in STEM due to the improved signal-to-noise ratio).

Most SEM manufacturers nowadays offer STEM attachments for their instruments. While this technique is not ubiquitous, it is fairly well known - having been used to study (for example) nanoparticles [33], dopant profiles in semiconductors [34] and even the shape of an electric field [35].

3.1.1 Contrast Mechanisms

Contrast, in all forms of transmission electron microscopy, is determined by how much of the transmitted beam gets collected. The sample will either absorb the beam, reducing its intensity; or scatter the beam away from its original path, causing it to miss an appropriately shaped detector. A TEM offers the additional possibility of using the sample to diffract the electron beam - such procedures can be carried out with parallel or converging beams and take advantage of TEM images being presented as an entire 2D plane at once (as opposed to the serial linescans of an SEM or STEM), but they will not be elaborated on here.

The most important source of contrast is that of scattering. STEM instruments have historically been equipped with detectors for both unscattered (bright-field) and scattered (dark-field) beams, collecting the dark-field signal from an annular region around the bright-field detector [1]. Electrons scatter primarily from dense accumulations of charge, such as atomic nuclei and core shells. The net scattering power is given by adding two more terms to Rutherford's elastic scattering equation (see also Eq.1.3):

$$Q(>\phi_0) = 1.62 \times 10^{-20} nl \frac{Z^2}{E^2} cot^2 \frac{\phi_0}{2} \tag{3.1}$$

$Q(> \phi_0)$ is the probability of scattering into an angle of greater than ϕ_0 with respect to the initial path, Z is the atomic number of the scattering atom and E is the energy of the incident electron in keV. The new terms here are n, which is the density of the material in atoms per unit cubic centimetre and l, which is the total length in centimetres through which the beam must pass. Together, these two terms incorporate the fact that more atoms will cause more scattering events. The result here is given in scattering events per incident electron.

A sample has two parameters which determine its scattering power - the atomic number of the atoms or molecules within the region which the beam interacts with and the density of the atoms or molecules in this region. Of the two, atomic number has by far the strongest effect - doubling the density of atoms will double the scattering, but doubling the atomic number will quadruple the level of scattering due to the Z^2 dependence in Eq. 3.1.

Because of this, homogeneously low atomic number samples such as biological material or polymers traditionally have specific parts of them stained with heavy elements (such as osmium, gold or uranium) beforehand [36, 4] to improve the contrast level inside the STEM.

However, due to the $\frac{1}{E^2}$ dependence of scattering power, the 25 keV beam of an SEM will scatter sixteen times more strongly than the 100 keV beam of a dedicated STEM from any given sample. Although this does not of its own accord give contrast between two regions of identical composition but differing density, it does serve to amplify any contrast which may be present - this is illustrated in Figure 3.1.

The other method of obtaining contrast is that of net beam attenuation. In situations either when the scattering is the same between different parts of the sample or when the whole transmitted signal is collected without discriminating between bright- and dark-field components, the only difference is in the amount of energy transmitted.

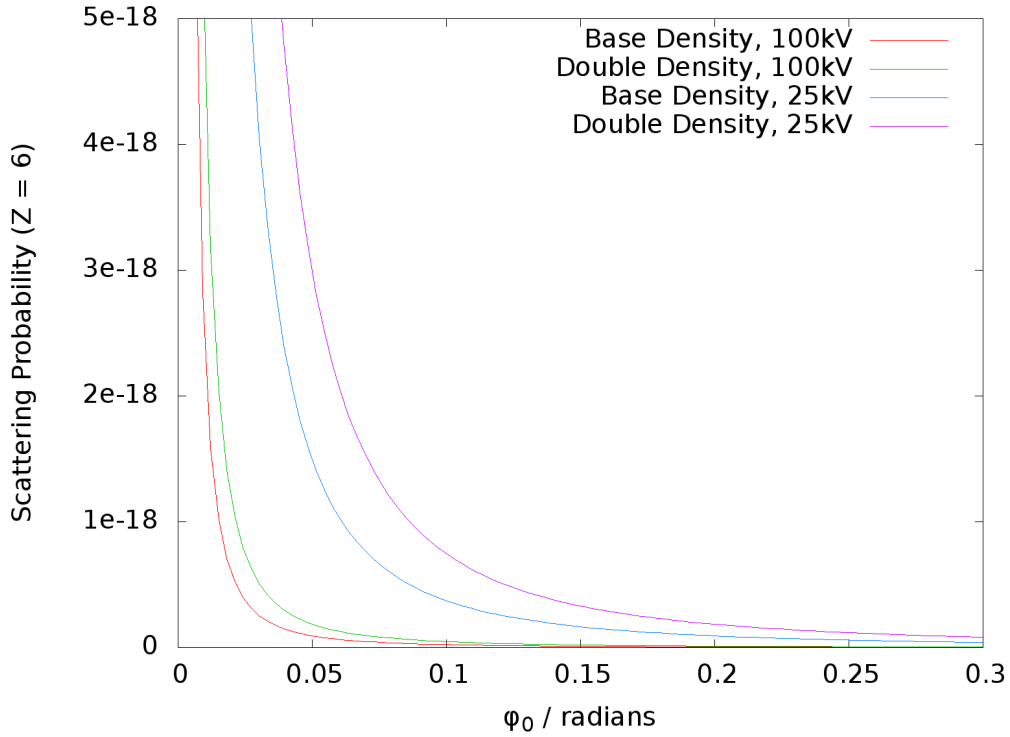

Figure 3.1: A plot of equation 3.1 showing the beam scattering power from two samples; both have an atomic number of 6, but one is twice the density of the other (and therefore has a multiplier of two compared to the base density). Acceleration voltages of 100 kV and 25 kV are compared. Note that the difference in scattering power between the 25 keV irradiated samples is greater than that between the 100 keV irradiated samples.

Kanaya and Okayama derived a semi-empirical formula for the range of an electron inside a sample (Eq. 3.2), along with the related formula linking electron energy to the distance travelled through a sample [37].

$$R = \frac{2.659 \times 10^{-10} A_f E_0^{5/3}}{\rho \sum_i \overline{Z_i^{8/9}} n_i} \tag{3.2}$$

Here, R is the electron range in metres, A_f is the formula weight for

one repeat unit of the material, E_0 is the energy of the incident electron in eV, ρ is the density of the material in kg m^{-3} and where Z_i and n_i are the atomic number and abundance of each element within one repeat unit of the material, respectively. For example: water has the formula H_2O, with a formula weight of $1 \times 2 + 16 \times 1 = 18$. Z_i and n_i would be 1 and 2 for hydrogen and 8 and 1 for oxygen, respectively.

$$E = (1 - \frac{x}{R})^{3/5} E_0 \tag{3.3}$$

Equation 3.3 gives the energy of the electron after penetrating a depth x into the sample, using the result of equation 3.2 for R. The value which decides the actual signal level is dependent on the type of detector (see part 3.2.2) - some measure the total energy absorbed from the beam, whereas others may derive their signal by counting the number of electrons with their energy playing relatively little part in the process.

3.2 STEM in the ESEM

Since the ESEM at its most basic level is an SEM with additional apertures, a STEM detector may also be used for low-vacuum work. Because the sample cannot sit directly on the STEM detector (some distance between the sample and detector is required to provide angular discrimination), there will be gas present between the sample and detector. This gas will scatter the transmitted beam and reduce the contrast (re-directing unscattered electrons into the dark-field segment and vice-versa), but since it takes 1cm of water vapour at 5 Torr/666 Pa and 1°C (typical gas conditions for imaging liquid water) to present the same number of molecules as 50 nm of liquid water, post-sample scattering will not present too much of a problem.

As mentioned before (part 2.1), the use of ESEM allows a broader range of samples to be imaged than conventional SEM - insulators, wet samples,

etc. By using a signal other than secondary electrons, the possibility of imaging components which are deeper than the escape depth of secondary electrons arises - for example, a sample completely immersed in water could theoretically be seen with STEM while remaining invisible to conventional ESEM.

Furthermore, the mechanisms by which contrast is generated with STEM (see part part 3.1.1) differ from those which generate secondary electrons (part 1.3.3), offering an alternate view of the sample to the microscopist.

The concept of using STEM in the ESEM (called Wet STEM by its originator) was envisaged relatively recently in 2005 by Bogner's group [38, 39], who created a sample holder which held a temperature-controlled sample over a backscattered electron detector and demonstrated its applicability to a broad range of samples. The work carried out for this thesis is intended to expand upon Bogner's method - developing an understanding of the contrast mechanisms, comparing it to other microscopy techniques and providing examples of how Wet STEM can be used to solve specific problems.

3.2.1 Wet STEM Assemblies

While Wet STEM detectors can now be bought as a packaged item, the original work [38, 39] was carried out before they existed and as such the first researchers had to assemble one from scratch. Three components are required for a Wet STEM detector: a Peltier stage for cooling, an electron detector of some sort and a mount to hold thin samples above the detector and in thermal contact with the Peltier stage.

Figure 3.2 is an example of the type of detector that Bogner's group used for the first Wet STEM work [38]. Samples mounted on a standard 3.05mm TEM grid are placed in the recess on the holder arm, positioned over the BSE detector which is responsible for generating the imaging signal.

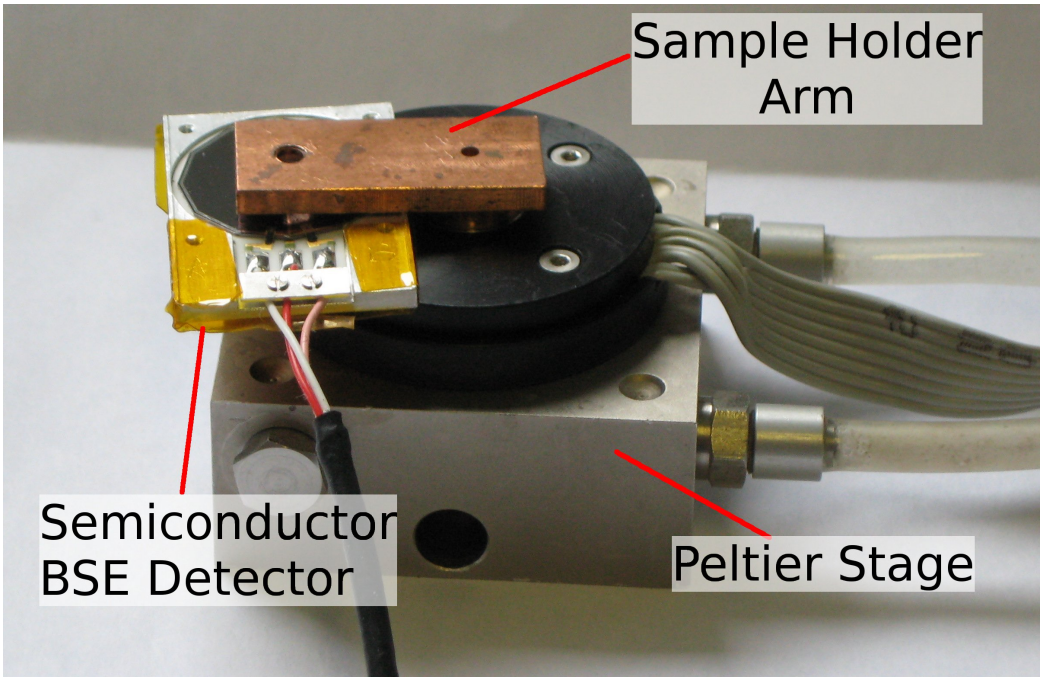

Figure 3.2: A picture of a Bogner-type Wet STEM detector [38], with the relevant three components indicated.

The device in figure 3.3 is similar in operation to that in Figure 3.2, but is packaged and sold by FEI Company for their ESEM instruments. It functions in exactly the same way as Bogner's initial detector, but the sample (still on a standard 3.05mm TEM grid) is now held inside a two-part capsule rather than sitting exposed on the top of the holder arm - this holds the sample in place more securely and allows better thermal contact with the Peltier stage.

Because the construction of both detectors is so similar, there is no difference in STEM performance between them. While the FEI detector is more convenient to use and offers better temperature control due to the tighter contact between the Peltier stage and the sample, the geometry of the sample capsule hampers collection of secondary electrons when compared to an exposed sample in a Bogner-style detector. In this work, unless otherwise stated, the FEI detector was used for recording all Wet STEM images.

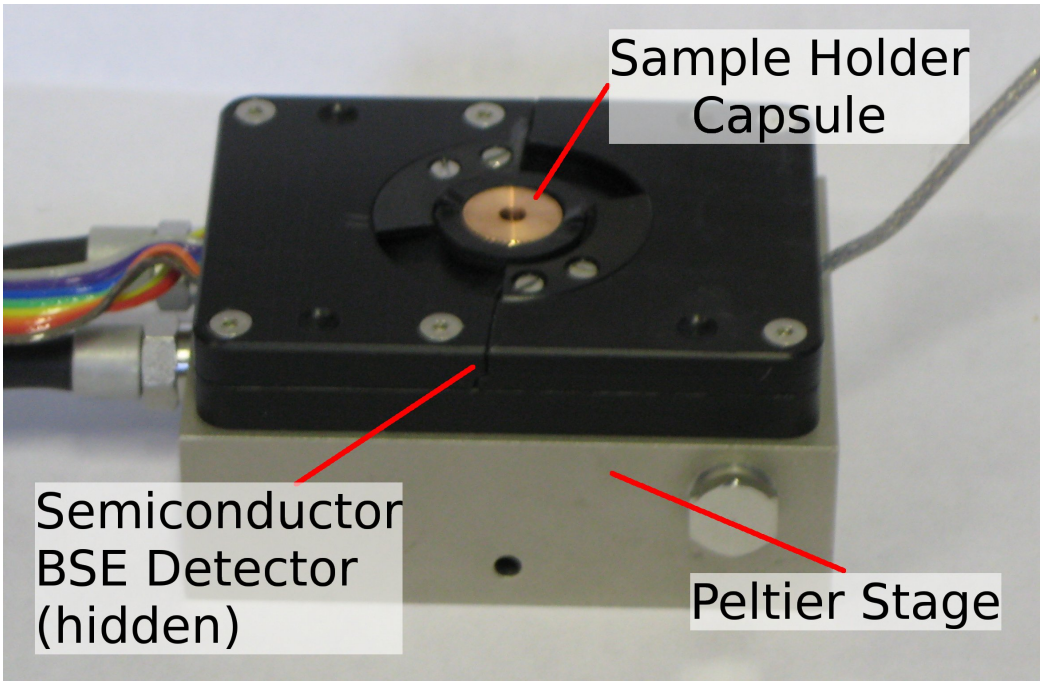

Figure 3.3: A picture of a packaged Wet STEM detector accessory from FEI. The inner workings are the same as the Bogner-type detector 3.2 and again, the relevant three components are indicated.

3.2.2 Signal Detection

There are several ways in which transmitted electrons could theoretically be collected. The first method, described in 1970 [40], is a paired system of a target with a high secondary electron yield beneath the sample and an additional secondary electron detector to collect the emissions from the target. Secondly, a scintillator and photomultiplier system as used in dedicated STEMs and in the first STEM in SEM work [32] could be used. Finally, a semiconductor detector can be positioned beneath the sample.

To date, only semiconductor detectors have been used. Converter plates do not easily allow simultaneous collection of bright- and dark-field signals and also suffer from any limitations that environmental SE detectors

have. Scintillator-photomultiplier systems could theoretically be used, but are bulky and require high voltages for the photomultiplier.

The initial work [38] used a backscattered electron detector to simultaneously collect bright- and dark-field signals. The chief advantage of semiconductor detectors are that they are physically small, use low voltages (of the order of 3-5 V) and that connections and an amplifier for the BSE detector are standard in all ESEMs.

A semiconductor BSE detector is a multi-segment p-n junction photodiode, with each segment having an independent readout. When electrons or photons strike the detector (providing that their energy is greater than the device's band gap), they will generate electron-hole pairs which are separated by the junction's inherent electric field. These electrons and holes are then collected and used to form the imaging signal. The output of the detector is proportional to the energy of the incident electron - higher energy electrons will generate more electron-hole pairs.

BSE detectors (such as those used inside the Bogner and FEI Wet STEM detectors) consist of two semi-annular segments. When installed inside a Wet STEM detector, the sample holder is typically positioned above the join between both segments and offset slightly towards one segment. The segment directly underneath the sample will then collect the unscattered beam (the bright-field signal) along with any components scattered away from the junction and the offset segment will collect any components of the beam which are scattered its way (the dark-field signal, see Figure 3.4).

Note that because of occlusion from the sample holder (see Fig. 3.2), each segment appears as a whole semicircle. The assembly therefore lacks an explicit bright-field segment, since the one directly below the imaging point collects both the unscattered beam and the components of the beam which are scattered away from the other segment. There are several ways to get around this complication.

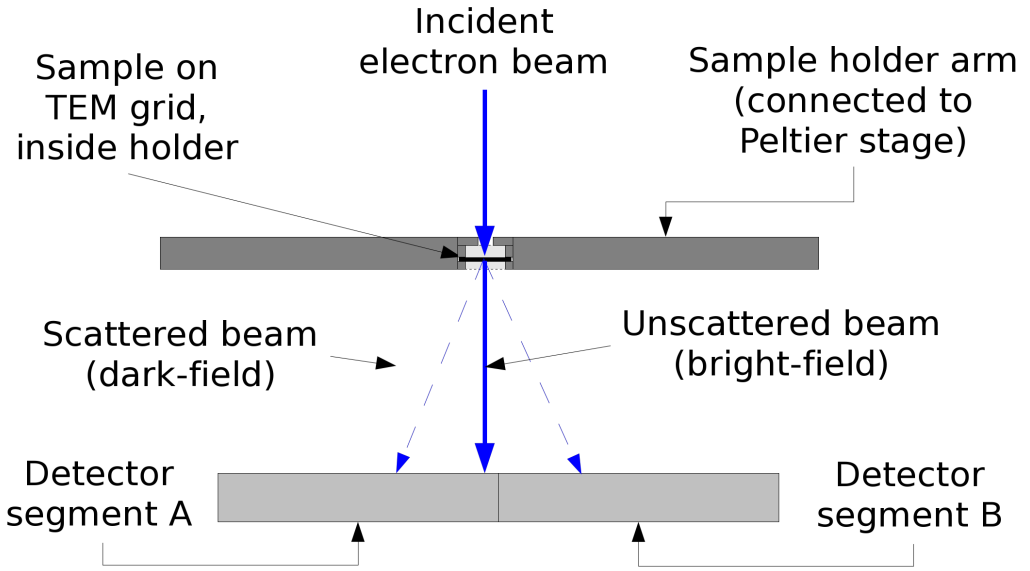

Figure 3.4: A schematic of how a two-segment semiconductor detector is positioned inside a Wet STEM assembly. Due to the slightly asymmetric positioning of the segments, Segment B only collects scattered electrons, while Segment A collects the unscattered beam along with the remaining proportion of the scattered beam. See also Figure 3.5 for a top-down view.

Firstly and most simply is to take signals only from the offset segment (segment B in figures 3.4 and 3.5). The resultant image will be formed only from the scattered beam and therefore will be a pure dark-field image.

Secondly is to take advantage of one of the design features of BSE detectors. Because they are installed directly below the polepiece for normal SEM use, they must have a hole in the middle to allow the electron beam through. If this central hole is located directly below the sample, the unscattered portion of the beam will be ignored and each segment of the detector will only collect scattered components. By taking the sum of both segments as the imaging signal, an annular dark-field image will be obtained. This is the method which Bogner's group employed [39] and is illustrated in Figure 3.6.

A similar result can be obtained by exploting a quirk of multi-segment

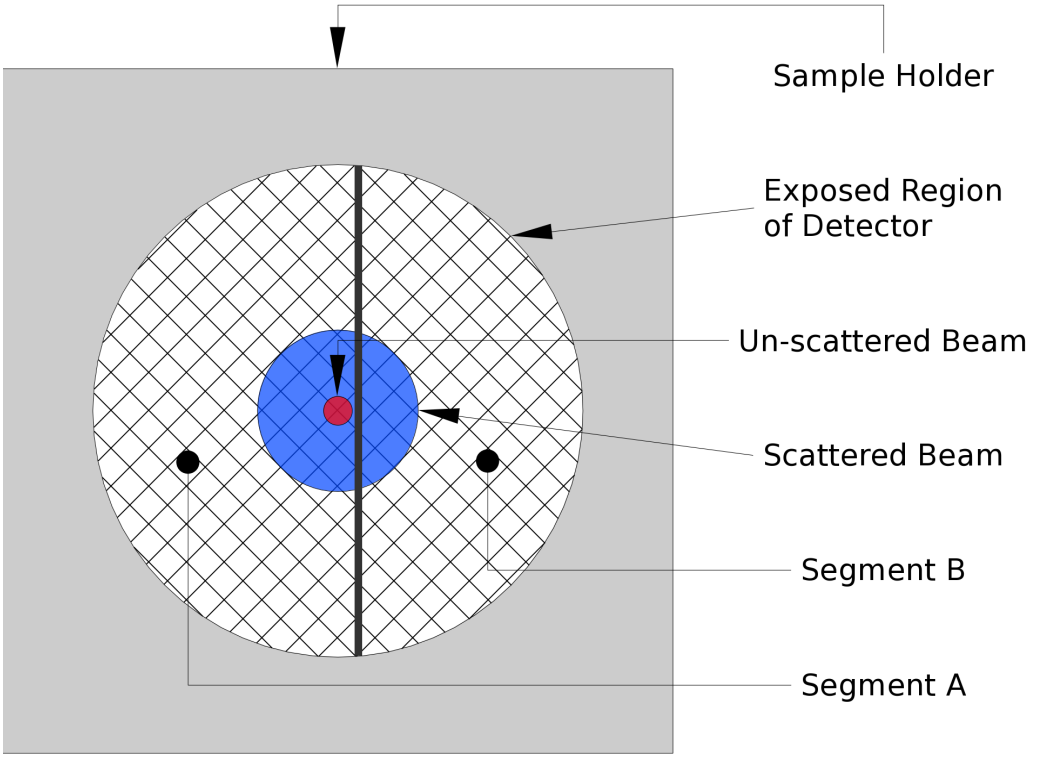

Figure 3.5: A sample-side view of the Wet STEM assembly's detector crystal. The electron beam's scattering with respect to the two segments is also shown. This is a top-down image of Figure 3.4.

photodiode design. Because the segments must be electrically isolated from each other to prevent signal leakage, there is a dead zone at the junction between them. If a point directly above this region is imaged, the unscattered beam will fall within the dead zone and will not be counted. Just as before, the sum of both segments will result in an annular dark-field image.

The final method is to take the signal from the segment which the unscattered beam impacts (segment A in Fig. 3.5) and subtract from it the other segment's (segment B in Fig. 3.5) signal. Assuming that the point being imaged is sufficiently close to the junction between segments and that the sample scatters isotropically (which is true for the multiple scattering events found at low beam energies, or for amorphous samples), the scattering into

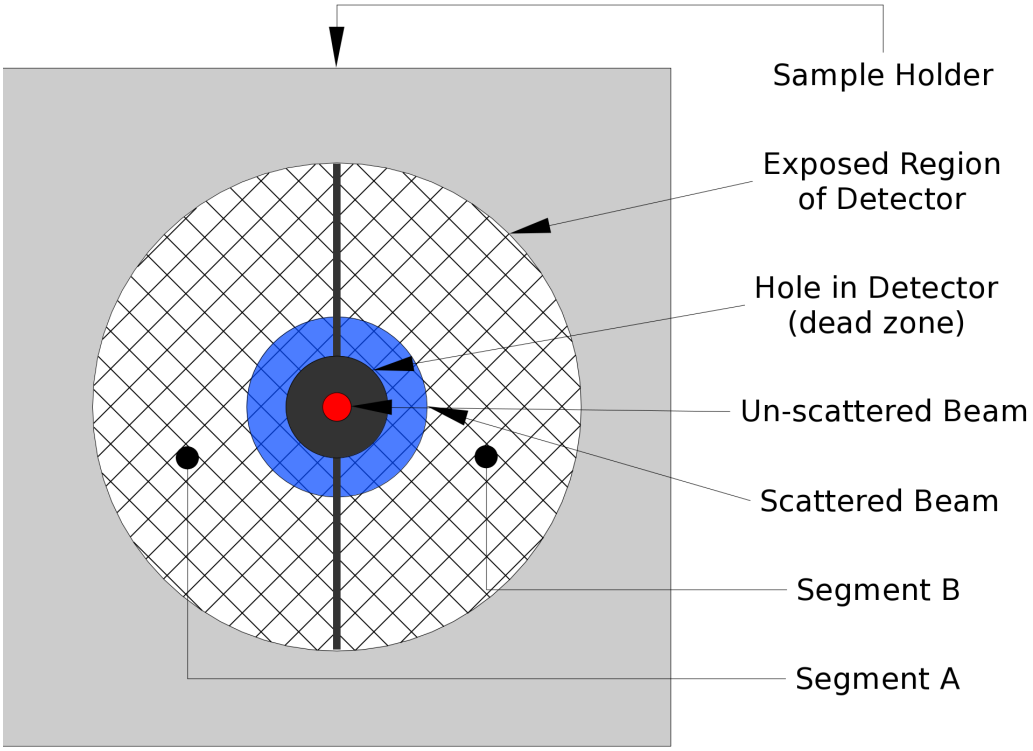

Figure 3.6: An illustration of the detector positioning used for the original work [38]. The unscattered beam does not impact any part of the detector, meaning that the sum of both segments provides a true annular dark-field signal. Compare to the geometry in Figure 3.5.

each segment will be roughly equal and as such the dark-field signal will cancel out, leaving a bright-field image.

Most of the imaging in this work has been conducted with the latter method. Although a pure dark-field signal theoretically offers a higher signal-to-noise ratio (there will be no background noise in an ideal system), I have found that it does not give enough signal to form a decent image without high-gain amplification and the resulting noise associated with such electronics.

An ideal assembly would use a detector with a central, circular bright-field region surrounded by an annular dark-field region. It would also permit

the detector to move about freely within the Wet STEM device, so that the bright-field segment is always coaxial with the electron beam. Such a setup would permit true bright-field and dark-field signals to be taken simultaneously.

3.3 Wet STEM Compared to Other Microscopy Techniques

While Wet STEM could be seen as ESEM with a twist, the different contrast mechanism involved means that its resolution can effectively be higher for the same type of materials than conventional SE-based ESEM. Because SEs are generated from any electron with sufficient energy which is within the SE escape depth (see Fig. 1.4), a not insignificant number will be created when backscattered electrons exit the sample (known as SE2-type secondary electrons) [2]. This means that SE signals will be generated from parts of the sample which are close to but not under the beam (see the red trajectories in Fig. 4.2).

By comparison, STEM images are less susceptible to this distance effect. If an electron scatters, it is counted as dark-field and if it does not scatter, it is counted as bright-field. Because of this, the resolution achievable using Wet STEM is potentially higher than that of conventional ESEM. Bogner's group have observed feature separations on the order of 5 nm in colloidal gold immersed in water [38].

The contrast mechanism from Wet STEM is the same as conventional (S)TEM and comes from scattering and as such is a function of atomic number and density. Because of the low accelerating voltage used when compared to a (S)TEM, density differences in the sample can play a more important role in forming an image (see Fig. 3.1), reducing the dependence on high atomic

number stains which conventional TEM employs for atomically-homogeneous samples.

The preparation techniques, or rather the lack thereof, are the biggest advantage of ESEM and by extension, Wet STEM. Because the ESEM is tolerant of insulating and wet samples, the traditional dehydration, fixation and coating steps are not required in the case of most samples. The only constraint is that STEM requires samples to be electron-transparent - for reference, a 25 keV primary electron will be absorbed after passing through 12 μm of water [37].

Chapter 4

Other Techniques

4.1 Monte Carlo Simulations

Because many of the equations which describe physical phenomena are either mathematically insoluble (for instance, multiple-body gravitational interactions) or incredibly complicated once more than a few elements interact (consider Rutherford scattering, equation 3.1, for multilayered systems), analytical solutions to them cannot be found. To make predictions from systems like these, a numerical method must be found and applied instead.

There are numerous interactions which take place when a beam of electrons impacts a sample. There is both elastic scattering, such as that defined by Rutherford and inelastic scattering in the form of secondary electron production, x-ray production and plasmon excitation, amongst other things. Whilst all these equations do have exact solutions, the complexity of the system and consequently the processing time and difficulty in formulating an analytical expression increases rapidly with the number of events. Electron-sample interactions are therefore insoluble in practice and must be analysed with numerical methods such as Monte Carlo simulations.

Monte Carlo methods work by simulating a large number of individual events (in this case, incident electrons) in sequence and averaging across every individual simulation. While each individual event may not resemble the overall system, their average will be a closer description (provided that the physical models used are correct). A Monte Carlo simulation must take into account all the significant processes which can affect the system in question. For instance, when a beam of electrons encounters a sample, it will be deviated from its original path and will lose energy via several mechanisms (for instance: secondary electron generation, x-ray production, phonon or plasmon production); all of which must be incorporated into the simulation in one form or another.

While each particular implementation will make different approximations and use different equations, the same basic principles and core algorithms will apply. In one example [41], only elastic scattering is used to evaluate path deviations, with a screened Rutherford elastic cross section used to determine how likely such a collision is to occur and through which angle the electron is deviated. The cross section, when combined with the material density, gives a mean free path and equation 4.1 gives the probability of travelling a distance s in a material with mean free path λ. Figure 4.1 shows a framework for a Monte Carlo simulation procedure.

$$p(s) = e^{-s/\lambda} \tag{4.1}$$

In the example described by Joy [41], a modified form [42] of Bethe's continuous slowing down approximation [43] was used to describe the rate of energy loss of electrons, which is responsible for generating secondary electrons, X-rays and cathodoluminescence. Calculating the rates of production for these signals is sufficiently complicated and detailed that entire papers [44, 45, 46] and books [47, 48, 49] are dedicated to them - they will therefore not be elaborated on further.

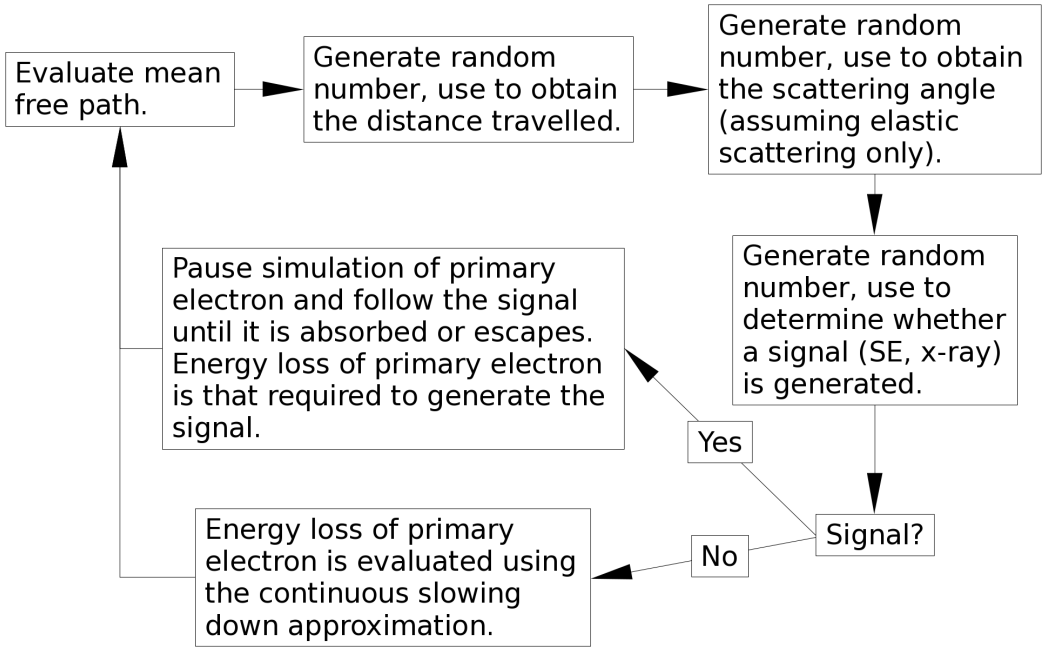

Figure 4.1: A flowchart showing the basic procedure involved in a Monte Carlo simulation of electron beam-sample interactions. The simulation is ended when either the electron exits the sample or its energy falls below a defined threshold, usually 50 eV. The book by Joy [41] was used as a reference.

A more detailed account of Monte Carlo methods can be found in one of many textbooks, such as that by Kalos and Whitlock [50] or Joy [41], which deals explicitly with electron microscope simulation and provided much of the reference material for this section. The software used in this work was CASINO v2.42, whose original publication [51] also contains some detail on the algorithms used and choices made in conducting Monte Carlo simulations of electron-sample interactions.

The output of a Monte Carlo simulation will therefore include not just the trajectories of the beam electrons (including those which become backscattered), but the yield and location of every simulated signal (secondary electrons, X-rays, etc.). Provided that the physical models and sample descriptions are accurate, Monte Carlo simulations serve as a useful method for

explaining phenomena observed inside the electron microscope and predicting the result of an imaging session on samples with a known composition.

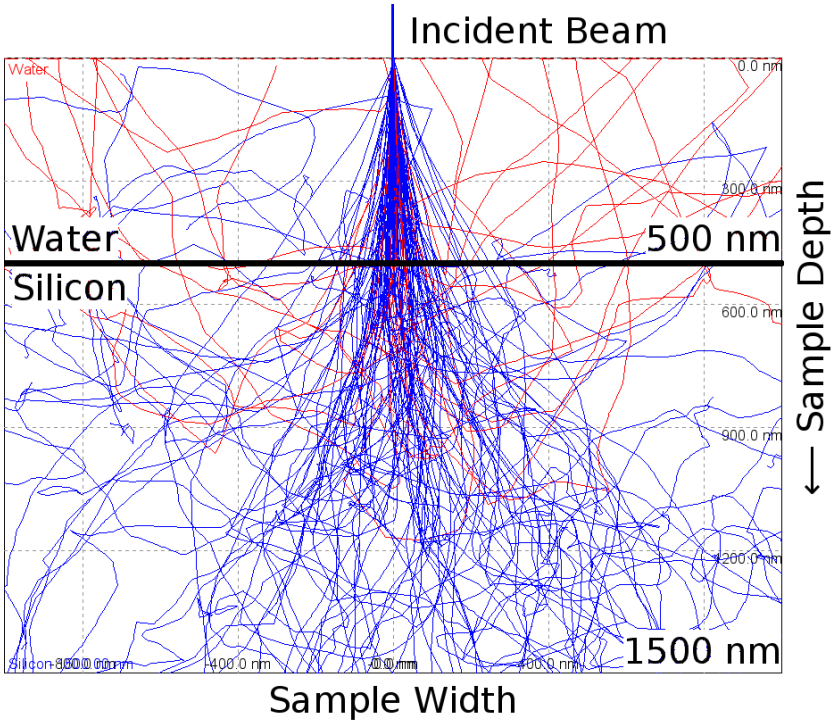

Figure 4.2: A Monte Carlo simulation of a 5 nm wide beam of 15 keV electrons impacting a sample which consists of 500 nm of water on a 1 μm layer of silicon. Field of view is 2.0 μm in the horizontal direction and 1.5 μm in the vertical direction. Red trajectories represent beam electrons which have scattered sufficiently to leave the top surface of the sample (and consequently have become backscattered). The parameters input to the simulation were: beam energy (15 keV), thickness, chemical formula and density for each layer, number of electrons to simulate (100) and probe size (5 nm). All other options were left with default settings. This image shows 100 trajectories.

Figures 4.2 and 4.3 are examples of data supplied by CASINO. Both are from the same simulation (a 15 keV electron beam impacting a sample which consists of a layer of liquid water on top of a layer of silicon) and show different things - electron trajectories in figure 4.2 and the localised energy

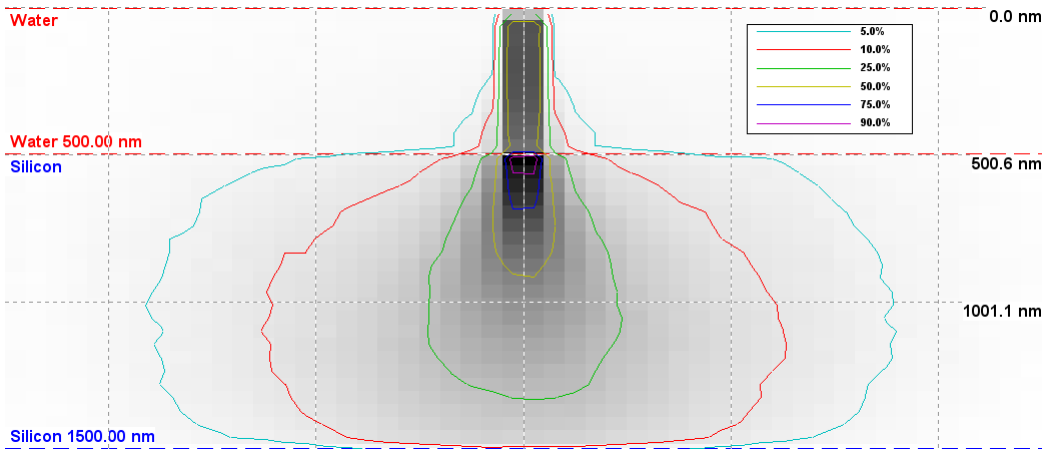

Figure 4.3: A plot showing the amount of beam energy deposited by region in the simulation used in Fig. 4.2 - iso-energetic contours are shown as coloured lines, with the most energy being deposited at the top of the silicon layer. This type of plot can be seen as another way of visualising beam spreading. The field of view is 3.5 μm in the horizontal direction and 1.5 μm in the vertical direction.

deposition in figure 4.3. Visualised trajectories such as this both inside and upon exiting a sample can be used to aid in interpreting STEM images.

It should be stressed that Monte Carlo simulations can only provide information about signals which they have been explicitly programmed to generate. CASINO v2.42 [51], for instance, contains code which generates x-rays for each element in the sample, records where they were emitted from and determines how many are absorbed by the sample. It also tracks any electrons that become backscattered and notes their maximum penetration depth. Finally, it records where in the sample energy is deposited. It does not contain code to generate secondary electrons, so it cannot reveal anything about the secondary electron yield of a sample. Neither does it record the trajectory of any transmitted electrons, so it cannot be used to obtain quantitative information about STEM contrast.

The accuracy of simulations such as this when compared to experiment

will also depend how closely the parameters input into the simulation match the physical situation. Each program will allow different microscope and sample parameters to be defined - in the case of CASINO v2.42, the sample can be defined as either a series of horizontal layers or a series of vertical layers, with each layer defined in terms of molecular formula and density. The microscope can be set up by defining a beam voltage, a sample tilt, a probe size, the position of the x-ray detector and optionally a scan pattern of multiple electron beams adjacent to one another.

Finally, due to their serial nature, Monte Carlo simulations may not take into account dynamic phenomena, such as contrast caused by differential sample charging [52] or the effects of beam damage.

4.2 Confocal Light Microscopy

Confocal scanning light microscopy is a way of improving the apparent resolution available to optical instruments. It functions by means of adding pinholes to the foci of lenses immediately before and after the specimen, which serve to reject light from any part of the sample which is not in the focal plane and directly illuminated, increasing the signal to noise ratio and hence the contrast available to the microscopist [53]. Note that the Abbe limit (see part 1.1) is not circumvented by this method - the ultimate resolution is still defined by the diffraction-limited spot width on the sample.

Figure 4.4 shows the core components of a confocal microscope. Note that only the illuminated spot in the sample can be seen using this setup - to image the sample as a whole, the focal spot needs to be scanned across the sample either by moving the sample itself (as with the first description of confocal microscopy [54]) or by scanning the pinholes and lenses to move the focal spot. Confocal microscopy implies a very shallow depth of field - because the pinhole rejects anything which isn't exactly at the focal spot,

there will be no information for regions which are out of the scanning plane.

4.2.1 Fluorescence Microscopy

Since light scattering or refractive index changes (such as in phase contrast microscopy) alone may not contain information about the region of interest, it is sometimes necessary (as in electron microscopy) to stain the sample to provide an additional form of contrast. Samples can be stained either negatively (eg. iodine causes starch to blacken) or positively, with fluorescent chemicals.

Fluorescence is the ability of a substance to absorb light at one wavelength and then re-emit it with a longer wavelength. By applying a selective fluorescent stain (for instance, DAPI, which is used to stain DNA [55]), irradiating the sample with light at the stain's excitation wavelength and filtering out all received light except for the stain's emission wavelength, an image will be obtained showing only the position of the stained material.

Provided that the excitation light spectrum does not contain any light in frequencies which are emitted by fluorophores used in staining, the background level should consist only of emitted light which becomes scattered by passage through the sample. Fluorescence microscopy therefore offers a higher signal-to-noise ratio than conventional light microscopy.

When imaging transparent samples (such as thin layers of biological material), light will be collected from the entirety of the sample and not just the focal plane, lowering the signal to noise ratio as a result. Because of this, fluorescence microscopy is best used in combination with confocal scanning microscopy. The two techniques combined offer a higher resolution image than fluorescence microscopy alone and a higher signal-to-noise level than either technique taken individually.

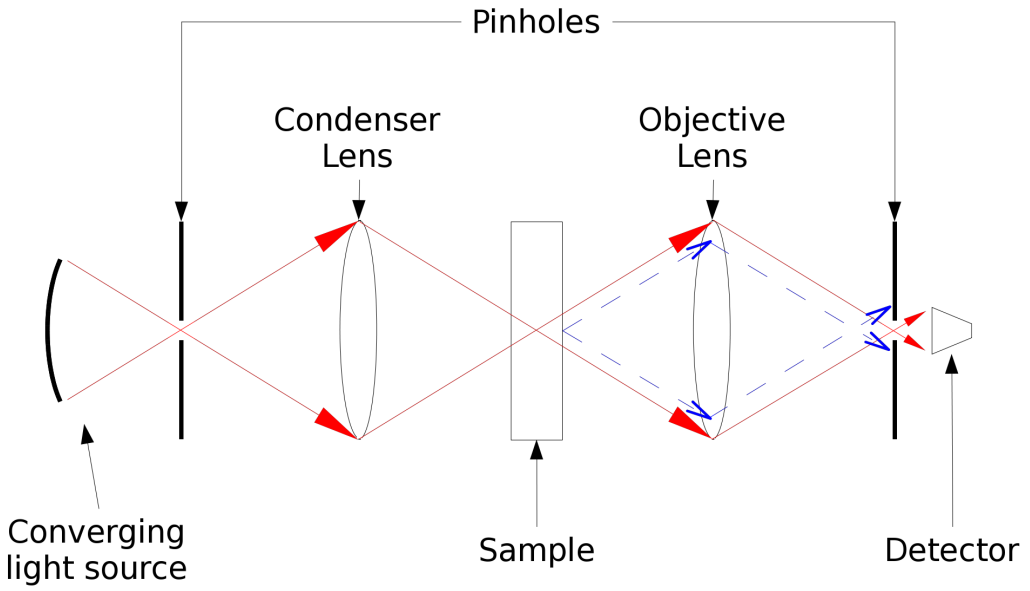

Figure 4.4: A schematic diagram showing the basic principles of confocal light microscopy. Light (red) is emitted from a converging source, which passes through a pinhole at its focus and is collected by the condenser lens whose foci are located at the first pinhole and inside the sample at the region of interest. Light transmitted through the sample from this point is collected by the objective lens, whose foci lie again within the sample (coincident with the focus of the objective lens) and within an exit pinhole, on the other side of which lies another detector. Light which is not emitted from this focal point (dashed blue lines) is not brought to a focus and hence is rejected by the exit pinhole. Diagram adapted from [53]

Chapter 5

Colloidal Suspensions

Because this work is based around investigating a technique rather than the behaviour of one specific system, a range of sample types will be imaged as a demonstration of Wet STEM's capabilities - image resolution, signal penetration and applicability to dynamic samples. The first test system will be that of colloidal suspensions, where colloids are defined as: "A microscopically heterogeneous system where one component has dimensions in between those of molecules and those of macroscopic particles like sand. A typical component of a colloid has one dimension in the range 1 nm to 1μm."[56].

Colloids come in various forms, depending on which phase state the various components are in - an example of a solid-in-gas colloid would be smoke and a liquid-in-liquid colloid would be an emulsion. Because of the ESEM's capacity to control liquid water, this work will demonstrate Wet STEM on two separate solid-in-liquid colloids, termed suspensions or dispersions.

The images in this chapter were taken using an FEI XL30 ESEM (FEI Company, Hillsboro, Oregon, US) equipped with a field-emission electron source.

5.1 Gibbsite Particles

The first test system is that of gibbsite, which is a type of clay. The mineral itself consists of hexagonal aluminium hydroxide plates which can be suspended in water under certain conditions [57]. Gibbsite suspensions have been imaged previously in the Cavendish laboratory using conventional ESEM [57], dehydrating a suspension inside the ESEM and showing how the plates pack together under conditions of different pH and salinity.

The gibbsite samples were grown in aluminium alkoxide solutions from seed crystals and made monodisperse by centrifugation [58]. Physically, they are the same as those used in the previous ESEM work on the subject [57] and are from the same batch of samples (originally prepared in the Van t'Hoff laboratory, Debye Institute, Utrecht University, The Netherlands). A stock suspension was created by adding 1 mg of dry plates to 1 ml of distilled water and sonicating the mixture for 15 minutes to ensure a complete dispersion (gibbsite was found not to be harmed by sonication [59]). For Wet STEM use, this suspension was diluted by a ratio of 1:40 with distilled water to ensure that the coverage was sufficiently light so that plates did not overlap. The gibbsite was observed to precipitate out of suspension over time, so each sample was shaken to re-disperse the particles before imaging. The sample used in this work has already been characterised [57] as having plates (574±63) nm across and (47±11) nm thick.

Since conventional ESEM obtains its images from secondary electrons which have a relatively low escape depth (see part 1.3.3), only those parts of the sample which are not submerged underwater can be seen - the sample in figure 5.1 was therefore dehydrated in-situ before imaging. Houghton's original work [57] was therefore an investigation into the post-aggregation state of gibbsite.

Aqueous gibbsite will therefore be a good test sample for investigating Wet STEM's capacity to image through other substances. In addition to

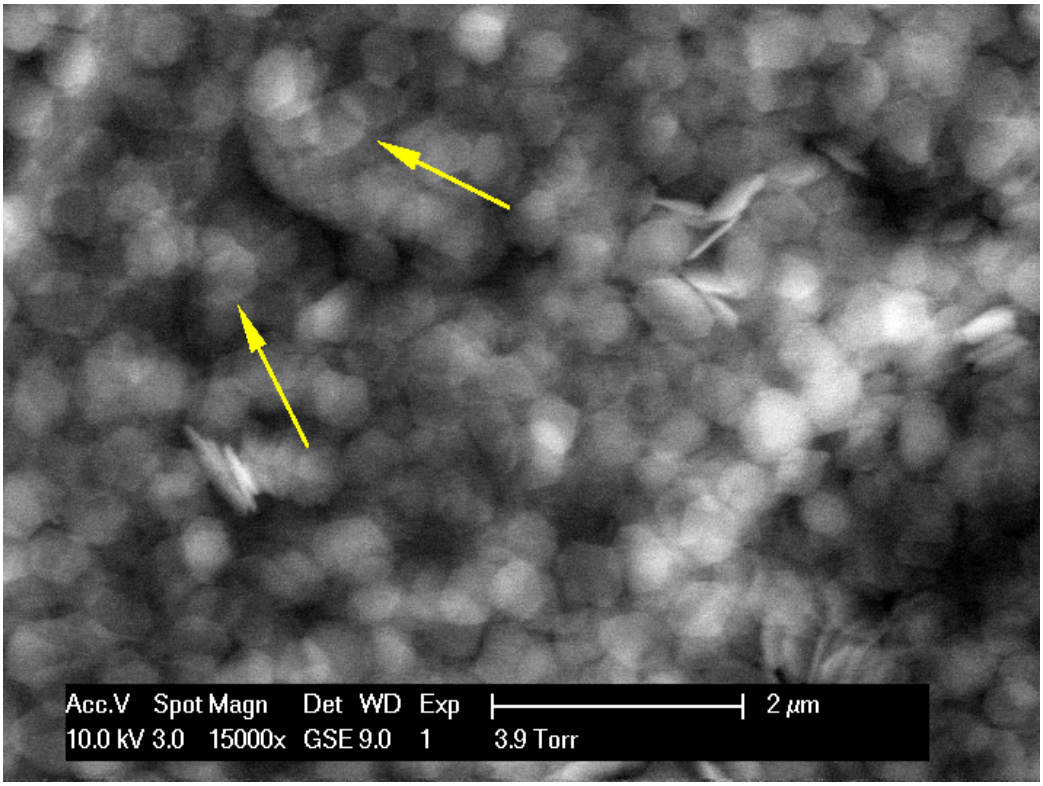

Figure 5.1: A SE image of in-situ dehydrated gibbsite. Note that some of the plates appear transparent (indicated by the arrows). Microscope conditions were 15℃ and 4 Torr.

sustaining a water layer on top of the gibbsite particles using the ESEM's capabilities, the plates themselves will stack together (see Fig. 5.1) and the amount of material through which the beam passes can be quantified if the plates have a well defined thickness.

Gibbsite's material properties also make it an ideal test sample. It does not change chemically or physically upon exposure to water, it is stable under the electron beam and its average atomic number is greater than that of the surrounding medium (water), giving it an inherent source of contrast (see part 3.1.1). Finally, to emphasise the advantages of ESEM, it is also an insulator - this means that even post-aggregation work could not easily be

carried out in a conventional SEM without further sample preparation.

5.1.1 Gibbsite Underwater

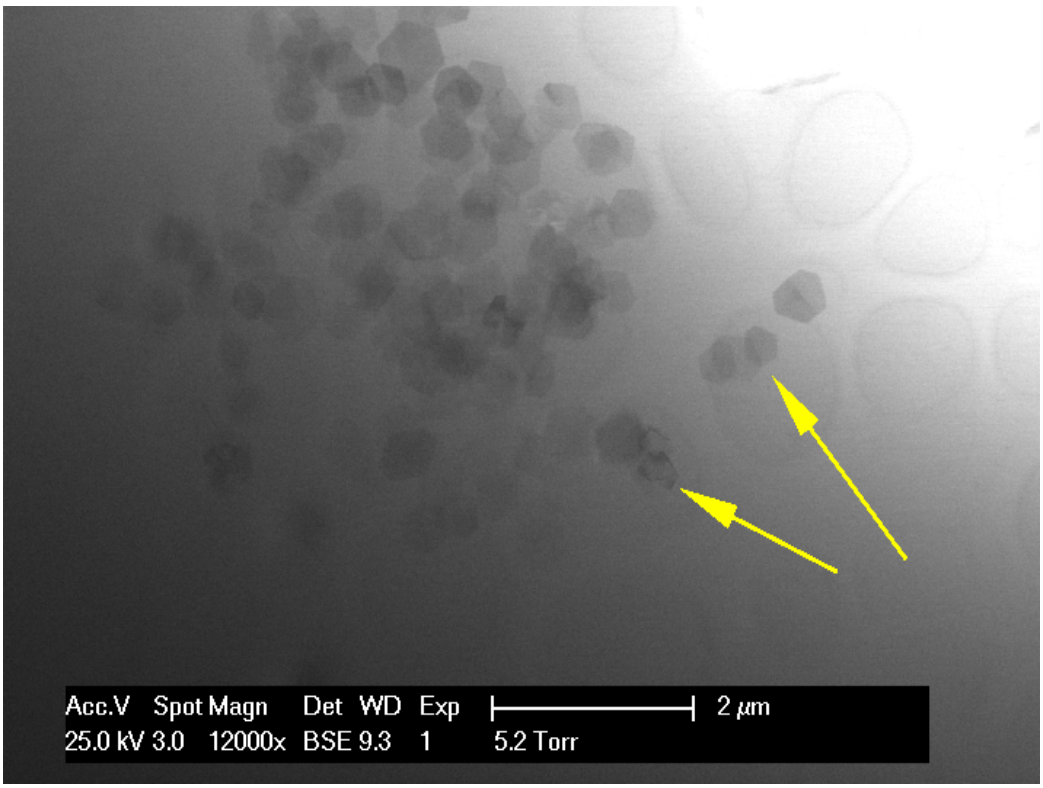

Figure 5.2: A bright-field Wet STEM image of gibbsite plates dispersed in glycerol solution. The web pattern is a holey carbon support film. Arrows indicate gibbsite plates suspended above holes in the film. Microscope conditions were 1°C and 5.2 Torr.

The sample in Figure 5.2 was prepared by diluting the stock gibbsite suspension by a ratio of 1:15 with 1% glycerol solution. The glycerol was initially added in an attempt to stop the plates from aggregating together and thus giving single layers on the support film, but had the additional property of sustaining liquid droplets with suspended particles inside the ESEM. This greatly simplified the process of observing gibbsite in suspension

- since glycerol is hygroscopic, droplets will evaporate less easily and as such will be more resilient under the electron beam than pure water. Note that the concentration of glycerol was originally 1%, but that spreading of the sample droplet across the film, condensation of water during purge and evaporation of water to permit beam transmission mean that the actual concentration at the time of imaging will be higher.

In bright-field Wet STEM, lighter regions correspond to less material. Because of this, the gradient going from upper-right to lower-left means that there is a continuous layer of material (water) covering the grid and that the thickness of this water layer is not constant. Plates of gibbsite can be seen positioned directly above holes in the film, showing that the clay is indeed suspended in liquid and not sitting on a surface covered by a droplet.

The visibility of gibbsite plates when underwater depends on how thick the water layers above and below them are - when the water is thin (shallower coverage is indicated by more beam propagation and the resultant higher background signal level - found towards the upper-right region of Fig. 5.2), the edges of the plates appear relatively well-defined. Conversely, when the depth of water coverage increases, the edges of the plates not only become blurred but the difference in grey level (signal level) between plate and water decreases. Because the absolute thickness of the water layer is not known, it is not possible to provide data on how much material the electron beam has penetrated before encountering the gibbsite plates.

It is also possible to image the Brownian motion of plates, provided that they are freely suspended in liquid. Figure 5.3 demonstrates this using gibbsite suspended in a 1% weight/volume solution of glycerol in water (again, microscope conditions will alter the concentration). Two progressions can be seen - firstly, the vertically-standing plate circled with a yellow ring navigates its way deeper into the droplet, becoming invisible due to occlusion from the water. Secondly, the plate in the upper-left corner of the image (not highlighted) moves upwards out of the frame of view. Other motion is present,

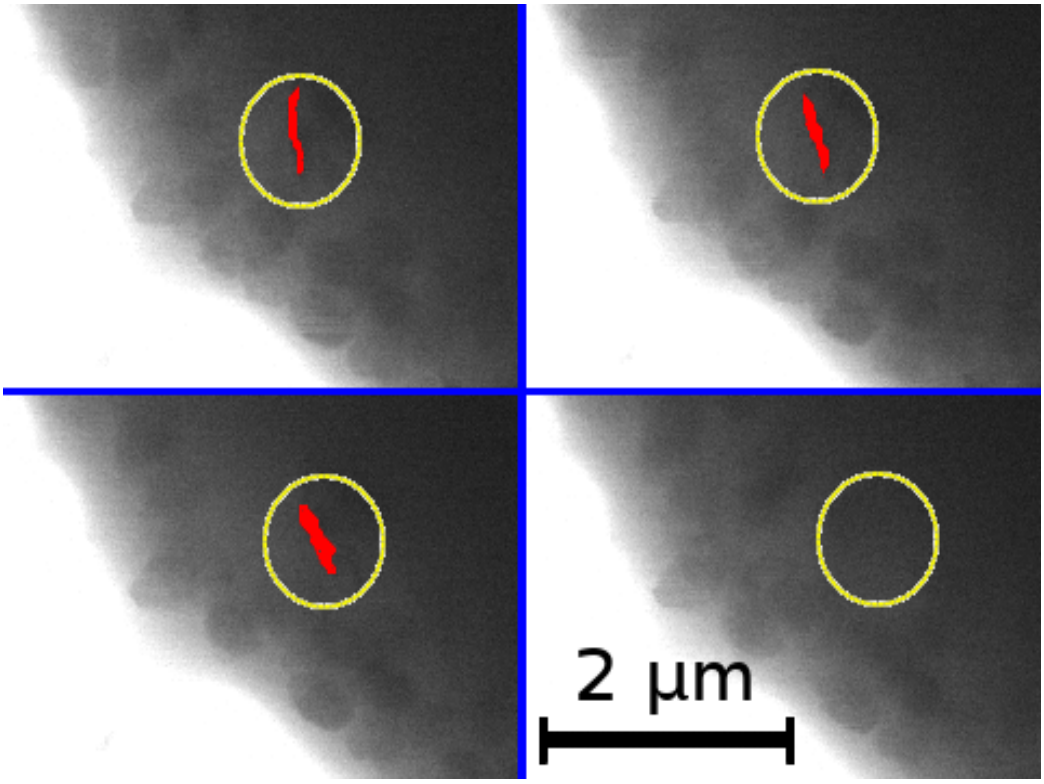

Figure 5.3: Four bright-field Wet STEM images of gibbsite plates suspended in a 1% weight/volume solution of glycerol in water. Images were taken sequentially, with a delay of 3 s between each. The yellow rings indicate the position of a plate (highlighted in red) which moved into thicker regions of the water and consequently disappeared as the images were taken. The microscope was operated at 25 kV and with a probe current of 120 pA. Environmental conditions were 1°C and 5.1 Torr.

but it only becomes apparent when the images are looked at sequentially or when carrying out live imaging with the ESEM.

5.1.2 Gibbsite Stacking

Because the depth profile of the water in figure 5.2 is poorly defined, no real information can be obtained as to how the image quality of an object is affected by the amount of material which covers it. A dry sample of this gibbsite, however, is comprised solely of 45 nm thick plates [57]. The degree to which lower plates are visible when a cluster of them overlaps should therefore offer quantitative insight into the penetrative power of Wet STEM imaging.

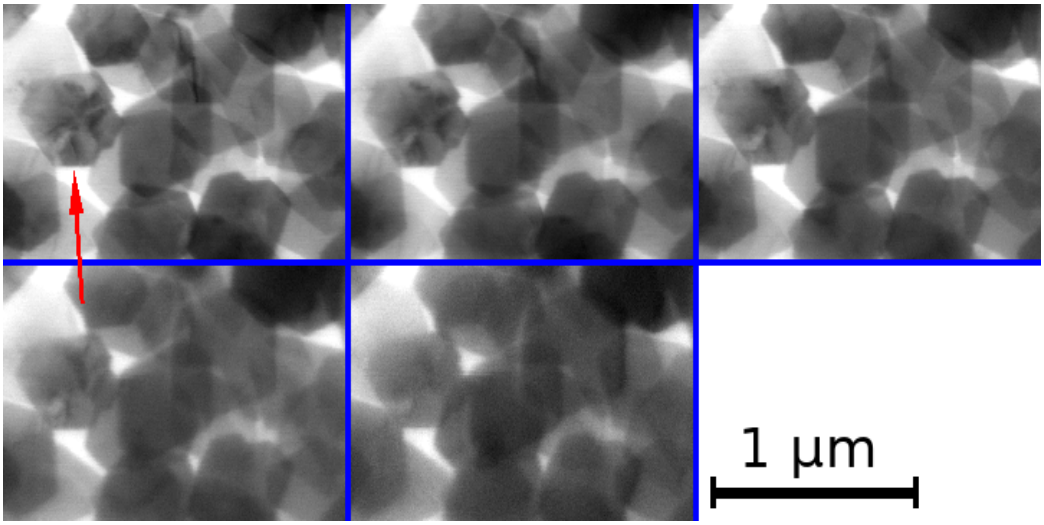

Figure 5.4: Five bright-field Wet STEM images of dry gibbsite plates, taken at different accelerating voltages. Top row: 30 kV, 25 kV, 20 kV. Bottom row: 15 kV, 10 kV. Microscope conditions were 20℃ and 1 Torr. The arrow indicates a plate with patterning sitting on another plate, the visibility of both the patterning and the other plate changing between beam energies.

Figure 5.4 shows the same area of overlapping dry gibbsite plates imaged at different beam energies. As the beam energy decreases, the difference in grey level between a stack of two and a stack of three plates also decreases. At 15 kV, it is no longer possible to clearly distinguish where the plates begin to overlap and looking at the 10 kV image only, it is not clear whether there

are multiple plates stacking in one area in the first place.

Secondly, the edges of the plates appear less distinct as the beam energy is reduced. At 30 kV, the outlines of the plates appear clear and sharp even when below three others - a situation which progressively declines as the beam energy decreases.

Finally, the patterning on the plate indicated by the arrow appears to fade as the beam energy decreases. This patterning is examined in more detail in part 5.1.3.

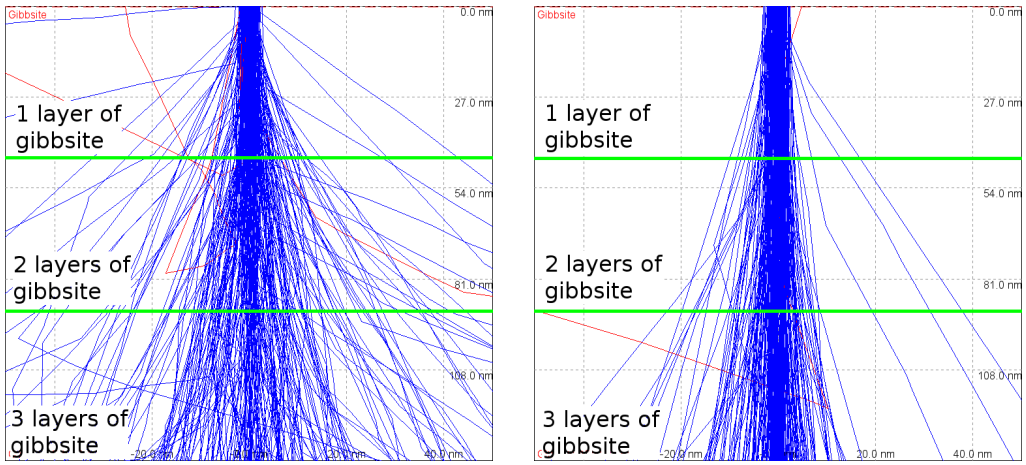

(a) 10kV **(b)** 30kV

Figure 5.5: Monte Carlo simulations of a 5 nm wide electron beam passing through a layer of gibbsite. The total thickness shown here is equivalent to three plates, with intervals of 45 nm marked off to indicate the depth of one, two or three plates. Simulations are carried out for (a), a 10 kV beam and (b), a 30 kV beam. The field of view is 100 nm across and 135 nm tall for each image. CASINO v2.42 software [51] was used for the simulation.

The difference in beam scattering between different thicknesses of gibbsite (and therefore the effective contrast) can be visualised using a Monte Carlo simulation, shown in figure 5.5 (see part 4.1 for an explanation). The simu-

lated sample in figure 5.5 was a 135 nm thick continuous layer of $Al(OH)_3$, with density 2.42 g cm^{-3}. 10 kV and 30 kV beams were used, with a 5 nm initial beam radius. 200 simulated electron trajectories are displayed.

While the 10 kV beam (Fig. 5.5a) still has a recognisable core and scattered component pattern after penetrating one plate's worth of gibbsite (45 nm), the angular distributions of electrons after penetrating 90 nm and 135 nm (2 and 3 plates) of gibbsite look very similar to one another. This translates to little visible difference between a stack of two plates and a stack of three when the transmitted beam impacts the STEM detector.

By comparison, the core (bright-field) and the scattered portion (dark-field) of the 30 kV beam (Fig. 5.5b) remain distinguishable from one another even after passing through all 3 plates (135 nm) of gibbsite. This means that there can be noticeable differences in the amount of scattering and therefore a contrast between stacks of two and three plates, an observation that has been made experimentally (Fig. 5.4).

As the beam spreads and consequently forms a large probe, it scatters from objects further away from its original trajectory. This causes blurring in the image and equates directly to a loss in resolution - the blurring can be represented mathematically as the convolution of the beam's point spread function with the "real" image one would obtain with a perfect microscope. A larger beam, whether caused by using larger apertures to allow more current or caused by scattering inside the sample will have a larger point spread function and as such a lower resolution. The decline in resolution with decreasing beam energy can be seen in figure 5.4.

This does not, however, explain why the edges of gibbsite plates appear consecutively more blurred as the beam energy is decreased. The probe size on the XL30 ESEM is approximately 5 nm at 30 kV and 15 nm at 10 kV, which is insufficient to cause the degree of blurring seen in Fig. 5.4 on 500 nm wide objects. Since the beam will not have penetrated any material

(aside from the imaging gas, which is incredibly sparse when compared to solid gibbsite) before impacting the sample's edge, it will not have been given the opportunity to spread out and should retain its original sharply-focussed profile.

Note that since the CASINO software does not provide information on the directions in which scattered electrons travel (and therefore what proportion of the transmitted beam will be detected by the bright-field segment), these simulations do not offer quantitative information on the expected STEM contrast. Any conclusions obtained are qualitative in nature. If another piece of software were to be used which did provide this information, and if the minimum difference in signal level required to exceed the noise level of the microscope and amplifier were known, then quantitative predictions about the transparency of any material in STEM could be made.

5.1.3 Other Properties of Gibbsite

Flakes of gibbsite, when imaged with STEM, are not the featureless plates which appear in conventional ESEM (see Fig. 5.1). Some of them (as indicated by the lower arrow in Fig. 5.2 and in Fig. 5.4) have some sort of apparent internal structure which looks similar to the bend contours found in conventional TEM [1, 60] of crystalline materials. This indicates that the gibbsite plates are not perfectly flat, but have been stressed by some mechanism and have bent as a result.

If this structure is caused by diffraction of the electron beam from crystalline materials, the portion of the scattered electron beam responsible for their signal should have a strong angle dependence. Figure 5.6 demonstrates the effect of changing the collection angle of the detector segments (see part 3.2.2) on the image produced. Even a small tilt is enough to significantly change the position and appearance of the intra-plate patterning, lending strong credence to the theory that these are bend contours [61]. When the

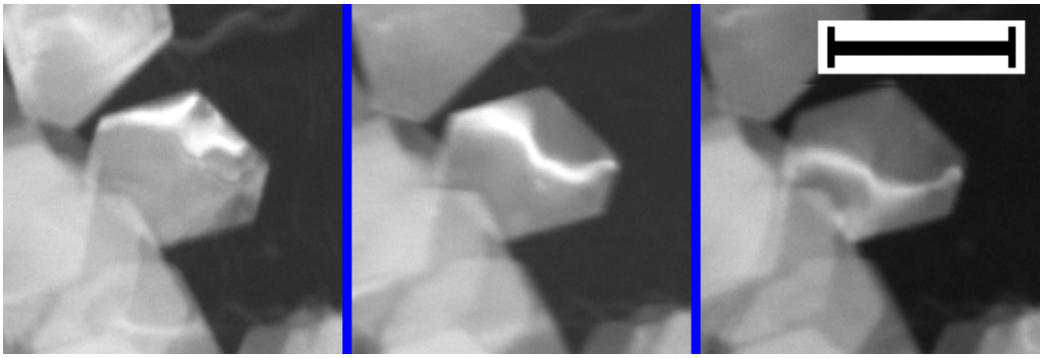

Figure 5.6: Dark-field images of dry gibbsite taken with a 25 kV beam, a probe current of 120 pA and 133 Pa/1 Torr of water vapour. The images are taken at tilt values of approximately -0.4°, 0°and 0.8°, where a positive tilt increases the minimum collection angle for dark-field signals. Scale bar is 500 nm.

sample stage is tilted enough (approximately 5°), the contours vanish entirely and the image is composed of pure mass-thickness contrast. Note that since the XL30 ESEM's stage is not equipped for high-resolution measurement and control of tilt angles, these results cannot provide quantitative information about the crystal structure of gibbsite.

5.2 Latex Particles

The other colloid sample that has been imaged is a water-based latex paint. This particular sample (provided by ICI) has been previously investigated using conventional ESEM to determine its mechanical properties [62, 63] as it dried in-situ. Just as with the gibbsite, it will be imaged both dry and wet using Wet STEM. This particular sample consists of 400 nm diameter spheres of a methyl methacrylate-2-ethylhexyl acrylate copolymer suspended in water. The original suspension contained a carbohydrate-based stabiliser, but it was diluted by a factor of 400 with distilled water in order to obtain

a single layer of paint for imaging.

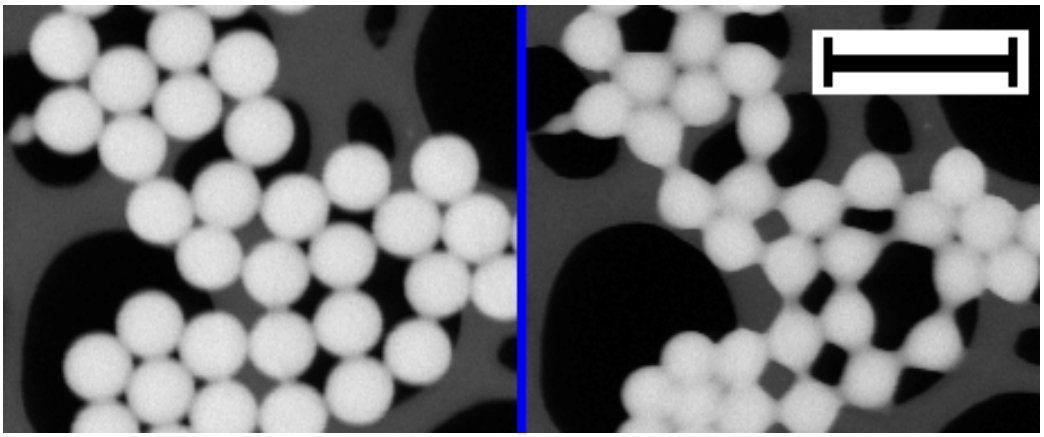

Figure 5.7: Dark-field images of dry paint on a holey carbon film taken with a 25 kV beam, 44 pA of probe current and 133 Pa/1 Torr of ambient water vapour at a temperature of approximately 20°C. The right image was taken after irradiating the sample with the electron beam for 6 minutes with a time-averaged beam intensity of 21.7 kW m^{-2}. Scale bar is 1 μm.

Figure 5.7 shows the effect that electron beam irradiation can have on a sample (see part 1.3.5). Before irradiation, the paint particles were mostly spherical and isolated (note that there is some bridging in the left-hand image - this occurred when navigating to the imaging site and when recording the image). After exposure to the electron beam, the particles appear to blend into one another, forming visible bridges between each other and distorting under gravity (note the difference between any particles which are suspended over a hole in the film before and after irradiation).

Since the material is a form of paint and as such is intended to flow over a surface, then mould together into a cohesive film, this inter-particle blending is to be expected. The coalescence behaviour of this particular sample has been previously investigated using ESEM and EDX [62]. Keddie described [64] the well-known process of film formation with four distinct stages - stage 1 is where they are freely dispersed with no interaction, stage

2 is when they touch and adhere to one another but maintain their general shape (see the left-most image in Fig. 5.7), stage 3 is where touching particles start to expand into a hexagonal shape to maximise the area of contact (see the right-most image in Fig. 5.7) and stage 4 is defined as when the particles have fully coalesced into an unbroken film of paint.

If a polymer does not crystallise (caused, for instance, by irregular molecular structure) and is taken below its glass transition temperature, it will retain the structure of the liquid phase, but its molecules will be immobile. Above the glass transition temperature, the polymer chains are able to move around, their mobility increasing with temperature. When mobile, polymer chains will diffuse past one another by Brownian motion - this means that paint particles above their glass transition temperature will merge if touching, a process which accelerates with increasing temperature. Further information on this subject may be found in works dedicated to polymer physics (such as that by Hamley [56]).

The glass transition temperature of this particular material has been measured as 280.1 K [62], which means that the operating temperature of the microscope alone (293 K) was enough to allow the polymer chains some mobility and thus permit the particles to merge. Particles irradiated by the electron beam were observed to merge with one another more quickly than non-irradiated regions. This could be due to a combination of two factors: firstly, that the electron beam was heating the sample up and speeding up the interdiffusion of the polymer chains and secondly, that the electron beam was causing chain scission in the irradiated part of the sample - shorter chains can diffuse more readily and as such will "melt" and move more easily.

To be noted is that the film changed little with additional beam exposure - an image recorded after 2 minutes of irradiation looked almost identical to the second image shown in Figure 5.7, even though it had only received one third of the energy.

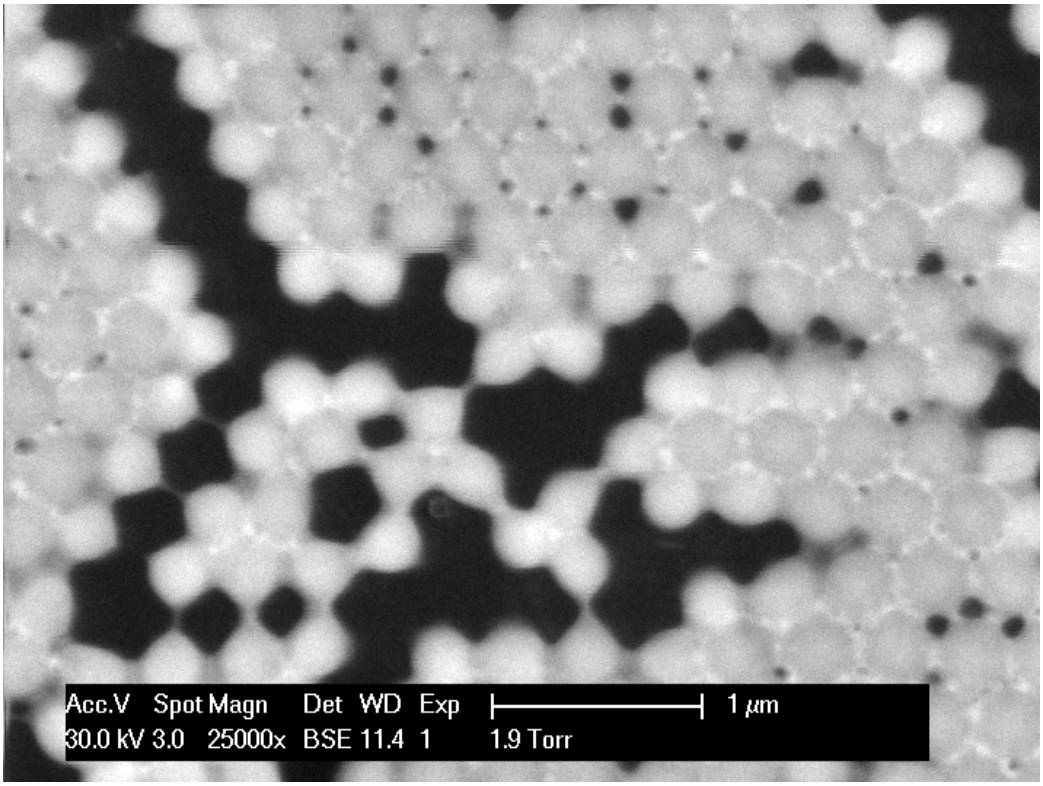

Figure 5.8: A dark-field image of a dry paint film taken with a 30 kV beam, 150 pA probe current, a sample temperature of 20°C and 2 Torr/266 Pa of ambient water vapour. Note the presence of electron-dense hexagonal patterns surrounding paint particles.

While imaging films of paint particles, hexagonal patterns of electron-dense material were sometimes encountered (Fig. 5.8). The most likely explanation is that they are caused by dissolved salts crystallising as the paint's water is evaporated, but the sample was moving too much and was too beam-sensitive for an EDX map to be obtained and as such their exact nature is unknown.

Figure 5.9 shows how paint particles appear when still in suspension. Note the lack of definition in the paint particles when compared to the gibbsite in Figures 5.2 and 5.3. This is because of the relatively low atomic number

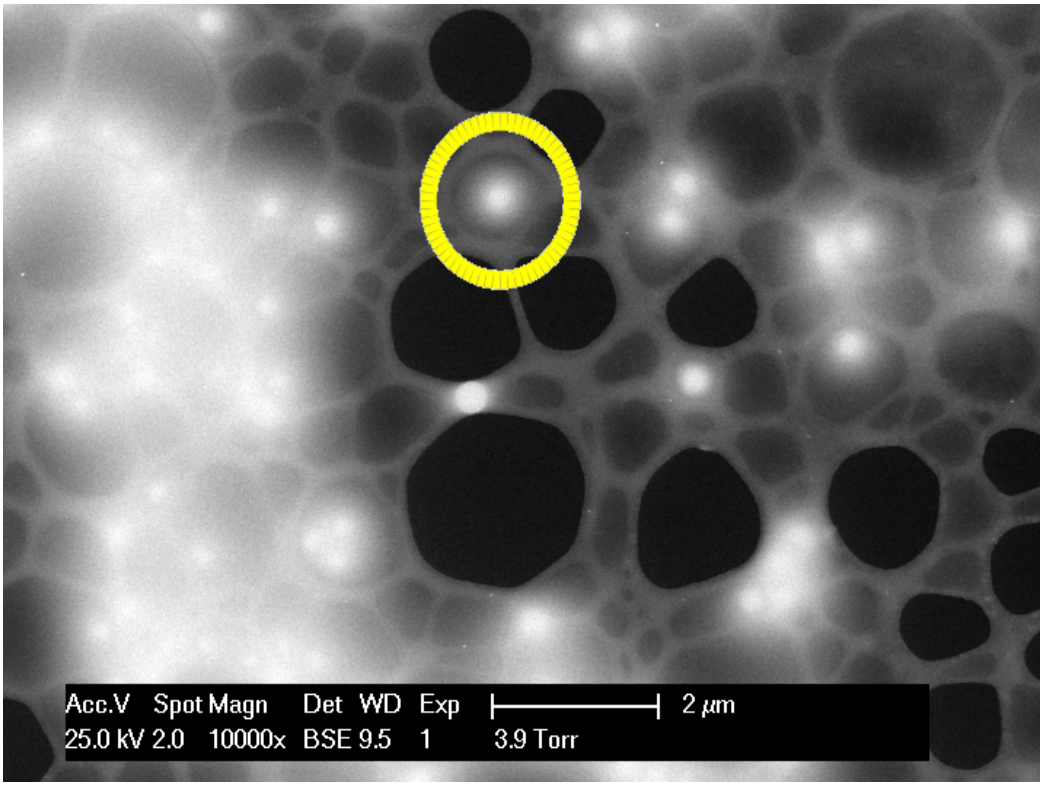

Figure 5.9: Dark-field images of dilute, wet paint on a holey carbon film taken with a 25 kV beam, 44 pA of probe current, a sample temperature of 1°C and 4 Torr/533 Pa of ambient water vapour.

difference between the particles (hydrocarbons) and the water. Even where the water level is relatively shallow (indicated by the yellow circle), the particles have an obvious "halo". A similar phenomenon has been seen before by Faucheu [65], where it was ascribed to the presence of a stabilising agent in the latex suspension. However, Faucheu also saw it on dry paint films, which was not the case here. A possible explanation is that the samples used in this work were too dilute for the stabilising agent to form obvious structures.

Additionally, although hard to distinguish due to blurring, there was no obvious bridging between the particles in suspension. This could be explained by several things: firstly and most importantly, the increased separation af-

forded by being suspended in water. Secondly, the condensed water and cooling stage could have served to conduct away sufficient heat (caused by the electron beam) to keep the particles below their glass transition temperature. Finally, any aggregation could have been hindered by the presence of any carbohydrate-based stabilising agent which still remained in solution. Provided that the water is a good solvent and that the carbohydrate chains are free-floating, the stabiliser molecules would swell in solution and provide a repulsive force between paint particles [56].

5.3 Colloidal Suspensions: conclusion

It can be concluded from this colloid imaging that Wet STEM is fully capable of imaging submerged materials (Fig. 5.2), but there is a loss of resolution when the scattering power of the sample is comparable to that of the liquid phase (Fig. 5.9). Wet samples offer the potential for dynamic, real-time studies (Fig. 5.3), though the time-resolution is limited by the scan rate of the microscope (1.5 seconds/frame in Fig. 5.3). Dry samples offer a higher level of detail (compare Fig. 5.7 to Fig. 5.9), potentially even being able to resolve multiple layers of the same object (Fig. 5.4), providing that the beam energy is high.

Chapter 6

Block Copolymers

The second class of materials to be examined using STEM are polymer films. A polymer is defined as "a compound with a molecular structure in which a (usually large) number of similar polyatomic units are bonded together" (Oxford English Dictionary), which encompasses a large range of materials encountered during everyday life - plastics, rubbers, protein, starch and DNA are all polymers, for instance.

The vast majority of plastics and rubbers encountered during everyday life are based upon carbon chains. Furthermore, their chemical structures are also very similar - polythene has the formula $[C_2H_4]_n$, polystyrene is described by $[C_8H_8]_n$ and poly(ethene terephthalate), or PET, has a formula of $[C_{10}H_8O_4]_n$.

The length of a polymer chain is determined when the polymer is synthesised, so there is no specific size of a polymer. Furthermore, due to the nature of chemical reactions, there will almost certainly be some variation in the polymer chain length - this is known as polydispersity. For reference, the molecular weight of polystyrene chains used for injection moulding is on the order of 200,000–300,000 Da [66], which corresponds to a chain of 2000–3000 monomers and therefore a total chain length of 600–900 nm (from Fig. 6.1a,

each monomer contributes 1 extra carbon-carbon bond in addition to the inter-monomer bonds, and assuming a C-C bond length of 0.152 nm [67]). Note that due to various factors (see part 6.2), the actual shape of the polymer molecule is not a straight line and as such will have an actual end-to-end distance which is somewhat smaller than the total chain length.

6.1 Polymer Imaging

6.1.1 Light Scattering

Despite the high molecular weight and relatively large size of polymer chains compared to other molecules, most polymer molecules are still too small to be directly imaged using light. Interference effects from bulk assemblies of polymers, however, are a viable technique. If a transparent, colourless polymer film is sitting on a reflective surface, has a different refractive index to that of the surface and the air and is of the right thickness, it will colour reflected light by means of constructive interference. When light of wavelength λ passes through a film with thickness $\frac{\lambda}{4}$, it will be strongly reflected due to interference between the reflections at the air-film interface and the reflections at the film-surface interface.

A more precise way of carrying out this type of analysis is known as ellipsometry. It functions by means of measuring changes in polarisation of reflected or transmitted light. By varying the angles of incidence and reflection, a table of information can be constructed about a thin film system - either one film or a series of layers. Given the refractive index of each material, the thickness of each layer can be evaluated at Ångstrom resolution - the converse can also be carried out. A more in-depth description of ellipsometry can be found in the book by Azzam and Bashara [68].

Finally, if polymeric objects align themselves in a regular array with di-

mensions comparable to the wavelength of light, they will exhibit Bragg scattering in exactly the same way as crystals do for X-rays or electrons. Any biological material which exhibits iridescence (for instance, butterfly wings) achieves it via this method, using a grid of proteins or other natural polymers [69].

6.1.2 Atomic Force Microscopy

While X-ray and neutron diffraction can provide information about the ordering and structure of polymers on a molecular level, beams of X-rays and neutrons are difficult to focus (the smallest beam size offered by the ESRF at the time of writing is 59 nm x 43 nm on their ID22NI beamline [70]). The information provided by such a beam will therefore be an average of everything contained within it and as such will not say anything about variations in structure below that length scale. To visualise local structure, alternative techniques are required.

One such technique is atomic force microscopy (AFM), which is where a sharp (30 nm or better [71]) tip attached to a cantilever is touched to the surface of a sample and scanned across it in much the same way as the electron beam in an SEM. The deflection of the cantilever is measured (usually by reflecting a LASER off the tip into a quadrant photodiode) and from that, a direct map of the surface profile can be obtained. An AFM can also be operated in tapping or phase-contrast mode, where the cantilever is oscillated at its resonant frequency and phase changes in the oscillation monitored as it is scanned across the sample. The phase change exhibited varies depending on the hardness of the material, so it is possible to obtain a compositional map when operating an AFM in phase-contrast mode.

Further information about AFM can be found in the book by Wiesendanger [71] and details on its application to polymers in particular can be found in the book by Sawyer, Grubb and Meyers [4].

6.1.3 Polymers in the Electron Microscope

The other main method of imaging the structure of a polymer directly is by using an electron microscope. As mentioned earlier (part 1.1), the wavelength of an accelerated electron is significantly smaller than that of visible light and as such it will be capable of resolving details on the atomic level. Both SEM and TEM can be used to image polymers - SEM for bulk systems and TEM for thin films.

Most polymers (with the exception of a few specific conducting or semiconducting polymers) are very good insulators, being composed of a non-conjugated carbon chain. Samples can charge up when imaged in both an SEM and a TEM, but the effects are more prominent in SEM due to thicker samples and lower beam energies causing increased levels of charge deposition. As mentioned before (part 1.4), insulators can be covered with a thin layer of metal to alleviate charge buildup. Alternatively, the accelerating voltage may be chosen such that the incoming (primary beam) and outgoing (secondary and backscattered electrons) charge flows cancel out, but the precise voltage needed will vary depending on the sample's composition and topography.

Each polymer reacts differently to the incident beam. Some, such as poly(methyl methacrylate), damage easily when irradiated. Others, such as polystyrene, are more tolerant of radiation due to the presence of large, resilient aromatic groups [4]. In a two-component polymer system, the electron beam may therefore cause artefacts by selectively ablating one of the polymers. Such a process can be used intentionally to enhance contrast between the resilient and fragile phases [72].

A thin polymer film for TEM can be made either by sectioning a block using a microtome or a focused ion beam (FIB) instrument; or by dissolving the polymer in solvent and spin-casting it on to a suitable substrate. Because most polymers are chemically very similar to one another (being comprised of

a carbon chain with carbon and occasional oxygen or nitrogen side groups), there is little difference in scattering power between different polymers (see equation 1.3). Polymers intended for TEM imaging are therefore typically stained beforehand with a heavy element such as osmium or ruthenium [4]. Staining can be chemically-selective in the case of multi-component systems or sample-wide in the case of negative staining.

Electron microscopy is a versatile method of imaging polymers, having been used to visualise individual aggregations [73], lamellar structures [74], electrospun fibres [75] and the extension of a hexagonal structure after stress testing [76].

6.1.4 Polymers and ESEM

Since the ESEM is able to either negate completely or selectively control [77] the charge buildup in insulating samples, it offers the option of imaging polymers without having to coat them or having to work at one accelerating voltage to balance charging. There are several examples of polymer imaging in the ESEM in the literature: the morphology of lignin-based composites [78], the bonding of bone to biodegradable polymer films [79] and cross-sectional images of photovoltaic polymer blends [80]. Since sample charging is either eliminated or greatly reduced in the ESEM, it becomes possible to take quantitative measurements of signal intensity [46] to distinguish different insulators from one another, something which is not possible in high-vacuum SEM.

With the addition of a temperature controlled stage, ESEM is also capable of imaging polymers which are naturally wet in a hydrated state (for instance, biopolymers secreted from marine organisms [81]) or even polymers which are freely floating on a liquid water surface [82].

Since STEM in the ESEM is quite recent, it has currently seen little

application to polymers: currently, only semiconducting polymer films [83] and polymer-grafted latex particles in suspension [84] have been imaged. As mentioned earlier in part 3.1.1, a 25 keV beam in an (E)SEM will scatter sixteen times more strongly from any material than a 100 keV beam in a (S)TEM, which means that any inherent differences in contrast (Fig. 3.1) will be exaggerated in the (E)SEM and may be visible unaided without recourse to staining.

6.2 Polymer Physics

The most important fact defining the behaviour of a polymer is the fact that it is a long chain. Because of this, polymers cannot move and diffuse as easily as single atoms or small molecules. Polymer chains do not normally exist as a straight line - while this is not physically prohibited as such, the chemical bonds making up the chain are usually fairly free to rotate and as such the probability of all of them pointing in the same direction is very low. It is therefore entropically more favourable for a polymer chain to adopt a random walk structure.

A system undergoing a random walk will always take a certain step length every time it moves, but will take that step in a randomly determined direction. For tetrahedral bonding (such as that found on the backbone of most carbon-based polymers), the inclination of each step is always 68° from its previous direction [85], but the azimuthal angle can be random and as such the path is free to change via bond rotation (though the permissible angles of rotation will depend on steric hindrance from any side groups which the polymer may possess). When enough steps have been taken, the polymer chain will have enough rotational freedom to be able to loop back upon itself - at this point, it can be useful to define a new effective "monomer" size where the new "monomers" are free to take a true random walk - this is known as the Kuhn length, or b.

$$\langle R^2 \rangle = nl^2 \tag{6.1}$$

Equation 6.1 [85] gives the mean square distance between chain ends in an ideal random walk, where R is the chain end separation, n is the number of monomers and l is the monomer size.

$$N = \frac{R_{max}^2}{C_\infty nl^2} \tag{6.2}$$

Equation 6.2 [85] relates N, the number of Kuhn monomers in a polymer chain to the Flory characteristic ratio C_∞ (which is particular to each polymer and is determined by the bond stiffness and steric hindrance from monomer units, amongst other things), the number of physical monomers in a chain n, the physical monomer size l and the contour length $R_{max} = nl\cos\frac{\theta}{2}$, where θ is the bond angle. When $N \gg 1$, the Kuhn monomer number and size can be used in equation 6.1 to obtain the mean end to end chain length.

$$R_F = bN^{3/5} \tag{6.3}$$

The end to end chain length of a real chain (Flory radius, or R_F) is given by equation 6.3. While the exponent is not exactly 3/5 in practice (more in-depth theories give it as $R_F = bN^\nu$ where $\nu \approx 0.588$ [85]), 3/5 is sufficiently close that meaningful information can be obtained from equation 6.3.

When polymers are melted, their chains will inter-penetrate to a degree due to entropy. This means that one polymer molecule cannot diffuse as a whole through the melt - it must first untangle itself from the other polymers. Polymer diffusion instead happens by a process known as reptation, where one end of the polymer makes its way through the melt by undergoing a snake-like motion following its "head". If a polymer is sufficiently regular

and its melt cooled slowly enough, it will order itself, crystallise and "solidify" into a regular lattice. Otherwise, polymers will pass through a glass transition upon cooling, below which polymers are immobile but still possess the disorder of their liquid state. Polymer molecules in the solid, glassy state will retain the same conformation as they would have exhibited in a melt.

6.2.1 Polymer Mixtures

Part 6.2 deals with the size of one polymer in a melt or when solidified. A mixture of polymers will have a tendency to segregate when given enough freedom (when above the glass transition temperature or when in solution). While most polymers are again chemically very similar to one another, there is still a difference between each monomer and consequently there is an energy penalty to be paid if polymer A is adjacent to polymer B when it could be adjacent to more of A instead (though there are may be exceptions, such as if polymer A has a net positive charge and polymer B is neutral or has a net negative charge).

For single molecules, the small energy penalty in this case is vastly outweighed by the entropic gain from mixing in all but the most different chemicals and so different small-molecule fluids of a similar composition will mix easily. For instance, toluene and hexane will mix readily, whereas the energy penalty from mixing toluene and water readily exceeds the entropic gain from mixing and as such they remain separate.

In polymers, however, the individual energy penalty is multiplied by the number of monomers in each molecule. Depending on the molecular weight of the polymer (and hence the number of monomers), polymers which are very similar such as polythene and polystyrene will nevertheless attempt to segregate into distinct regions of one or the other when given sufficient mobility and time.

If two chains of a different polymer are grafted to one another (known as a diblock copolymer), there will still be an effective repulsion between the two different chemistries but they will be unable to completely segregate into one bulk region containing only polymer A and another bulk region containing only polymer B. The final state of a diblock copolymer (if heated above its glass transition temperature and allowed enough time to reach equilibrium) will vary depending on the relative proportions of the two components, the total chain length and the degree of incompatibility between each component. There are several forms which it can take - lamellae, hexagonally-packed cylinders, regular arrays of spheres of component A in a matrix of component B, a gyroid structure or if the repulsive effect is not strong enough to cause segregation, a disordered mixture. A more detailed study of block copolymers can be found in the work by Matsen and Bates [86].

The information in this section was primarily taken from the books by Rubinstein and Colby [85] and Hamley [56], which should be consulted if a more in-depth description of polymer physics is desired.

6.3 Styrene-Isoprene Diblock Copolymers

The samples used in this chapter are two diblock copolymers of polystyrene (PS) and 3,4-polyisoprene (PI), one of which has equal volume fractions of PS and PI (symmetric) and as such should result in a lamellar structure [86], while the other is 75% PS (asymmetric) and as such should provide hexagonally-packed cylinders [86] when annealed. Both polymers were synthesised and provided by Dr. Patrick Fairclough, Department of Chemistry, University of Sheffield.

The symmetric block copolymer has a weight-average molecular weight (M_w) of 578,000 g mol^{-1}, a number-average molecular weight (M_n) of 426,000 g mol^{-1} and a polydispersity (defined as $\frac{M_w}{M_n}$ [85]) of 1.38. The asymmetric

block copolymer has M_w = 898,000 g mol^{-1}, M_n = 747,000 g mol^{-1} and a polydispersity of 1.21.

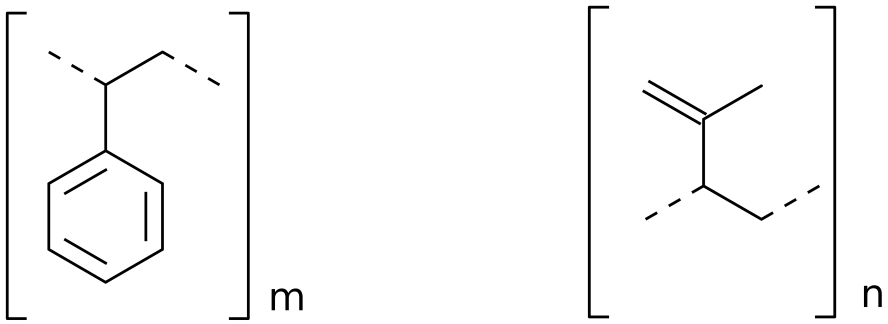

(a) Polystyrene **(b)** 3,4-Polyisoprene

Figure 6.1: Chemical structures of polystyrene (formula $[C_8H_8]_n$) and 3,4-polyisoprene (formula $[C_5H_8]_n$).

Figure 6.1 shows the chemical structure of the PS and PI monomers, both of which are pure hydrocarbons. At room temperature, amorphous PS has a density of 1050 kg m^{-3} and PI has a density of 910 kg m^{-3} [87]. Under these conditions, PS is a glassy solid, while PI is the chemical name for natural rubber which is flexible at room temperature. A difference between the two can therefore be seen in the phase [88] and topography modes (an AFM tip in tapping mode will compress the sample and create erroneous height maps [89]) of an AFM.

Because the composition of these two polymers is so similar, they are almost invariably stained before imaging under traditional electron microscopy [76]. TEM imaging under conditions of beam defocus (so that interference is the dominant contrast effect, rather than scattering [90]) allows these diblocks to be imaged unstained, but if the phases are not equal in size, their apparent size will change with the level of defocus which can lead to misleading artefacts. Staining itself, as with any process that modifies the sample, may

also lead to artefacts.

An alternative means of obtaining more contrast is to use a lower accelerating voltage, the principle of which has been previously covered in part 3.1.1. Unstained styrene-isoprene block copolymers have been successfully imaged at 5 kV in a low-voltage TEM [75], demonstrating that neither stains nor defocus phase contrast are necessary. Using an ESEM to carry out such imaging will allow the microscopist to reduce charging (see Fig. 6.3) and optionally, if the polymer in question will react with the imaging gas, to observe changes in the polymer structure as they happen. Neither component of PS-block-PI reacts with water or is particularly beam sensitive, so this will not be investigated here.

6.3.1 Sample Preparation

The PS-PI polymers were synthesised by Dr. Patrick Fairclough, Department of Chemistry, University of Sheffield using high-vacuum living anionic techniques [91, 92], with the following sample preparation procedure provided by him. Reactions were carried out in benzene (Sigma Aldrich, Gillingham, Dorset, UK) purified by degassing and stirring over living polystyryllithium for 24 hours, and initiated with known quantities of s-butyllithium in cyclohexane.

Monomers were purified as follows: Styrene (Aldrich) by degassing and stirring over di n-butylmagnesium for 24 hours, isoprene (Aldrich) by degassing and stirring over n-butyllithium for 24 hours. Each block was polymerised at room temperature with a 24 hour reaction time for the styrene block and 72 hours for the isoprene block, in between polymerisation stages, a small sample of living polystyrllithium was taken in a side arm equipped with a stopcock for future GPC analysis.

For both diblock copolymers used in this work, the isoprene addition

contained a small (slight stoichiometric excess) of tetrahydrofuran (THF) in order to change the polyisoprene microstructure from predominantly 1,4 to 3,4 enchainment (isoprene contains two double bonds, only one of which will be used for straight-chain polyisoprene. Fig. 6.1b shows the structure of 3,4-polyisoprene).

The final living polymer was terminated with an excess of degassed methanol added via an ampoule. The reaction mixture was then allowed to stand with periodic agitation for 2 days to ensure complete termination before the polymer was isolated by pouring into stirred methanol containing a small amount of antioxidant. At this stage the diblock and single block sample taken earlier were analysed by GPC and if necessary the polymer was fractionated using toluene/methanol as the solvent/non-solvent mixture at a concentration of $<$0.5% w/w in toluene, in order to remove any PS homopolymer.

Purified polymers were then dried under vacuum at room temperature to constant weight before further analysis by GPC and ^{1}H NMR was carried out.

For imaging under STEM, thin polymer films (estimated to be approximately 100 nm thick bases on the deep violet colour of reflected light, see part 6.1.1) were prepared by dissolving 0.1g/5ml PS-block-PI in toluene, applying a layer of solution to the surface of an ethanol-cleaned glass slide and spinning the glass slide in three consecutive steps for 2s at 2,000 RPM, 2s at 2,500 RPM and 20s at 3,000 RPM.

The coated glass slides were then solvent-annealed (a further description of the theory and process to do this can be found elsewhere [93]) by placing them inside a glass vacuum desiccator over degassed toluene, covering the slides loosely with a Petri dish to prevent splashing, evacuating the desiccator and allowing the vacuum to slowly leak over a period of 7h in the case of symmetric PS-block-PI or 48h, in the case of asymmetric PS-block-PI. Upon completion of the annealing process, the slides were removed slowly

by venting the remaining (very low) vacuum and sliding the desiccator open by 1cm; removing the lid of the desiccator; removing the petri dish covering the slides and finally removing the slides from the desiccator containing the toluene. Between each step of the removal and after removing the slides from the desiccator, the desiccator (or samples, in the final case) was placed in the airflow of an active fume cupboard for 1 minute.

Annealed films are removed from slides by scoring with a sharp scalpel and floating off on to deionised water, at which point 200-mesh TEM grids (Agar Scientific, Stansted, Essex, UK) were placed on the film and the film scooped up with a cover slip. Film thickness is determined by the colour of reflected light at this stage. Smaller sections of the film were cut and floated for the purposes of microtoming; these were collected with a 3mm diameter loop of 200 μm diameter wire.

For samples which were to be stained, staining was carried out immediately after retrieval from annealing. Films still on their glass slides were placed in another glass desiccator above a bottle of 2% aqueous osmium tetroxide (Agar) and the desiccator evacuated and left for 1 hour. After staining, slides were removed from the staining desiccator and placed in the airflow of an active fume cupboard for 5 minutes to remove any remnant OsO_4, then floated off with the same procedure as for unstained slides. OsO_4 attacks closely spaced pairs of unsaturated carbon-carbon bonds [4], cross-linking them and inserting a high-atomic number osmium atom which provides the staining properties. OsO_4 will therefore stain the polyisoprene phase only.

Samples to be microtomed for cross sections were placed in a sputter coater and coated with 100nm of gold on each side to ease location of the film in cross-sectional view. Coated films were embedded with Araldite CY212 resin (Agar) in a silicone mould, excess resin trimmed off with a scalpel and then 80 nm thick section ribbons were cut with a Leica Ultracut UCT microtome (Leica Microsystems, Wetzlar, Germany) and lifted off on to 300-

mesh copper TEM grids (Agar).

6.3.2 Polymers in Low-Voltage STEM

Because there is no benefit in keeping PS-block-PI films hydrated, imaging was conducted with the minimum pressure necessary to prevent charging (1 Torr/133 Pa) to minimise contrast losses to beam spread (see part 2.4.1) and no temperature control was applied to the Wet STEM detector. As with the colloidal samples (see part 5.1.2), an accelerating voltage of 25 kV was found to be optimal, though due to the comparatively lower atomic number of the sample, a larger range of beam energies was viable for this case than for the gibbsite.

Figure 6.2 shows the difference between an SE image (taken with a high-field needle detector [28]) and a dark-field STEM image of an annealed symmetric PS-block-PI film, both taken with 1 Torr of water vapour present for charge control. It is obvious that the STEM image exhibits much greater contrast than the SE image and with far less scan time. This translates at the absolute minimum to an eightfold reduction in the absorbed electron dose (faster electrons in STEM will deposit less energy in a thin sample than the lower-energy beam used for SE, so the improvement is potentially even greater) - useful for beam-sensitive samples.

The necessity of using ESEM for charge control can be seen in figure 6.3. While the image taken using ESEM (Fig. 6.3a) shows no distortions, the image taken under high-vacuum (Fig. 6.3b) shows both line discontinuities towards the top of the image in addition to a general buildup of charge over the whole frame, indicated by the large light and dark bands. Since both PS and PI are strong insulators, they cannot dissipate any charge implanted by the electron beam and require the ion flood from the ESEM's secondary electron detector (see part 2.5.1) to neutralise charge buildup. Nevertheless, contrast can still be seen in this low-voltage STEM image without the need

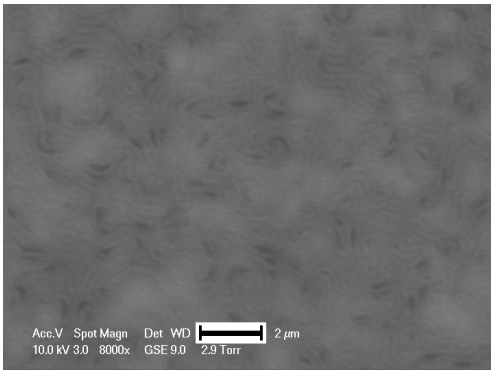

(a) SE image of PS-block-PI

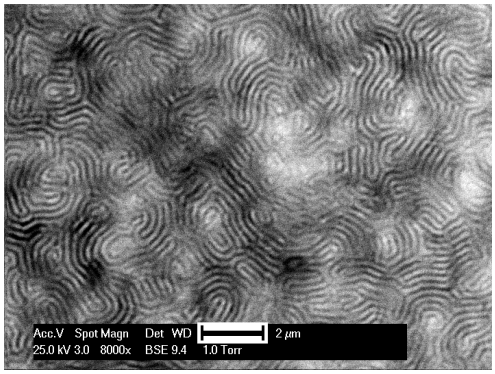

(b) Dark-field STEM image of unstained PS-block-PI

Figure 6.2: A comparison between SE and STEM images of an annealed, unstained symmetric PS-block-PI film. The SE image is the average of 8 712x484 images with a line scan time of 13.4ms. SE imaging was carried out with a beam energy of 10 keV and with 3 Torr/400 Pa of water vapour in the chamber. The STEM image was one single 712x484 image with a line scan time of 13.4ms. STEM imaging was carried out with a beam energy of 25 keV and 1 Torr/133 Pa of water vapour in the chamber. Scale bar = 2 μm in both cases.

for staining.

Assuming that the main process defining sample contrast is Rutherford scattering (equation 3.1), it should be possible to identify which polymer corresponds to the light and the dark phases in figures 6.2 and 6.3. Scattering (and therefore signal level in these images) is proportional to Z^2 and to the number of atoms present, so the relative ratio of each should be considered. The repeat unit of polystyrene is C_8H_8, while the repeat unit of polyisoprene is C_5H_8. This corresponds to an average Z^2 of 28.9 for polystyrene and 25.2 for polyisoprene. Furthermore, amorphous polystyrene has a density of 1050 kg m^{-3}, while polyisoprene has a density of 910 kg m^{-3}. Both of these factors contribute to the fact that polystyrene should scatter more strongly and

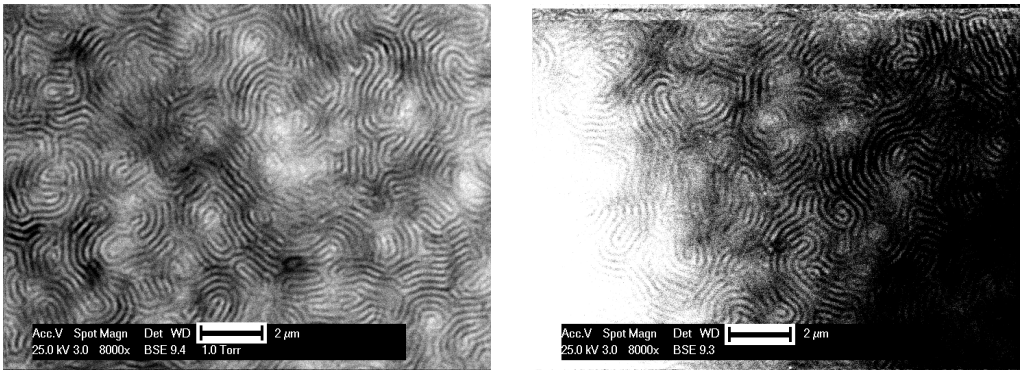

(a) 1 Torr water vapour **(b)** High vacuum

Figure 6.3: Dark-field STEM images of an annealed symmetric PS-block-PI film in both **(a)** 1 Torr/133 Pa of ambient water vapour and **(b)** high vacuum. Both images were one single 712x484 image with a line scan time of 13.4ms and taken at 25 kV. Scale bar = 2 μm in both cases.

therefore be the brighter phase in a dark-field STEM image (note, however, that the actual density of each phase here will be less than the bulk value because phases confined within the lamellar structure will not be able to relax and take their densest, least energy state).

This can be confirmed directly by imaging the asymmetric diblock copolymer. Because its chemical nature dictates that it will form hexagonally-packed cylinders of polyisoprene in a polystyrene matrix, it is possible to conclusively identify the phases based purely on their position in the image. The theory above would predict a dark-field STEM image of the asymmetric diblock copolymer film to have a light matrix with dark inclusions, which is seen in figure 6.4, confirming this identification.

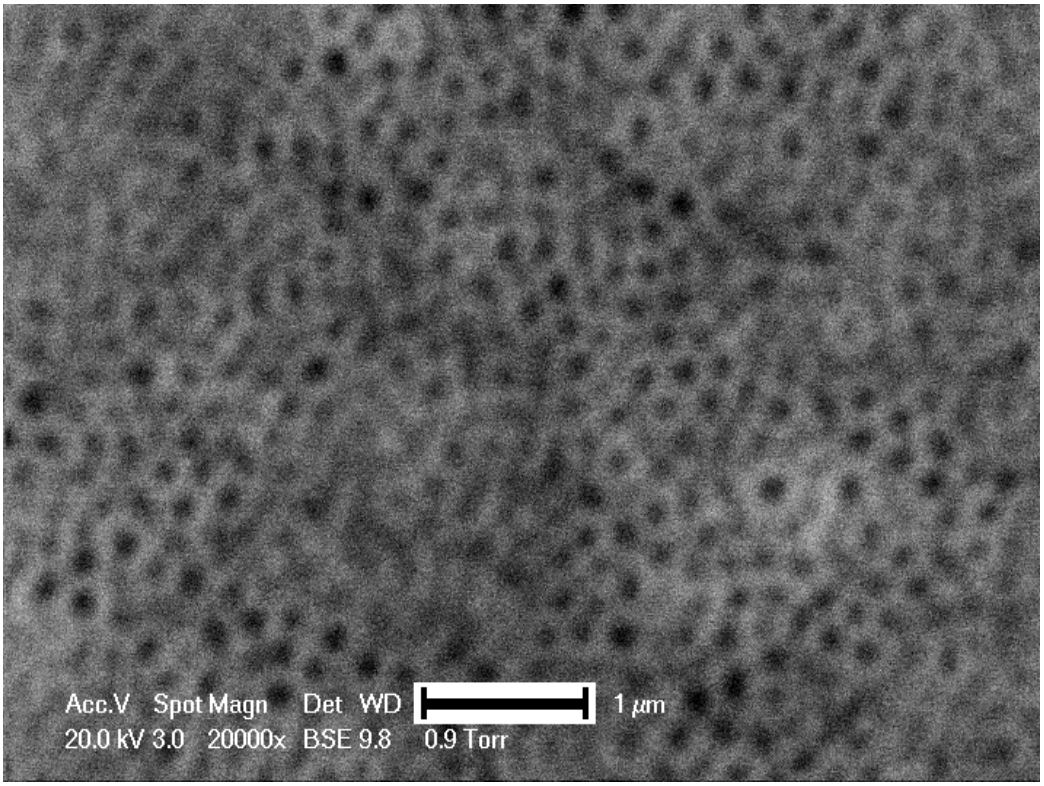

Figure 6.4: A dark-field STEM image showing an annealed asymmetric (majority phase: polystyrene) PS-block-PI copolymer film. Image was taken with an accelerating voltage of 20 kV, a chamber pressure of 1 Torr/133 Pa and was the average of 4 712x484 scans with a line scan time of 13.4ms. Scale bar is 1 μm.

6.3.3 The Effect of Staining

Since all the previous images taken in this chapter were of untreated polymer films but that in the literature, most polymer blends are first stained before imaging under (S)TEM, it is desirable to test the effects of staining - therefore, the popular heavy metal stain osmium tetroxide was used as a test case.

The literature is inconclusive about the effects of OsO_4 on polymers -

some have stained epoxy-rubber blends and found swelling in the stained component [94], while others have imaged stained and unstained styrene-isoprene block copolymers with phase-contrast TEM and found no difference in the feature sizes [90]. Again, OsO_4 will only react with the isoprene in this particular diblock copolymer, as polystyrene contains no isolated double bonds (OsO_4 will not react with aromatic systems).

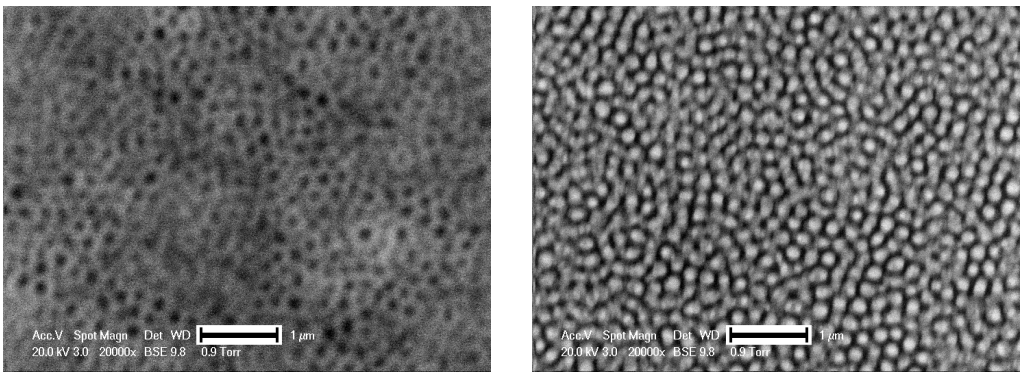

(a) Unstained asymmetric PS-block-PI **(b)** Stained asymmetric PS-block-PI

Figure 6.5: Dark-field STEM images of **(a)** unstained and **(b)** stained annealed asymmetric PS-block-PI film. Imaging was conducted with a beam energy of 20 keV, 1 Torr/133 Pa chamber pressure and as an average of four 712x484, 13.4ms/line images. Scale bars are 1 μm.

Figure 6.5 shows the effect of staining asymmetric PS-block-PI. The stained image (Fig. 6.5b) has a contrast reversal when compared to the unstained image (Fig. 6.5a), indicating that the addition of osmium is enough to overpower the "natural" contrast of this sample. Beyond that, little information can be obtained from the asymmetric sample - the structure is too disordered to provide direct information on length scales and the image Fourier transform does not contain peaks which are sufficiently well-defined for whole-image analysis.

The symmetric PS-block-PI (Fig. 6.6) is more interesting. When stained (Fig. 6.6b), there is an obvious change in the lamellar size. In agreement with

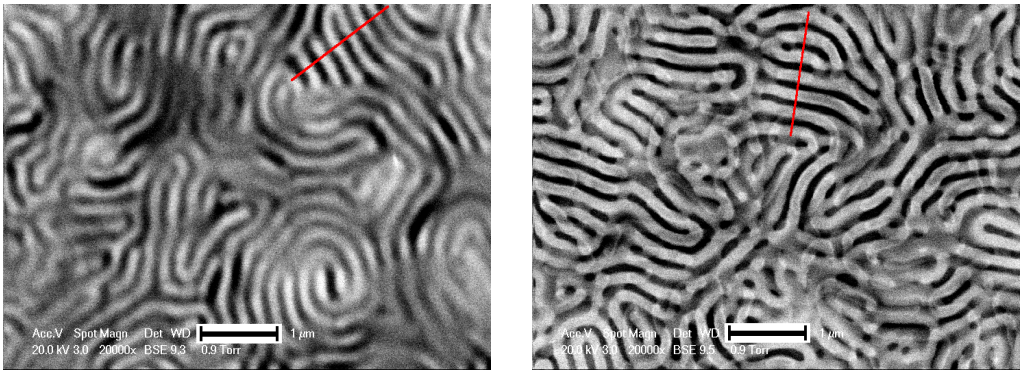

(a) Unstained symmetric PS-b-PI **(b)** Stained symmetric PS-b-PI

Figure 6.6: Dark-field STEM images of both **(a)** unstained and **(b)** stained annealed symmetric PS-block-PI. The lines drawn are examples of where line traces were taken for analysis. When comparing the images, be aware of the contrast inversion caused by staining - PS is the bright phase in the unstained sample, while PI is brighter in the stained sample. Imaging was conducted with a beam energy of 20 keV, 1 Torr/133 Pa chamber pressure and as a single 712x484, 13.4ms/line image. Scale bars are 1 μm.

the work carried out by Meyers et al [94], the stained phase (polyisoprene) has visibly swollen and now appears larger than the polystyrene, in comparison to the unstained sample (Fig. 6.6a) where both phases look identical.

To obtain numerical values from this information, multiple images, each of a different part of the sample, were taken of the symmetric stained and unstained samples. Line traces perpendicular to stacks of lamellae (see the red lines in Fig. 6.6) for each image were taken with the ImageJ software [95]. A custom-written C++ program using the FFTW library [96] was used to perform a discrete cosine transform on each line trace and select out either the largest peak in the power spectrum for the unstained sample (for which there was only one periodicity) or the two largest peaks in the case of the stained sample, rejecting any wavelengths over 300 nm to reduce errors due to uneven film thickness causing intensity fluctuations. The most significant

components in the power spectrum should correspond to the overall envelope of the lamellar shape, so a sample with two separate lamellar sizes should exhibit two large peaks - one each for the characteristic dimension of the larger and smaller spacings.

A point is designated as a peak by the analysis program if it is higher than its two neighbours. Only the peak's position is recorded - no attempt is made to calculate the peak's width, as their shapes are uneven. Hence, error values are gained from the statistics of multiple data points.

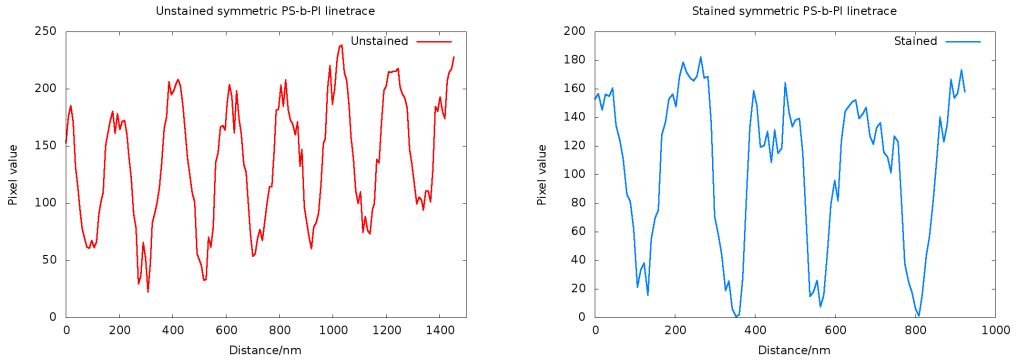

(a) Linetrace from unstained symmetric PS-b-PI

(b) Linetrace from stained symmetric PS-b-PI

Figure 6.7: Examples of linetraces from **(a)** unstained and **(b)** stained annealed symmetric PS-block-PI images.

Examples of cross-sections taken across the red lines in figure 6.6 are shown in figure 6.7. When viewed in this form, there is again an obvious difference between the unstained (Fig. 6.7a) and stained (Fig. 6.7b) samples, where the peaks and troughs are of different widths in the latter and very similar in the former.

This information can be further distilled by calculating a power spectrum of each linetrace, the data from figure 6.7 shown in figure 6.8 after performing a discrete cosine transform on it. Compared to the unstained sample, the

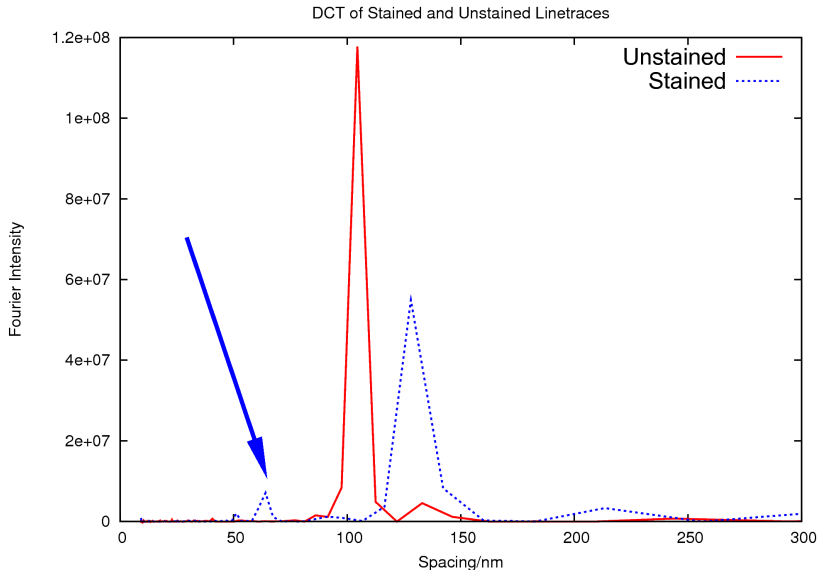

Figure 6.8: Discrete cosine transforms of the data in figure 6.7, overlayed on one another for easier comparison. Arrow indicates the second highest peak in the stained power spectrum.

stained sample's power spectrum has its largest peak at a higher spacing, clearly indicating the presence of swelling. Additional smaller peaks have appeared, the next tallest peak (indicated by the blue arrow) being located at a smaller spacing than the original unstained sample - indicating an apparent compression or a masking of the unstained phase behind a swollen stained phase.

The mean spacing for the unstained sample as well as the means of the larger and smaller distances for the stained sample are shown in table 6.1, along with their standard deviations. An additional program was written to analyse the linetraces directly and to attempt to pick out the size of "dark" and "light" regions directly, but due to the noisy nature of the linetraces, the errors from such a method are large. Despite these large errors, the results are included in table 6.1 to indicate clearly which phase has swollen. Both methods indicate a single lengthscale for the unstained sample and that the

Table 6.1: Lamellar spacings obtained from the discrete cosine transform of linetrace data for unstained and stained samples (single distance for unstained, lower and upper distances for stained) along with the results obtained by analysing the linetraces directly (dark and light sizes). For the discrete cosine transform method, 33 line traces from 9 image files were used to obtain the unstained sample's results and 97 line traces from 10 images were used to obtain the stained sample's results. For the direct analysis of linetraces, 10 traces from 5 image files were used to obtain the unstained sample's results and 86 traces from 10 image files were used to obtain the stained sample's results. Errors are one standard deviation.

Sample	Single/nm	Lower/nm	Upper/nm	Dark/nm	Light/nm
Unstained	113±6			110±23	114±27
Stained		81±26	130±19	98±21	131±26

action of staining significantly modifies this.

Staining the PS-block-PI film with OsO_4 causes the stained phase to swell by a factor of approximately 1.15, causing an apparent compression of the other phase to a scale of approximately 0.71 of its previous size as it does so. A visual inspection of the images (Fig. 6.6b) agrees with this data - the lighter (stained) phase clearly appears larger than the other to the eye, whereas the two were comparable before staining (Fig. 6.6a).

An alternative method of conducting this analysis was carried out by Spontak et al. [97], who took a histogram of the image and assigned the amount of space before and after the median point on the histogram to the relative ratios of each component. Spontak's method cannot be used to obtain a "second opinion" for this data, however - the images here do not have the right characteristics.

Having obtained an understanding of the effects of osmium staining on a plan-view image of the polymer film, a useful comparison can be made

between cross-sections of both stained and unstained films.

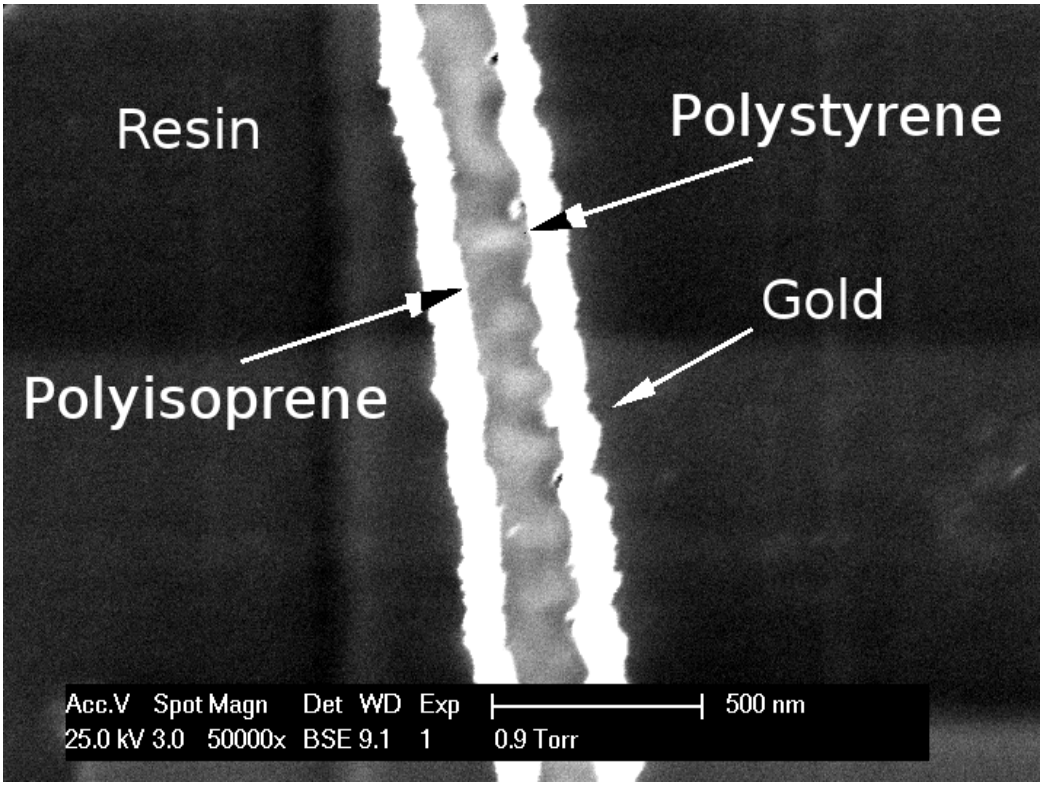

Figure 6.9: A cross-section through an unstained symmetric PS-block-PI film, taken using dark-field STEM. Imaging was conducted with a beam energy of 25 keV, 1 Torr/133 Pa chamber pressure and as a single 712x484, 40 ms/line image. Scale bar is 500 nm.

Figures 6.9 and 6.10 shows microtomed cross-sections through both unstained and stained resin-embedded symmetric PS-block-PI films (see part 6.3.1). Looking at the unstained film (Fig. 6.9), it can be seen that the film has both a smooth and a rough surface. This was probably caused during annealing - the smooth surface would most likely have been the one in contact with the glass slide and as such would be confined in-plane. The exposed surface of the film would have been afforded more freedom of movement and would therefore be able to extend out of the plane - this additional topography may help with providing contrast in SE mode (Fig. 6.2a) and would also affect

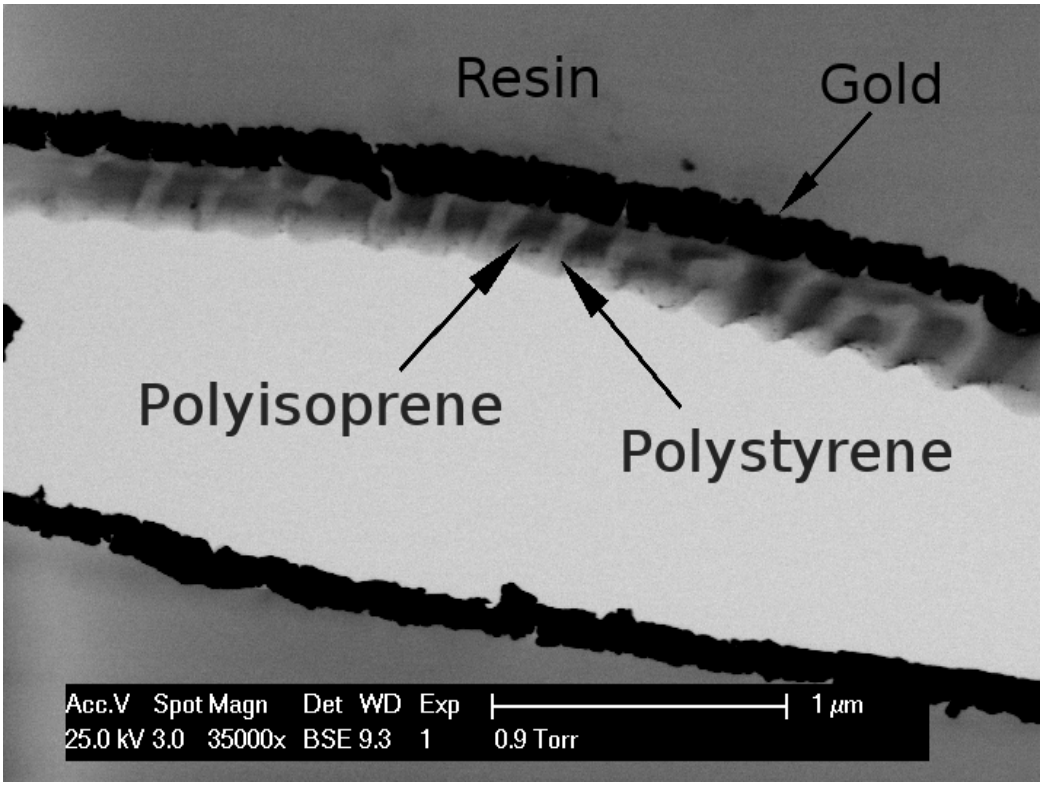

Figure 6.10: A cross-section through a stained symmetric PS-block-PI film, taken using bright-field STEM. Imaging was conducted with a beam energy of 25 keV, 1 Torr/133 Pa chamber pressure and as a single 712x484, 40 ms/line image. Scale bar is 1 μm.

AFM images.

While the contrast in figure 6.9 is not very clear, it can be seen that the two phases (polystyrene is light, polyisoprene is dark) are, if not exactly equal, quite comparable in width. By comparison, the widths of the polystyrene (light) and polyisoprene (dark) components in the stained film (Fig. 6.10) appear noticeably different, with the stained PI phase being visibly wider than the unstained PS phase. Although the polystyrene phase appears to extend out of the plane of the film for both the stained and unstained samples, these images are not clear enough to determine whether the

degree of extrusion differs between the stained and unstained samples.

Both programs used to analyse the polymer samples are included on the provided CD. linetracestatsdir1a.cpp is the program used to analyse the line traces directly, while fouriertracestatsdir.cpp and fouriertracestatsdir1a.cpp are two variants of the same program which takes the discrete cosine transforms used for figure 6.8. fouriertracestatsdir.cpp is used to analyse unstained sample (it provides the mean position of only the tallest peak), while fourierertracestatsdir1a.cpp is used to analyse stained samples - it provides the mean positions of the two tallest peaks, grouped into the mean of the shorter spacings and the mean of the longer spacings.

All the programs were written in C++ and compiled using GCC version 4.3.1 on a SuSE Linux 11.0 system. fouriertracestatsdir.cpp and fouriertracestatsdir1a.cpp additionally require the FFTW 3 library and were compiled against FFTW version 3.3.2. Compilation instructions can be found in the comments for each program. All programs are available under the GNU General Public License version 3, a copy of which is included along with the program code.

Each program will iterate through all the line trace files in its working directory. Line trace files are tab or space-delimited two-column files produced by ImageJ on an image which has been calibrated in nanometres. The results from each directory's files are output to the console, with power spectra from the fouriertracestatsdir and fouriertracestatsdir1a programs for each line trace saved as new files in the working directory.

6.4 Polymers: conclusion

Since the majority of polymers are electrically insulating, low atomic number materials, they cannot be imaged untreated with conventional SEM and exhibit little contrast when imaged under high-voltage (S)TEM. Charging

artefacts (Fig. 6.3b) cause severe problems for insulating polymers, while conventional SE imaging may fail to provide contrast between two different phases in a flat surface (Fig. 6.2a).

When imaged in an ESEM, charging is nullified (Fig. 6.3a) and the low beam voltage (see also part 3.1.1) allows contrast to be brought out between two materials with a very similar chemical composition (Fig. 6.2).

Because of this intrinsic contrast, staining with heavy metals is not necessary to observe the morphology of a styrene-isoprene diblock copolymer. When this block copolymer is selectively stained with osmium tetroxide, visible changes occurred with the stained phase increasing in size (Fig. 6.6), compressing and possibly extruding the unstained phase out of the plane of the film (Fig. 6.9 and 6.10).

This swelling has been quantified by means of Fourier analysis (Fig. 6.8), the aggregate statistics from 33 datasets for the unstained sample and 97 datasets for the stained sample showing that the stained phase (polyisoprene) expands by a factor of approximately 1.15, causing an apparent lateral compression of the other phase (polystyrene) to approximately 0.71 of its original dimension (Table 6.1). These findings therefore demonstrate that quantitative information obtained from stained TEM images as conventionally used in the literature may be misleading.

Chapter 7

Mammalian Cells

7.1 Biological Material and the Electron Microscope

Electron microscopy has been part of the cell biologist's repertoire since at least the 1950s [36]. Consequently, there is a great wealth of literature either containing electron images of cells or pertaining directly to the procedures used therein. Most of these images are taken using either stained thin sections and a TEM or dried, fixed and coated whole cells using an SEM. Due to ESEM's relative youth when compared to TEM and SEM, it was not applied to biological material until 1991 [98], when biofilms and diatoms (unicellular organisms) were imaged. Plants followed in 1993 [99] and animal cells in 1994 [100] for x-ray microanalysis and 1995 [101] for imaging.

This chapter will give an overview of the previous electron imaging methods used to image animal cells in the electron microscope and demonstrate the application of Wet STEM to one particular type of cell. The electron images in this chapter were taken using an FEI XL30 ESEM (FEI Company, Hillsboro, Oregon, US) equipped with a field-emission electron source. Con-

focal LASER scanning microscopy was carried out with a Zeiss Axioplan 2 fitted with a Zeiss LSM510 confocal module (Carl Zeiss GmbH, Oberkochen, Germany).

7.1.1 Structure of Mammalian Cells

In order to properly evaluate this technique and compare to previous work, the structure and composition of animal cells should be discussed so that the various techniques and their resulting images can be put in context. In its most basic state, a cell is a collection of functional components enclosed by a lipid bilayer called the plasma membrane. Plant cells and bacteria have an additional layer of polysaccharides outside of the membrane to provide structural support - this is called the cell wall.

There are two main categories of cell: eukaryotes (animals, plants and fungi, for example) and prokaryotes (bacteria and archaea). Eukaryotic cells are defined by the presence of "organelles" inside the cell - these are regions with a special functionality which are partitioned off from the rest of the cell by means of another lipid bilayer like the plasma membrane. Common organelles include mitochondria, which are used to convert food into usable energy (a molecule called adenosine triphosphate, or ATP), chloroplasts (found in plant cells), which carry out photosynthesis, and the endoplasmic reticulum, which has a role in protein production. All eukaryotes contain their genetic material inside an organelle called the nucleus. A more complete description of both prokaryotes and eukaryotes can be found elsewhere [102].

7.1.2 Traditional Cell Preparation for Electron Microscopy

Cells are wet, insulating and mechanically fragile. To survive exposure to the vacuum of an electron microscope, cells have traditionally been chemically fixed before imaging. A common method is to combine glutaraldehyde

or formaldehyde fixation, which immobilises proteins and nucleic acids, with osmium tetroxide fixation, which both immobilises and stains lipid membranes [36]. Together, these two chemicals serve to prevent cellular material from disintegrating under the vacuum.

Secondly, cells must be dehydrated carefully before imaging, since otherwise they will suffer considerable damage from rapid vapourisation or freezing of remnant cellular water upon exposure to the vacuum of the electron microscope. As with fixation, there are several methods of achieving this - serial immersion in a sequence of increasingly concentrated solvents, freeze drying and critical point drying are among those frequently used [36]. Care must be taken when dehydrating biological material, since the presence of a liquid-vapour interface leads to surface tension which can alter cellular structure.

An alternative method is cryo-fixation, which functions by freezing the sample so rapidly that its water is unable to form ice crystals and vitrifies in place [1]. If the sample is kept sufficiently cold (liquid nitrogen temperatures are commonly used), this vitreous ice will neither crystallise nor evaporate and as such the sample will remain intact under the vacuum of the microscope. Frozen samples can also be freeze-fractured - the fracture usually occurs along discontinuities within the cell, such as the lipid bilayer of a membrane. Freeze-fractured cells will therefore show a "surface" from their interior, allowing the surface structure of internal membranes to be examined.

For TEM usage, samples must be formed into thin slices to obtain the best image resolution. This is carried out by first infiltrating and embedding the sample with resin (this can take place at the same time as the dehydration step) to provide mechanical stability [36]. The embedded block of biological material can then be microtomed into thin slices (on the order of 100 nm thick) and imaged. TEM imaging may require additional staining to highlight components of interest within the cell beyond that of the mem-

branes highlighted by osmium fixation. Staining for selective components can be carried out using antibodies specific to the cellular component of interest attached to particles of heavy metal, such as gold or platinum [103].

SEM imaging requires samples to be conductive, as mentioned in part 1.4. Therefore, a metal layer (usually gold) is often sputter-coated on to the surface of a fixed and dried cell before SEM imaging takes place [1].

7.1.3 Mammalian Cells in the ESEM

As mentioned earlier, the first reference to the imaging of animal cells in an ESEM was in 1995 [101]. Furthermore, animal cells have been imaged when completely untreated using ESEM [104, 105] in the past, indicating that while they may not be alive after exposure to low vacuum [11] (determined by observing whether cells took up a compound called calcein-AM), they may at least retain their structure.

One important caveat is that in order to preserve the structure of these cells, they were kept in osmotically balanced culture medium or buffer solution. When this buffer solution is evaporated to expose the cell (see part 5.2 for a demonstration of why low atomic number samples need to be dry), large salt crystals will appear [11]. Because the contrast mechanism in Wet STEM has a much stronger dependence on atomic number than conventional ESEM, these crystals will obscure anything of interest which may lie beneath them.

Washing the cells with distilled water removes any solutes which might crystallise, but causes osmotic shock which rapidly damages both cell viability and structure [11]. This means that some form of fixation is required to carry out Wet STEM on animal cells, a step which has the additional useful property of slowing sample degradation under the electron beam and thus allowing images to be taken at higher magnifications where unfixed cells

would be damaged by the consequent increase in averaged beam intensity.

7.2 Wet STEM of Mammalian Cells

7.2.1 Sample Preparation

The cells used in this work were 3T3 fibroblasts, a standard cell line originally derived from mice [106]. They were cultured from frozen stock in Dulbecco's Modified Eagle Medium (DMEM, obtained from Invitrogen), to which was added 1% penicillin/streptomycin (Sigma-Aldrich), 10% fetal bovine serum (Invitrogen) and 1% glutamine (Invitrogen).

Cells in suspension were pipetted on to ethanol-sterilised Formvar-covered gold TEM grids sitting in well plates and cultured in a sterile incubator at 37°C for 2 days. Formvar support films were prepared by making a 1g/100ml solution of formvar (Agar Scientific) powder in chloroform, spin-casting for 20s at 3000 RPM on to 25x25mm glass squares, then scoring the films and floating them off on distilled water. 200-mesh gold grids (Agar Scientific) were placed on the floating films, which were then retrieved from the water using a glass cover slip.

After incubation, grids were removed from culture medium, washed once in phosphate-buffered saline (PBS) solution, immersed in a 4% solution of glutaraldehyde in PBS for 30 minutes at room temperature, then rinsed 5 times in PBS to remove any remnant glutaraldehyde. The resulting fixed cells were stored in PBS at 4°C for up to a week before imaging.

Cells to be imaged under confocal scanning microscopy were cultured as above, but instead fixed by immersion in a solution of 4% paraformaldehyde in PBS for 10 minutes at room temperature and washed three times for 5 minutes in PBS. The fixed cells were immersed in 10% normal donkey serum

in PBS for 1h at room temperature to mask general reactive groups from binding the antibody. Treated cells were then washed once with PBS for 5 minutes, incubated with a monoclonal mouse anti-ATP Synthase β antibody (Sigma-Aldrich, Gillingham, Dorset, UK) for 1h at 37°C, washed three times with PBS for 5 minutes, then incubated with goat anti-mouse antibodies conjugated with Alexa Fluor 488 fluorescent stain (Invitrogen, Carlsbad, California, USA) for 1h at 37°C. The cells were given a final wash three times in PBS for 5 minutes, then stored in PBS at 4°C until imaged. Since only mitochondria carry the protein ATP Synthase β, only mitochondria will be shown in a fluorescence image of these cells.

7.2.2 Wet STEM Procedure and Sample Images

The environmental conditions were adjusted so that the microscope chamber was in a slightly dehydrating state (see part 2.3) to ensure that water did not condense on the sample and interfere with imaging. The conditions used were 4 Torr/533 Pa and 3°C - this corresponded to a relative humidity of 72%. Before imaging, the buffer solution was washed from each grid by dipping it into distilled water.

Figure 7.1 shows an unstained animal cell with bright-field Wet STEM. The instrument does not have sufficient dynamic contrast range to show both the nuclear region and the extremities of the cell in the same image (compare Fig. 7.1a and Fig. 7.1b) - this is caused by large differences in thickness and hence beam attenuation between different parts of the cell.

Visible are the nucleus, its membrane, its nucleoli and an indistinct cloud on the exterior of the nucleus which is most likely the endoplasmic reticulum. Small, dense objects with a diameter of approximately 500 nm can be seen distributed throughout the cell. Their size indicates that they could either be mitochondria, whose higher scattering power could be due to their additional functionality as a store for calcium ions [102] (the size is comparable to that

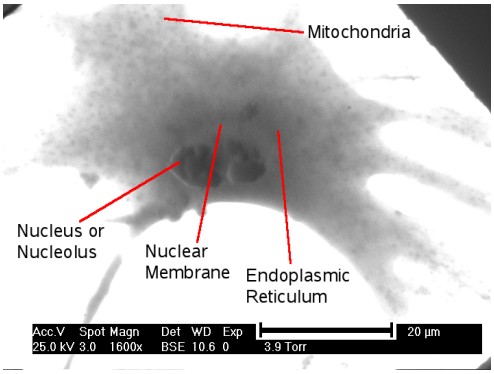

(a) 3T3 Cell, Nucleus

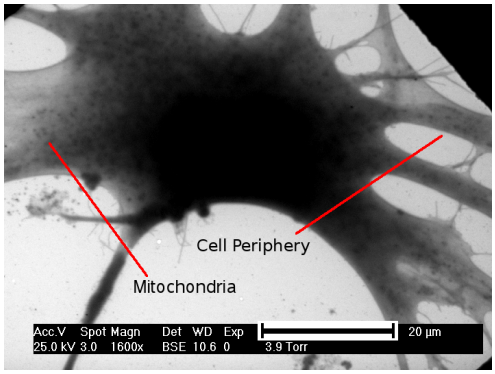

(b) 3T3 Cell, Body

Figure 7.1: Bright-field STEM images of a glutaraldehyde-fixed 3T3 fibroblast, with the amplifier settings adjusted to highlight details in (a), the nucleus and (b), the cell body. Both images were taken under mildly dehydrating conditions (3°C, 4 Torr/533 Pa). Scale bar = 20 μm in both cases.

observed with confocal fluorescence microscopy, see Fig. 7.2), or perhaps some sort of secretory vesicle (3T3 cells were originally fibroblasts, the purpose of which is to construct extracellular soft tissue).

Figure 7.2 shows a confocal scanning fluorescence microscopy image (see part 4.2.1) of another 3T3 cell, stained for mitochondria. The resolution of the mitochondria inside the cell appears broadly similar to, if somewhat poorer than the Wet STEM image (Fig. 7.1), but the limited depth of field available to this particular technique is made apparent in the top region of the cell, where it has grown out of the plane and the stained mitochondria can no longer be distinguished from one another.

Figure 7.3 shows that higher resolution images can be obtained from certain parts of the cell. Whilst imaging the main body of the cell at such magnifications is pointless due to beam spreading, the thinner extremities of the cell offer less impediment to the beam and as such can show greater detail. In this case, the thin processes are approximately 150 nm across. Their size

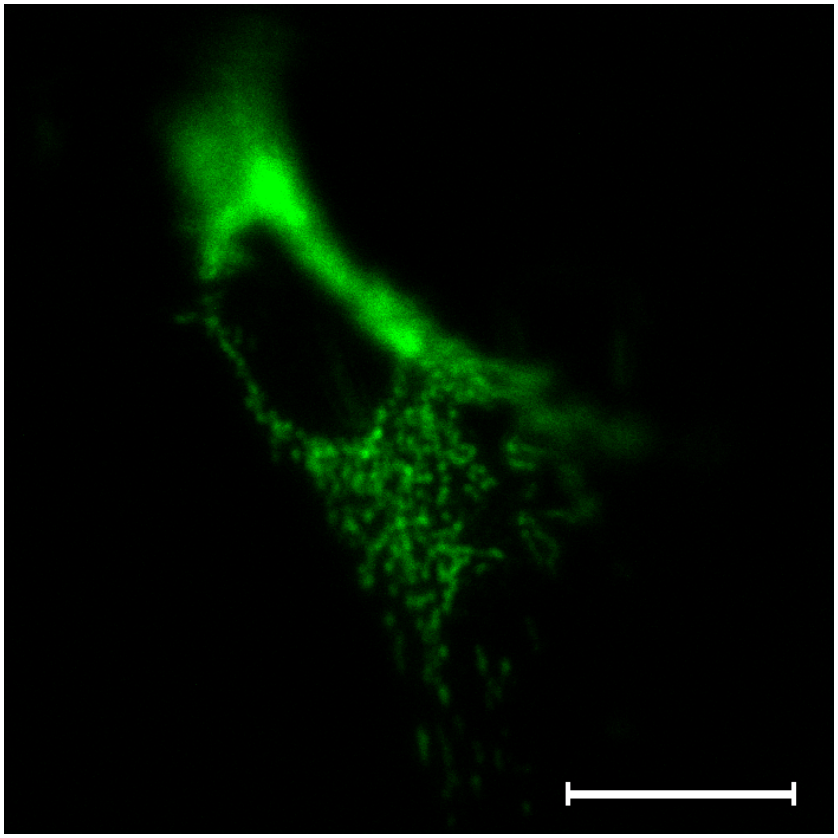

Figure 7.2: A confocal scanning fluorescence microscopy image of a 3T3 cell, stained for mitochondria. The scale bar is 20 μm.

implies [107] that these processes are probably filopodia - they act as feelers for cells which are growing and spreading across their substrate [108].

This particular image is dark-field (see part 3.1.1), as opposed to the bright-field STEM images used previously. Dark-field imaging was chosen in this case because of its higher signal to noise ratio (see part 3.2.2) - it has no impact on the achievable image resolution.

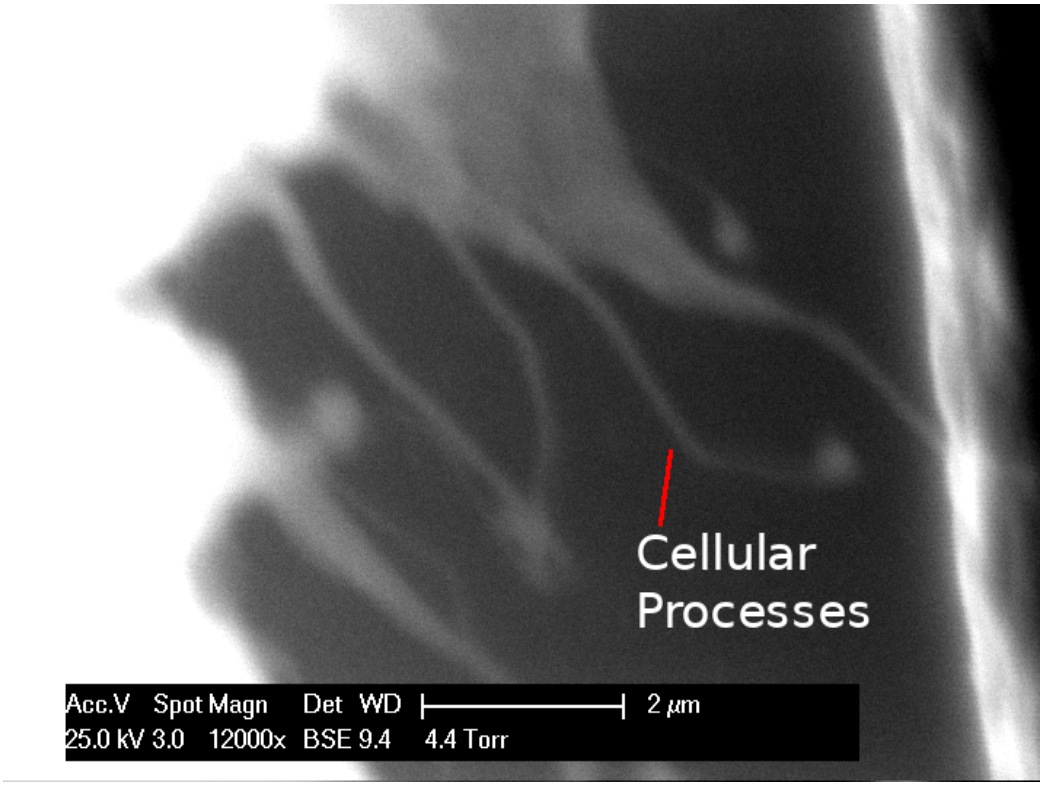

Figure 7.3: A dark-field STEM image of some thin processes at the very exterior of a glutaraldehyde-fixed 3T3 fibroblast. Microscope conditions were 1°C and 4.4 Torr, scale bar = 2 μm.

7.2.3 Effect of the Environment and Sample Preparation

Figure 7.4 demonstrates the necessity of chemical fixation. Even though the microscope was maintained at 100% humidity, the cell in figure 7.4a has not only ruptured, but the cell contents appear to have been dispersed across the support film. The only discernable feature is the nucleus and possibly the remnants of its attached endoplasmic reticulum - the cell itself no longer possesses a discernable boundary.

By comparison, the cell in figure 7.4b has been fixed, but was imaged

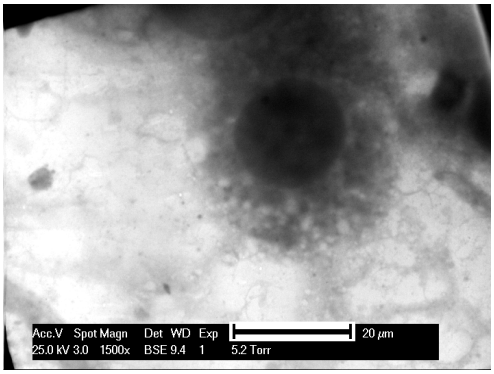

(a) 3T3 Cell, Unfixed

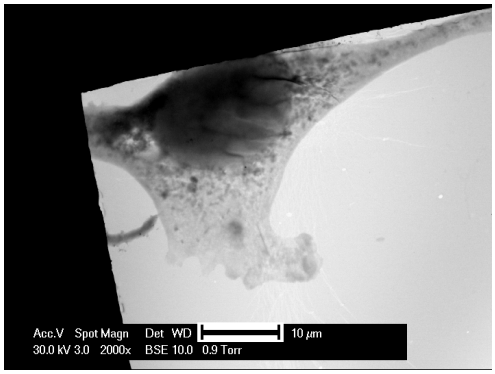

(b) 3T3 Cell, Fixed and Dehydrated

Figure 7.4: Bright-field STEM images of (a), an unfixed 3T3 fibroblast imaged fully hydrated (5.3 Torr/705 Pa and 2°C, relative humidity just below 100%) and (b), a fixed 3T3 fibroblast imaged at 1 Torr/133 Pa, purged (see part 2.3) 9 times from 2–9 Torr (266–1200 Pa) and with no temperature control (temperature is therefore around 20°C, with a relative humidity of 5.5%). Scale bar = 20 μm in (a) and 10 μm in (b).

in a severely dehydrating environment (1 Torr/133 Pa, 20°C). Although it appears considerably more intact than the unfixed cell in figure 7.4a, the nucleus appears wrinkled - this could be a collapse caused by the rapid loss of water resulting from the relatively harsh pumpdown procedure.

Figure 7.5 shows the effect of staining a glutaraldehyde-fixed cell with osmium tetroxide. Fixed cells on TEM grids were stained by immersion in a solution of 2% osmium tetroxide in water at room temperature for 10 minutes, then washed ten times for 1 minute each in fresh PBS to remove remnant OsO_4.

As mentioned earlier in part 1.4, osmium tetroxide attacks unsaturated carbon-carbon bonds, crosslinking two adjacent molecules or parts of a molecule, embedding the osmium atom within it and consequently increasing its electron scattering power. In cells, this staining corresponds mostly to mem-

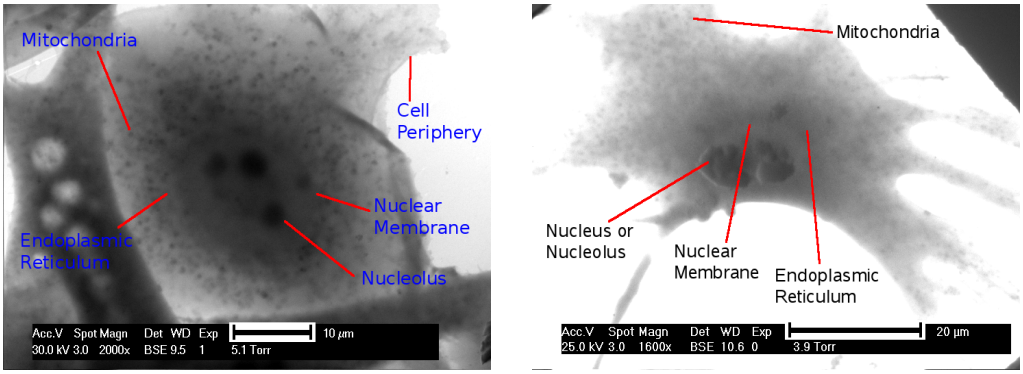

(a) 3T3 Cell, Fixed and Stained

(b) 3T3 Cell, Fixed Only

Figure 7.5: Bright-field STEM images of (a), a fixed and osmium-stained 3T3 fibroblast and (b), a fixed, but unstained 3T3 fibroblast (this is the same cell as in Fig. 7.1a). Both samples are imaged fully hydrated (5.3 Torr/705 Pa and 2°C, relative humidity just below 100%). Scale bar = 10 μm in (a) and 20 μm in (b).

branes and some proteins [102], which has the convenient effect of highlighting any partition between cellular compartments when thin sections of osmium-stained material are imaged with a TEM.

Because the cell in figure 7.5a has not been sectioned, there will be no regions where intracellular membranes are purely facing out of the plane and as such there are no clear delineations between intracellular compartments. The result of osmium staining is therefore to highlight regions which contain more lipid bilayer - key among those being mitochondria, which due to folding in their internal membrane [102], have an unusually large surface area available for staining.

The only difference between the two images in figure 7.5 is a possible compression in the sample's dynamic contrast range after staining - note that the entirety of the cell in figure 7.5a can be seen, whereas figure 7.5b only shows detail in its nucleus and the surrounding area (the thicker parts

of the cell) - see also figure 7.1 for an example of insufficient contrast range in the microscope, its effect being that only thin or thick parts of the sample can be imaged at any one time.

7.3 Mammalian Cells: conclusion

Wet STEM is capable of imaging animal cells (Fig. 7.1), but they must be chemically fixed (Fig. 7.4a) and imaged hydrated (Fig. 7.4b), with any remnant water evaporated before imaging can take place. The structures made visible to the microscopist are different to that of conventional (E)SEM, which reveals surface structure. The apparent resolution is superior to that of confocal scanning fluorescence microscopy (Fig. 7.2), visualising 150 nm wide processes (Fig. 7.3) with little difficulty. No staining is required to observe any of these features, although osmium staining may assist in other ways (Fig. 7.5).

Chapter 8

Bacterial Cells

8.1 The Bacterium

Mammalian cells and their associated preparation and imaging have already been discussed in chapter 7. While all cells are composed of the same basic materials (mostly nucleic acids, proteins, carbohydrates and lipids), bacteria are somewhat smaller than eukaryotic cells (on the order of 3 μm long, compared to an animal cell's typical diameter of 20 μm [102]) and have less internal structure.

As stated before (part 7.1.1), bacteria have a cell wall outside their lipid bilayer membrane to provide mechanical stability - a structure which mammalian cells lack. Some bacteria have an additional membrane on the outside of the cell wall, giving them a distinctive two-membrane structure which is visible when imaged with sufficient resolution [109]. Since bacteria are significantly smaller than eukaryotic cells, they do not exhibit as much internal structure or specialised compartments. While some functions are still preserved (for instance, bacteria also possess a cytoskeleton which serves much the same functionality as it does in eukaryotes [110]), other cellular functions must be achieved by simpler methods. For instance, while the genome of a

bacterium does float freely inside the cell, it is confined to a central region known as the nucleoid. Instead of using an explicit nuclear membrane, the bacterium accomplishes this by means of polymer chain physics [111].

8.1.1 Bacteria and Microscopy

The history of imaging bacteria with a microscope goes back to 1683, when Leeuwenhoek first described small organisms using his original apparati [102]. Since they are composed of the same types of material as eukaryotic cells, the methods used to image them are broadly similar. Light microscopy can be conducted on untreated bacteria in phase contrast mode for greater detail, or they can be made fluorescent either by staining or genetic engineering to image specific components (see part 4.2.1).

Electron microscopy is also routinely carried out on bacterial samples - potentially being more useful than for mammalian cells due to the smaller size of bacteria. Again, sample preparation is similar to that used for eukaryotes, with a few modifications to account for physical differences (animal and plant tissue can be prepared in blocks, while bacteria must be treated in suspension). For traditional electron microscopy, bacteria must be fixed and dried. They may be coated with metal as-is for imaging under SEM, or placed directly into an SEM for low-magnification imaging when charging or beam damage effects will not be significant.

TEM can be carried out on thin sections which have been treated either with a general stain (eg. osmium tetroxide for highlighting lipids) or by immunogold labelling to locate specific components of the cell. Since bacteria are thinner than mammalian cells, they can be imaged under TEM without sectioning (as has been carried out on a particular species of archaea [112]), although some staining may be required.

8.1.2 Bacteria and the ESEM

Bacteria, when compared to mammalian cells (see chapter 7), are more suited for immediate imaging with an ESEM. Since they have a cell wall, their exterior appearance and structure will be somewhat protected from both osmotic shock and moderate levels of vacuum damage. This means that although they may not be alive after exposure to ESEM operating pressure, beam radiation or ionisation-induced chemical attack [26], they will at least retain their shape [113].

The first published instance of applying ESEM to bacteria was in 1991 [98], where samples prepared with traditional SEM techniques were compared to bacteria which had only undergone a chemical fixation before imaging in the ESEM. Unfixed bacteria were later imaged in 2001, but only as a secondary part of an investigation into biofilms [114]. The first work explicitly dedicated to imaging of untreated bacteria with ESEM was in 2004 [115] and later expanded upon by the same group in 2005 [116], where endophytic bacteria were imaged with both environmental SEM and, after fixation and treatment, conventional SEM.

The advantages of using ESEM compared to conventional SEM are more pronounced for bacteria than they are for mammalian cells. Since not even a fixation step is required, bacteria can be imaged almost immediately (again, any culture medium is best removed beforehand to prevent crystallisation artefacts [11]) - a significant improvement when compared to fixation, dehydration and metal coating which is time consuming and requires additional equipment.

Wet STEM builds upon this by offering a different form of contrast than the SE imaging used in ESEM. As shown previously in chapter 5, STEM images not only have improved resolution and contrast when compared to SE images, but are also capable of showing information not present in an SE image (part 5.1.3).

8.2 Bacterial Culture and Sample Preparation

8.2.1 Bacterial Culture

Four species of bacterium were imaged for this work: *Escherichia coli* strain DH5α, *Cupriavidus necator* strains H16 (ATCC 17699) and PHB^{-}4, *Salmonella enterica* serovar Typhimurium strain SL1344 (both wild-type and Δ*mreC* mutant) and *Campylobacter jejuni* strains 81-176 (wild-type and Δ*kpsM* mutant) and 11168 (wild-type and Δ*kpsC* mutant). *E. coli* frozen stock was provided by Dr. Andrew Grant, Bacterial Infection Group, School of Veterinary Medicine, University of Cambridge and cultured by the author. The *C. necator* was grown and provided by Nick Thomson, BSS Group, Cavendish Laboratory, University of Cambridge. The *S.* Typhimurium and *C. jejuni* were grown and provided by Dr. Andrew Grant, Bacterial Infection Group, School of Veterinary Medicine, University of Cambridge.

E. coli is a standard laboratory organism and was used to establish a baseline for bacterial imaging. *C. necator* naturally produces a kind of plastic (polyhydroxyalkanoates, or PHA) which it uses as a food store [117, 118]. *S.* Typhimurium and *C. jejuni* are both pathogenic bacteria which are responsible for food poisoning.

E. coli strain DH5α was streaked out from frozen glycerol stock on to Luria-Bertani (LB) agar (Sigma-Aldrich, Gillingham, Dorset, UK) and incubated for 16h at 37℃. Colonised agar plates were stored in a 4℃ refrigerator for a maximum of 3 weeks before disposal. Liquid cultures were created by removing a single colony with an inoculation loop and growing in liquid LB medium (Sigma-Aldrich) for 16h at 37℃, shaking at 200 RPM throughout.

C. necator strains H16 (ATCC 17699) and PHB^{-}4 (kindly provided by Prof. Takeharu Tsuge, Tokyo Institute of Technology, Japan) were inoculated directly from frozen glycerol stocks to nutrient-rich medium for *C. necator* (composed of (g/L) tryptone (10), yeast extract (2) and meat extract (10))

and grown at 30℃ overnight, shaking at 250 RPM. They were then subcultured to nitrogen-limited mineral salts solution (MS), using an inoculation volume of 1%, and grown for a further 48h as before. The PHB^{-}4 strain of *C. necator* lacks a key enzyme in the production of polyhydroxyalkanoates (PHA) and as such does not produce and exhibit granules of PHA.

MS medium (pH 7) is designed to allow high-volume production of polyhydroxyalkanoates and consists of (g/L) $Na_2HPO_4{\cdot}12H_2O$ (9); KH_2PO_4 (1.5); NH_4Cl (0.5); $MgSO_4{\cdot}7H_2O$ (0.2); and 1 ml/L of trace element solution (containing (g/L) $FeCl_3$ (9.7); $CaCl_2$ (7.8); $CoCl_2{\cdot}6H_2O$(0.218); $CuSO_4{\cdot}5H_2O$ (0.156); $NiCl_3{\cdot}6H_2O$ (0.118) and $CrCl_3{\cdot}6H_2O$ (0.105) in 0.1 M HCl). Filter-sterilised fructose solution was used as the sole carbon source at a final concentration of 20 g/L.

S. Typhimurium strain SL1344 was cultured under the same conditions as *E. coli*. A Δ*mreC::kan* mutant was created and will be described in detail elsewhere (Bulmer *et al.*, submitted). Briefly, the lambda red one-step gene disruption method [119] was used to construct a Δ*mreC::kan* mutant in *S.* Typhimurium SL1344. This mutation leaves intact the first gene in the operon (*mreB*) which appears to be an essential gene, but disrupts *mreC* critical for assembly of the MreB-based cytoskeleton. The identity of the mutation was confirmed by PCR and DNA sequencing. Compared to wild-type *S.* Typhimurium, Δ*mreC* mutants are coccoid in shape and grow more slowly [110].

C. jejuni was routinely cultured on Mueller-Hinton (MH) Agar (Oxoid, Basingstoke, UK) supplemented with 5% defibrinated horse blood (hereafter referred to as MH blood agar plates) at 42℃ under microaerobic conditions (5% O_2, 5% CO_2, 5% H_2, 85% N_2) in a MACS VA500 Variable Atmosphere Workstation (Don Whitley, Shipley, United Kingdom). Liquid cultures of *C. jejuni* were grown in Brain Heart Infusion (BHI) broth (Oxoid) at 42℃ under microaerobic conditions with agitation at 150RPM. Both Δ*kpsC* and Δ*kpsM* mutations prevent *C. jejuni* from exporting the exterior polysaccha-

ride capsule [120, 121], but have no effect on the production of the capsule.

8.2.2 Bacteria Sample Preparation

As mentioned in part 8.1.1, bacteria must be resuspended in sterile distilled water (SDW) before imaging to prevent artefacts from solute crystallisation. 0.5 ml of bacteria in liquid culture medium are spun at 17,000 g for 1 min in a desktop centrifuge, replacing the supernatant with distilled water and vortex mixing until the pellet is re-suspended. This procedure is then repeated four times.

The resultant suspension is then diluted or concentrated with SDW to have on the order of 10^7 to 10^8 colony forming units (CFU) ml^{-1}. More than this will result in bacteria piling up and forming large, potentially multi-layered clusters which cannot be imaged to the same level of detail as smaller clusters or individual bacteria. Conversely, having too dilute a suspension can make it very hard to locate bacteria for imaging. ESEM work does not require any further preparation (for instance: dehydration, fixation, coating or staining).

8.2.3 Safety Issues when Handling Bacteria

E. coli and *C. necator* are both Hazard Group 1 organisms. Although their infection hazard is minimal, certain precautions must be taken when using them. Should they be spilled on any surface, that surface should be cleaned with a solution of 70% ethanol in water or 2% Virkon in water immediately to disinfect it. Materials which have contacted bacterial suspensions (such as pipette tips, TEM grids and gloves) should also be sterilised with either solution before disposal in a biological waste container.

Cleaning the interior of the microscope and any components that go inside

(such as the Wet STEM detector) was carried out only with 70% ethanol, since residue left by Virkon solution or any other cleaner that does not completely evaporate will contaminate the microscope. Since all ESEMs can be used as high-vacuum instruments, the microscope can be pumped down into high vacuum to inactivate any remnant micro-organisms. Testing with the XL30 ESEM (see part 8.2.4) showed that exposure to 15 minutes of vacuum at which the microscope would operate in conventional high-vacuum mode was sufficient to kill any aqueous *E. coli* DH5α - and therefore, sufficient to disinfect any spillage that may occur inside the microscope. The microscope was therefore kept at vacuum for at least 15 minutes before allowing access to the next user.

S. Typhimurium and *C. jejuni* are both Hazard Group 2 organisms and as such require more stringent controls. In addition to the procedures described above, the microscope room was sealed off during imaging to prevent access to those lacking the requisite biological safety training. All materials (pipette tips, gloves, samples) used during the experiment were sprayed with 70% ethanol, double-sealed and transported back to the School of Veterinary Medicine for sterilisation and disposal. The use of a lab coat was mandatory for Hazard Group 2 work. The effectiveness of vacuum sterilisation was not tested for *S.* Typhimurium or *C. jejuni*, however *C. jejuni* is known to be especially fragile against environmental hazards [122] when compared to other bacteria and *S.* Typhimurium is very similar to *E. coli* (Andrew Grant, personal communication). Pumping the ESEM into high vacuum for 15 minutes should therefore also be effective at inactivating remnant *S.* Typhimurium or *C. jejuni*.

8.2.4 Sterilisation at Microscope Vacuum Levels

The effectiveness of the microscope's vacuum system at inactivating remnant micro-organisms was tested via the following method: In an isolation cabi-

net, two sterile disposable inoculation loops were dipped in a suspension of *E. coli*in water suitable for imaging under Wet STEM. They were fastened securely inside a sterile, sealable box along with two other untouched disposable loops from the same pack. Each loop was given a different label. After transportation of the box to the microscope, the microscope chamber at high vacuum was vented with pure nitrogen and opened, then one sterile loop and one loop dipped in bacteria were taken out of the box (taking care to open it as little as possible) and fastened to a sample stub with a carbon tab, making sure that the loops did not touch anything.

After pumping the microscope down to minimum operating vacuum (10^{-2} Pa, indicated by the microscope software allowing the electron beam to be activated), it was left for 15 minutes after which time the microscope chamber was vented with pure nitrogen from a bottle and both loops removed to the sealable box. The box was then taken back to the bacterial culture facility, where all four loops were streaked out on to LB agar (Sigma-Aldrich) and incubated for 16h at 37°C.

Four samples were examined in total: an untouched loop left to sit for 15 minutes in the box (control null), one dipped in bacteria and left to sit for 15 minutes in the box (control positive), one untouched and exposed to vacuum for 15 minutes (vacuum null) and one dipped in bacteria then exposed to vacuum for 15 minutes (vacuum positive). Both inoculation loops exposed to vacuum resulted in no colonies growing on the agar, the control null formed 15 colonies and the control positive formed 252 colonies. A visual comparison between the loops showed the droplet of water still present on the control positive loop, whereas the vacuum positive's water droplet was found to have completely evaporated after the vacuum treatment. From these experiments it can be seen that an exposure of 15 minutes in high vacuum is sufficient to kill remnant bacteria if they are dispersed in water.

Additional tests of the same kind were carried out with bacteria in glycerol solution directly from frozen stock and from bacteria in culture medium.

The glycerol droplet was still present upon removal from the microscope and formed a very large number of colonies upon culturing, indistinguishable from the sample which was not exposed to vacuum. Upon removal from the microscope, the culture medium was found to have dried up into a fine powder on the end of the inoculation loop. Although bacteria did grow from the vacuum-treated culture medium, significantly fewer colonies grew from the vacuum-treated loop than from the loop which was not exposed to vacuum. These surviving bacteria were most likely from the inside of the droplet and consequently would have had a wall of dried culture medium form around them to offer protection against the worst of the vacuum's effects.

8.3 Imaging Bacteria with Wet STEM

Before conducting experiments on any particular sample, it would be useful to ascertain what contrast is available when imaging intact bacteria under low-voltage STEM, along with what effects the environmental changes offered by the ESEM may have on a bacterium's structure. To that end, *E. coli* will be used to demonstrate Wet STEM on bacteria - the differences between SE and STEM imaging, the effect of keeping bacteria hydrated or dehydrated and, for the purposes of aiding sample preparation, the effect of storing bacteria in liquids which are not osmotically balanced.

E. coli is a very well studied bacterium and is used as a model system for various aspects of cell and molecular biology. The strain used in this work, DH5α, is readily available, easily cultured and non-pathogenic. It is rod-shaped, has flagellae and exhibits no unusual features (compare with the PHA granules produced by *C. necator* in part 8.4.1).

The first imaging of bacteria using STEM in the ESEM was conducted by Bogner et al [38, 39], who used it as one of many test cases to illustrate the power of the technique. There, they imaged unprepared, live *Pseudomonas*

syringae immersed in water and were able to resolve its double-membrane structure at the points where bacteria touched one another. Since then, there has been very little published work applying Wet STEM to bacteria - only one piece reporting on its application to the same type of PHA-producing bacteria used in this work [123]. High-voltage STEM of intact bacteria has also been carried out using an environmental cell [124], however these bacteria were fixed and their exterior labelled with gold nanoparticles before imaging took place.

The procedure for imaging bacteria with Wet STEM is the same as with colloidal suspensions - resuspend in pure water and place a 0.3 μl droplet of suspension on a TEM grid in the Wet STEM detector. The environmental conditions (temperature, purge cycle, final pressure) can then be chosen and the microscope pumped down for imaging.

8.3.1 STEM and SE Imaging Compared

The first useful comparison would be between a secondary electron (conventional ESEM) and a STEM image of the same bacterium. As mentioned in parts 1.3.3 and 3.1.1, contrast in SE images primarily results from sample topography and differences in the electronic environment of the sample (allowing for more or less ionisation by the electron beam), while contrast in STEM images comes from differences in mass-density and atomic number.

On thin samples, however, both methods result in images which are quite similar. Figure 8.1 shows that for a single layer of bacteria, the bright-field STEM image appears like a contrast-inverted version of the SE image. This trend has been seen previously with the gibbsite (Fig. 5.1 and 5.4) where again, both SE and STEM images appeared similar.

For highly electron-transparent samples (either low atomic number or very thin, such as single bacteria or gibbsite plates), the sample will not

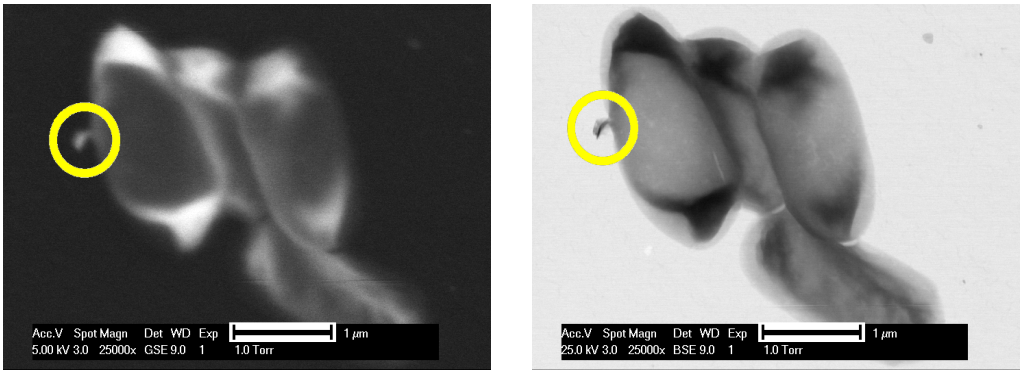

(a) *E. coli*, imaged with SE

(b) *E. coli*, imaged with STEM

Figure 8.1: Collapsed *E. coli* strain DH5α on a carbon film-coated TEM grid imaged using **(a)** conventional ESEM and **(b)** bright-field STEM in a dehydrated state (20℃, 1 Torr/133 Pa). No coating, staining or other such sample preparation has been carried out. Scale bars are 1 μm.

attenuate the beam quickly enough to stop secondary electron production from deeper regions of the sample - whether they are directly produced secondary electrons (known as SE1) or SEs produced from backscattered electrons (called SE2). If a sample is thin enough (half the electron range in that material, to a first approximation), the backscattered electron yield (and hence the SE2 yield) will increase directly with the material's mass-thickness.

Since STEM contrast also comes from mass-thickness, this results in the same features being shown in both SE and STEM images. The main difference between the two is that in both bacteria and gibbsite, the STEM image appears sharper than the SE image. This is primarily due to the improved signal to noise ratio given by STEM. Both images in figure 8.1 were taken in the same manner (712x484 image, 13.4 ms/line, 4-frame integration), but the SE image is considerably noisier than the STEM image and with less contrast. On very thin samples or those with a low atomic number, the SE yield is rather low - this is shown best on the edges of the bacteria, where the outer "shell" seen clearly with STEM is not visible in SE.

STEM also exhibits an innately higher resolution than SE imaging because of the nature of the interaction volume (see Fig. 1.5). While a bright-field STEM image can be formed solely from the unscattered portion of the beam after passage through the sample, SE images are formed by the region of the interaction volume which is within the escape depth of the material. On low atomic number samples like bacteria, this interaction volume may be quite large indeed and can blur out features of interest (see the circled region in Fig.8.1).

8.3.2 The Effect of Hydration

The second effect requiring investigation and the cause of the bacteria's internal structure in figure 8.1 is that of the ESEM's environmental control capabilities. Figure 8.1 was taken without concern for the hydration level - no temperature control, a nominal pressure (1 Torr/133 Pa) of water in the chamber and a harsh purge cycle (5 cycles of 2–9 Torr/266–1200 Pa) intended solely to ensure that the imaging gas was pure water. This resulted in a relative humidity level of approximately 6%.

Figure 8.2 shows the difference between bacteria which have been kept hydrated (1℃, 4 Torr/533 Pa, 6 purge cycles of 6–9 Torr/800–1200 Pa, 82% relative humidity) or dehydrated as in the case of figure 8.1 (room temperature, 1 Torr/133 Pa, 5 purge cycles of 2–9 Torr/266–1200 Pa).

Hydrated *E. coli* exhibit no internal details aside from a double-wall structure (indicated by the arrow in Fig. 8.2a, seen also in the initial work [38]). Bacteria do not have a compartmentalised internal structure in the same way that eukaryotic cells do [102] - while there is some segregation keeping the genome in one specific region called the nucleoid [125], it can be achieved using a combination of polymer physics (specifically, by modelling it as an elastic filament) and a few intra-genomic interactions [111] instead of any explicit nuclear membrane. Since the cytoplasm is relatively homogeneous in

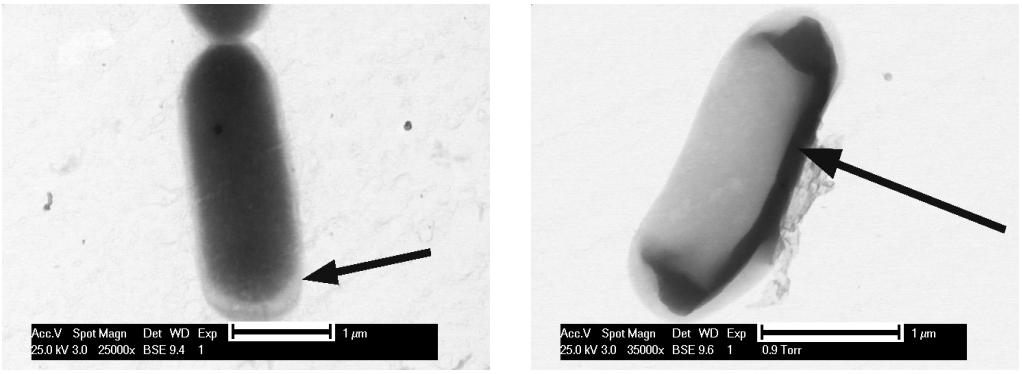

(a) *E. coli*, hydrated **(b)** *E. coli*, dehydrated

Figure 8.2: Bright-field STEM images of *E. coli* strain DH5α imaged under **(a)** hydrating conditions (1°C, 4 Torr/533 Pa) and **(b)** dehydrating conditions (20°C, 1 Torr/133 Pa). Scale bars are 1 μm.

both composition and density due to the lack of compartmentalisation, one would not expect to see much detail inside an unstained bacterium.

When *E. coli* are dehydrated according to the procedure used here, they collapse into a dense "backbone" of material running along the length of the cell and extending to the poles (indicated by the arrow in Fig. 8.2b).

To explain this, it would be useful to understand what happens when bacteria are dehydrated in this manner. One possible explanation is that there is a strong water flow out of the cell as the exterior pressure is dropped and that this water flow carries cellular components along with it. If these components can fit through pores in the cell membrane, they will be extracted from the cell (see the wispy threadlike parts to the right of the bacterium in Fig. 8.2b) - otherwise, they will remain inside the cell as it collapses.

As can be seen in figure 8.2b, the collapse is not uniform. Just like eukaryotic cells, bacteria produce cytoskeletal proteins [110] which by their very nature are rigid and resilient. It is possible that when a bacterium is collapsed via dehydration, these cytoskeletal elements keep their general shape (if not

their position - they generally span the entire cell in a helical pattern [110]). Since the individual filaments making up cytoskeletal elements are not large enough to form the "backbone" structure observed in figure 8.2b (a typical element, MreB [110], is very similar to actin whose filaments have a diameter of approximately 5 nm [102]), they will not be able to form the very visible contrast seen in figure 8.2b.

The source of the contrast along with the large size of the "backbone" is therefore most likely due to the other large components of the cell which are more free to move around. As the cell is collapsed, they will be drawn to and become entangled with the stationary cytoskeletal elements, forming a solid mass. This means that dehydration-induced collapse functions as a type of staining, highlighting parts of a cell which are more mechanically resilient than others. Again, since bacteria do not contain organelles, these large components will be molecular in nature - primarily the cell's DNA, any transcribed RNA sequences and large protein molecules (such as transmembrane proteins or ribosomes).

8.3.3 The Effect of Storage Media

As stated in part 8.1.1, cells must be suspended in pure water before imaging to prevent artefacts from solute crystallisation. Pure water, however, is very damaging to mammalian cells [126], swelling and eventually killing them via osmotic pressure. While the cell wall of a bacterium will prevent it from swelling, their internal structure may be affected by changes in the osmolarity of their environment.

Figure 8.3 shows the difference between *E. coli* stored for 5h in an osmotically balanced medium (phosphate-buffered saline, or PBS) and in sterile distilled water, both at 4℃. While the cells stored in PBS (Fig. 8.3a) appear very similar to those imaged freshly in figure 8.2a, bacteria which had been allowed to sit in water have a noticeably different appearance (Fig. 8.3b).

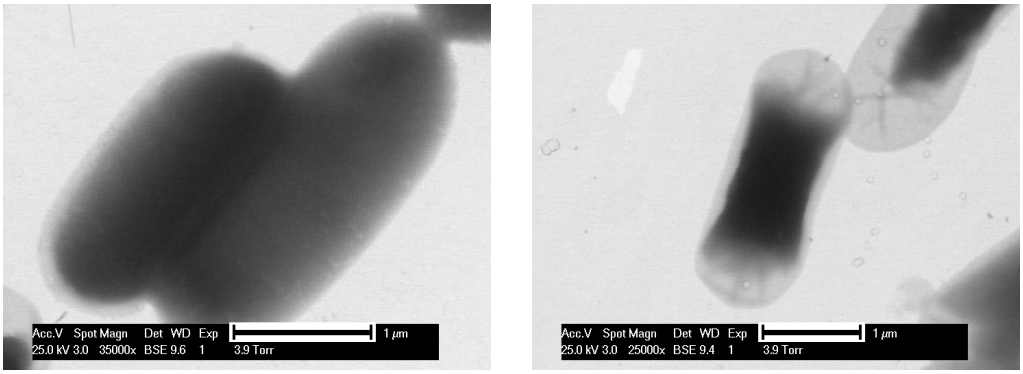

(a) *E. coli*, stored in PBS

(b) *E. coli*, stored in water

Figure 8.3: Bright-field STEM images of *E. coli* after storage for 5 hours at 4℃ in **(a)** phosphate-buffered saline (PBS) or **(b)** pure water, then imaged in a hydrated state (1℃, 4 Torr/533 Pa). Scale bars are 1 μm.

They have shrivelled away from their cell walls - a collapse which is both more uniform and with a different pattern to that seen in dehydrated bacteria (Fig. 8.2b).

Although bacteria are not damaged as much by osmotic shock as mammalian cells due to their cell wall, they are still sensitive to it and consequently are still subject to structural changes. Since the onset of visible differences is not instant (Fig. 8.2a was taken after the bacteria had been suspended in SDW for 45 minutes), there is a window in which imaging should be carried out after resuspension - certainly less than 5 hours and preferably as soon as possible to minimise damage or changes.

8.4 Specific Bacteria Imaged with Wet STEM

8.4.1 *C. necator*

With an understanding of the contrast mechanisms offered by Wet STEM on bacteria along with the effects made available by use of the ESEM's environmental control, the images produced by Wet STEM on different samples under varying pressure conditions can now be interpreted.

The first such sample is the bacterium *C. necator*. As mentioned earlier (part 8.2.1), *C. necator* naturally produces and stores a particular type of plastic inside itself as a food store. These granules have been imaged previously with TEM studies [127], however there are a number of disadvantages with traditional TEM techniques. Preparing TEM sections has a long, involved procedure associated with it - this has been covered already (part 1.4), but thin sections themselves present an additional issue for volumetric objects.

Because of their very nature, they only show the dimensions of an object in the particular plane at which it was sectioned. The apparent diameter of a spherical object (such as these PHA granules) varies depending on which point it is sampled at, meaning that multiple TEM sections from a collection of particles will need to be taken to obtain a true estimate of the particle size. Because Wet STEM images intact bacteria, any internal particles will be seen as their entire cross-section, allowing for an immediate estimation of both particle size and distribution within any one bacterium.

When attempting to engineer another species of bacteria to produce these plastics (such as *E. coli*, which is very easily cultured), it will be useful to know not only whether plastic is being produced (which can be ascertained via fluorescent staining and ordinary light microscopy) but also the size and distribution of the PHA granules within the cell. Wet STEM therefore offers a quick and effective method of inspecting bacteria for PHA accumulation.

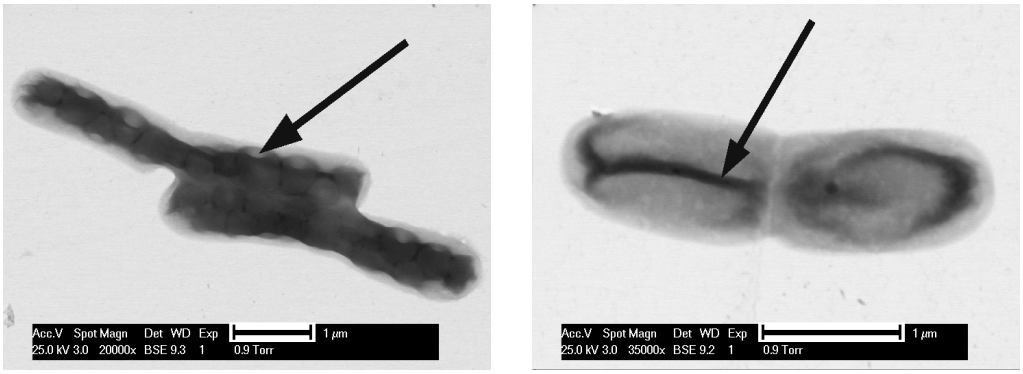

(a) *C. necator* H16 **(b)** *C. necator* PHB^{-}4

Figure 8.4: Bright-field STEM images of *C. necator* strain H16 grown in favourable conditions for PHA accumulation. The bacteria in **(b)** are mutated such that they lack the ability to produce PHAs. Both images show collapsed bacteria (20°C, 1 Torr/133 Pa). Scale bar = 1 μm in both cases.

Figure 8.4 shows the difference between two different strains of *C. necator*: the wild-type, which produces PHA granules (Fig. 8.4a) and a mutant (Fig. 8.4b), which lacks one of the key enzymes responsible for the production of PHAs [128]. Note that while the bacteria in figure 8.4 have been collapsed via dehydration, a collapse is not necessary to observe the presence of PHA granules and was carried out solely for the purpose of increasing the image contrast by accumulating cellular material around the granules.

A clear difference can be seen between the two different strains. *C. necator* strain PHB−4 (Fig. 8.4b) appears to exhibit the same kind of collapse as *E. coli* (Fig. 8.2b), possessing the same dense backbone (indicated by the arrow) with no other internal structure. Wild-type *C. necator* (Fig. 8.4a), on the other hand, contains a long chain of roughly spherical inclusions - these are the PHA granules. These granules are (0.41 ± 0.07) μm in diameter (mean of heights and widths from fitting ellipses to 20 granules).

Note that the wild-type *C. necator* has collapsed around the granules

rather than the obvious backbone as seen in mutant *C. necator* and the *E. coli*. This indicates that PHA granules are a more resilient structure than the cytoskeletal elements - they are solid accumulations of polymer and as such are mechanically different to the rest of the cytosol.

8.4.2 *S.* Typhimurium

The next test case is that of the bacteria *S.* Typhimurium, which is a leading cause of food poisoning throughout the world. A comparison was made of a wild-type strain of *S.* Typhimurium (SL1344) along with the same strain mutated to suppress transcription of the *mreC* gene (known as a $\Delta mreC$ knockout mutant), which has the effect of disrupting the MreB-based bacterial cytoskeleton. This mutation has two effects - firstly, it causes the rod-like *S.* Typhimurium to become coccoid and secondly, bacteria mutated like this grow more slowly [110].

Figure 8.5 shows wild-type and $\Delta mreC$ *S.* Typhimurium in both hydrated and collapsed states. The most obvious difference between the two strains is their shape - mutants are round while wild-type *S.* Typhimurium are rod-like. This can be seen quite easily with light microscopy, but the ESEM's pressure control offers additional sources of information.

The differences between rod-like and coccoid *S.* Typhimurium are made apparent in figure 8.5, with figures 8.5a and 8.5b presenting an immediate difference between wild-type and $\Delta mreC$, respectively. Even when hydrated, a difference between the rigidity of the bacteria can be seen - the wild-type strain in Fig. 8.5a maintain their rod-like shape even when touching, but the $\Delta mreC$ strain in Fig. 8.5b deform when brought into contact, some of them even becoming concave (see the arrow in Fig. 8.5b) in response to the contact forces applied.

When *S.* Typhimurium are dehydrated, they are seen to collapse around

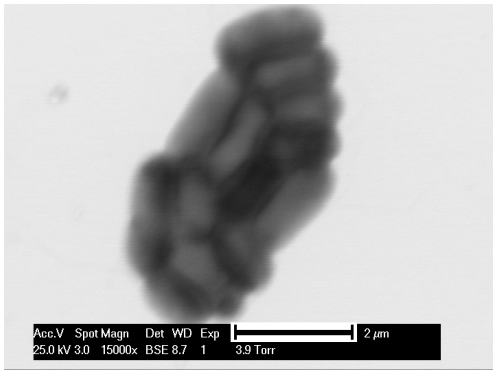

(a) *S.* Typhimurium, wild-type and hydrated

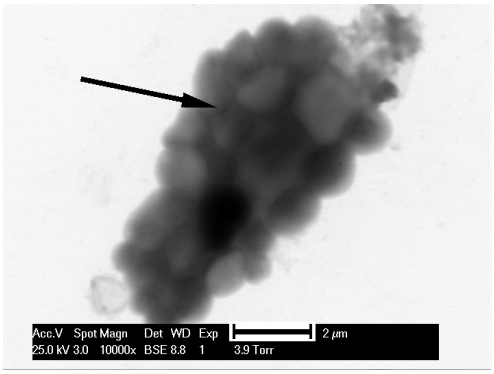

(b) *S.* Typhimurium, Δ*mreC* and hydrated

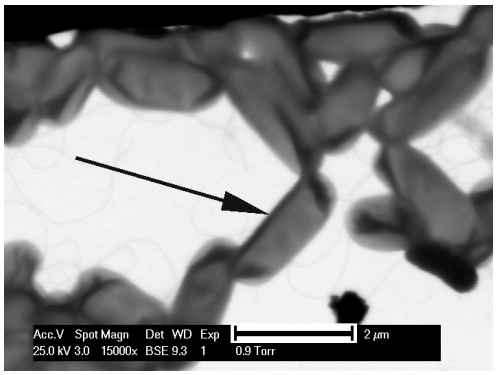

(c) *S.* Typhimurium, wild-type and collapsed

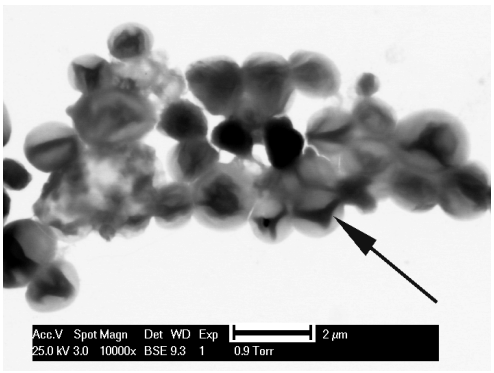

(d) *S.* Typhimurium, Δ*mreC* and collapsed

Figure 8.5: Bright-field STEM images of wild-type and Δ*mreC* strain SL1344 *S.* Typhimurium bacteria under hydrated (1℃, 4 Torr/533 Pa, Fig. **(a)** and **(b)**) and dehydrating (20℃, 1 Torr/133 Pa, Fig. **(c)** and **(d)**) conditions. The arrow in (b) indicates at point where one of the bacteria has deformed into a concave shape after contact with another bacterium, while arrows on dehydrated bacteria indicate the position of collapsed material. Scale bars = 2 μm.

or into a band of denser material running throughout the cell in much the same way as *E. coli*. Wild-type *S.* Typhimurium almost exclusively forms

a band around its inner edge (indicated by the arrow in Fig. 8.5c, again compare to the *E. coli* in Fig. 8.2b), but the Δ*mreC* mutant is seen either to lyse under the strain (see the leftmost part of Fig. 8.5d) or collapse into a centrally positioned lobed band (indicated by the arrow in Fig. 8.5d).

The Mre family of proteins act to give shape to the bacterium [110], with MreB being an actin-like protein that serves to provide rigidity and structure, and MreC being an anchor that holds MreB to the cell membrane. MreD is less well understood, but recent work [129] postulates that it helps to direct the assembly of the cell wall along the axis of MreB. As in the collapsed *E. coli* (Fig. 8.2b), the contents of the cell are most likely clustering around rigid cytoskeletal elements (such as MreB) to provide the image with contrast.

The difference between the two cell types lies in how the MreB is organised. MreC acts as an anchor for MreB - although MreB is still being produced (bacteria cannot survive without it), it is no longer being attached to the cell's perimeter and is therefore most likely going to be floating freely inside the cytoplasm. This means that when Δ*mreC S.* Typhimurium collapse, the collapse pattern will not be localised to the cell perimeter and will instead be an irregular accumulation in the middle of the cell. Additionally, the lack of a reinforcing endoskeleton (if that term can be used) would also explain why Δ*mreC S.* Typhimurium lyse more easily (Fig. 8.5b, top-right). Without a rigid network supporting the membrane, the bacteria will undergo more severe deformations in response to stress and thus be at greater risk of rupturing.

8.4.3 *C. jejuni*

The final test case is *C. jejuni*, another major cause of food poisoning throughout the world. It usually exhibits a helical structure, but it can also take on rod-like [130, 131] or coccoid [132] shapes when under oxidative stress or starvation, respectively, and usually has one flagellum extending out from

each end of the bacterium. *C. jejuni* also exhibits an extracellular layer of polysaccharides [133] (the capsule), which may be removed via mutation.

C. jejuni has been imaged with ESEM and Wet STEM previously in the Cavendish [126], where a preliminary investigation into ESEM's capabilities on this particular bacterium was made. The previous work showcased both SE and STEM modes of ESEM and investigated a variety of microscope conditions (beam energy, beam current and a gentle decrease in chamber pressure) and their effects on the imaging of both wild-type, $\Delta kpsC$ and $\Delta kpsM$ *C. jejuni*.

This work will focus explicitly on applying Wet STEM and the dehydration-induced collapse methods demonstrated earlier in this chapter to *C. jejuni*. Using the information obtained from *E. coli* and *S.* Typhimurium earlier, deductions about the interior structure of wild-type and mutant *C. jejuni* in its various forms will be made.

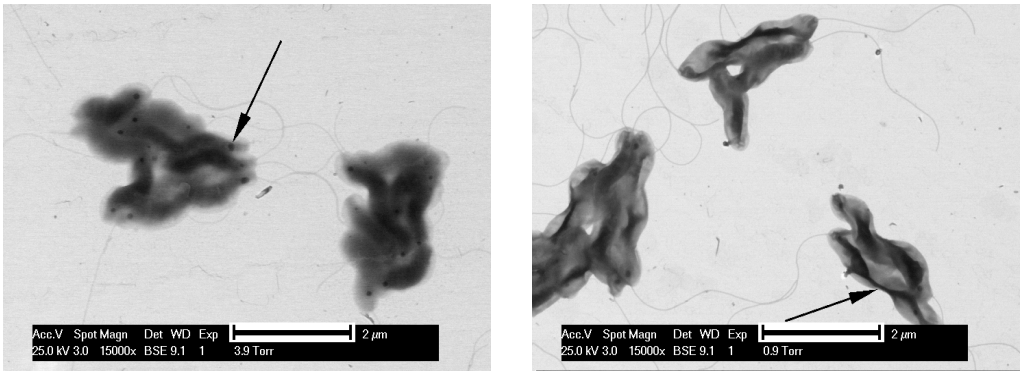

(a) 81-176, hydrated

(b) 81-176, dehydrated

Figure 8.6: Bright-field STEM images of *C. jejuni* strain 81-176 imaged under **(a)** hydrated (1°C, 4 Torr/533 Pa) and **(b)** dehydrated (20°C, 1 Torr/133 Pa) conditions. Arrow in **(a)** indicates dense inclusions (see also fig. 8.7), while the arrow in **(b)** shows the central helical collapse pattern. Scale bar = 2 μm in both cases.

Figure 8.6 shows wild-type *C. jejuni* strain 81-176 under Wet STEM. The helical shape of the bacteria is readily visible in both hydrated (Fig. 8.6a) and collapsed (Fig. 8.6b) conditions, along with a large quantity of flagellae (with an approximate diameter of 20 nm, a value which agrees with previously published literature [134]).

Compared to the thin edge-bound collapse pattern of *E. coli* and *S.* Typhimurium (see Fig. 8.2b), wild-type *C. jejuni* tend to collapse into a thicker central core - this could be indicative of either a stronger central structure, a more resilient outer component (potentially the capsule) which protected the interior from the worst effects of the dehydration or possibly even remnant water in the microscope causing a slower, gentler dehydration and collapse procedure.

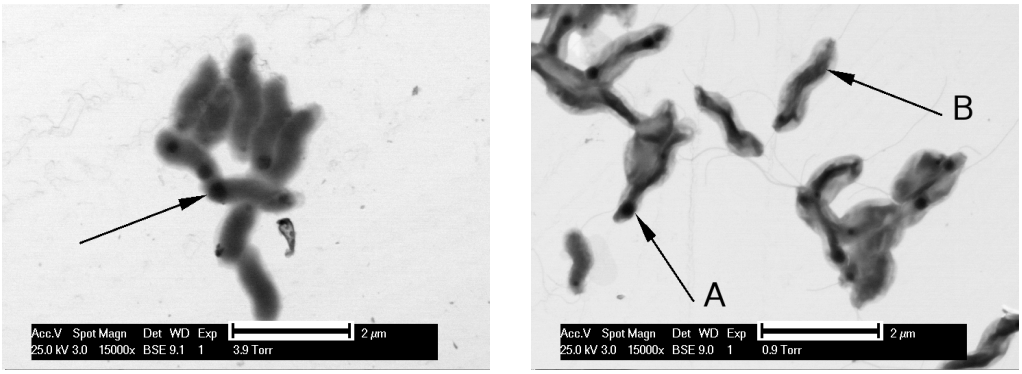

(a) Δ*kpsC* 81-176, hydrated

(b) Δ*kpsC* 81-176, dehydrated

Figure 8.7: Bright-field STEM images of Δ*kpsC C. jejuni* strain 81-176 imaged under **(a)** hydrated (1°C, 4 Torr/533 Pa) and **(b)** dehydrated (20°C, 1 Torr/133 Pa) conditions. The arrow in **(a)** indicates a dense inclusion. Arrow A in **(b)** indicates a dense inclusion, while arrow B in **(b)** indicates a central helical collapse pattern (see also Fig. 8.6b). Scale bar = 2 μm in both cases.

Figure 8.7 shows strain 81-176 of *C. jejuni* mutated to inactivate the *kpsC* gene, which is responsible for one of the steps in assembling the exterior

polysaccharide capsule of *C. jejuni* [121] - this mutant therefore lacks the capsule.

The most obvious difference between $\Delta kpsC$ and wild-type *C. jejuni* is the presence of large, dense inclusions within the cell. The most likely explanation for these inclusions is that they are a buildup of capsule material which cannot be exported (as the exporter protein is not being produced) and hence accumulates inside the cell. While they can be seen in wild-type *C. jejuni* (see Fig. 8.6a), these "nodules" are significantly smaller and less common than they are in the capsule-negative strains.

As has been mentioned earlier in this section, when *C. jejuni* is exposed to an oxygenated environment, it changes shape from a helix to a rod-like structure [130] which although viable, is significantly less infectious than the helical form [131]. Neither the exact mechanism by which this shape change occurs nor the reason for it occurring are presently known. By collapsing rod-like *C. jejuni* with the ESEM's pressure control, information can be obtained about the bacterial cytoskeleton in both rod and helix phases.

Figure 8.8 shows $\Delta kpsM$ *C. jejuni* strain 11168 which grew with rod-like morphology. While both wild-type and capsule-negative mutants exhibited rod shapes, more of the mutant bacteria were rods and as such they were chosen in preference for imaging.

Hydrated rod-like *C. jejuni* (Fig. 8.8a) do not exhibit any important distinguishing features over other rod-like bacteria - while they still have polar flagellae and denser "nodules" towards the poles, this only helps to identify them as *C. jejuni* and does not provide any information about their transformation.

Collapsed rod-like *C. jejuni* (Fig. 8.8b) potentially offer a little more information. When helical *C. jejuni* collapse (Fig. 8.6b), the collapse pattern is a central core which is also helical in shape. The natural rod-like bacteria imaged so far (Fig. 8.2b for *E. coli* and fig. 8.5c for *S.* Typhimurium) have

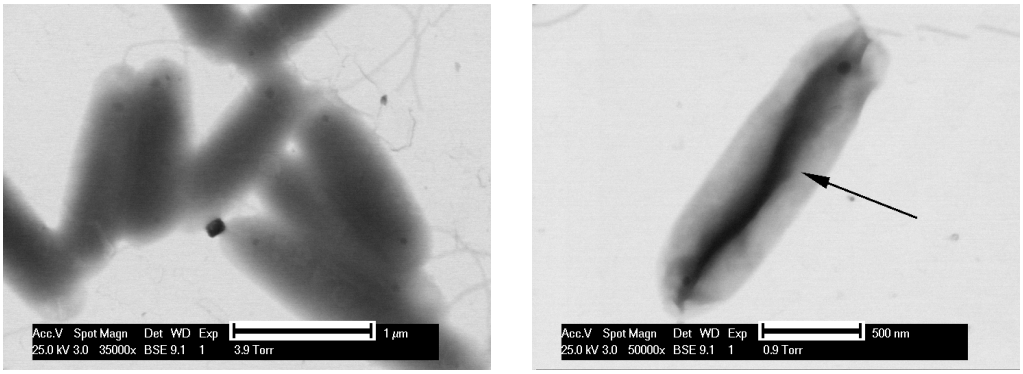

(a) Δ*kpsM* 11168, hydrated **(b)** Δ*kpsM* 11168, dehydrated

Figure 8.8: Bright-field STEM images of rod-like Δ*kpsM* *C. jejuni* strain 11168 imaged under **(a)** hydrated (1°C, 4 Torr/533 Pa) and **(b)** dehydrated (20°C, 1 Torr/133 Pa) conditions. The arrow in **(b)** indicates a central linear collapse with a faint, but visible helical structure. Scale bar = 1 μm in **(a)** and 500 nm in **(b)**.

a collapse pattern which is one dense strand running along one edge of the bacterium, usually connected to a pair of denser regions at the poles.

Rod-like *C. jejuni* collapse more like helical *C. jejuni*. In figure 8.8b, the collapse pattern is central (like the wild-type *C. jejuni*), but has a definite helical appearance to it. This would indicate one of two things: either that the core cytoskeleton of *C. jejuni* is helical by nature, is retained as it changes from helix to rod and is stiffened somehow during the transition to rod-form. Alternatively, the *C. jejuni* cytoskeleton could be naturally linear (like *E. coli* and *S.* Typhimurium) but forced to coil up upon itself by means of tension applied to it through some additional proteins. When it is placed under oxidative stress and changes from helix to rod, some of these proteins may become unbound and allow the "natural" linear skeleton shape to become more apparent.

Finally, under conditions of starvation [132], *C. jejuni* may also become

coccoid. When in the coccoid form, its genome is found to be degraded [122] - combined with the observed release of cell contents into the extracellular medium, this is perhaps indicative of cell death.

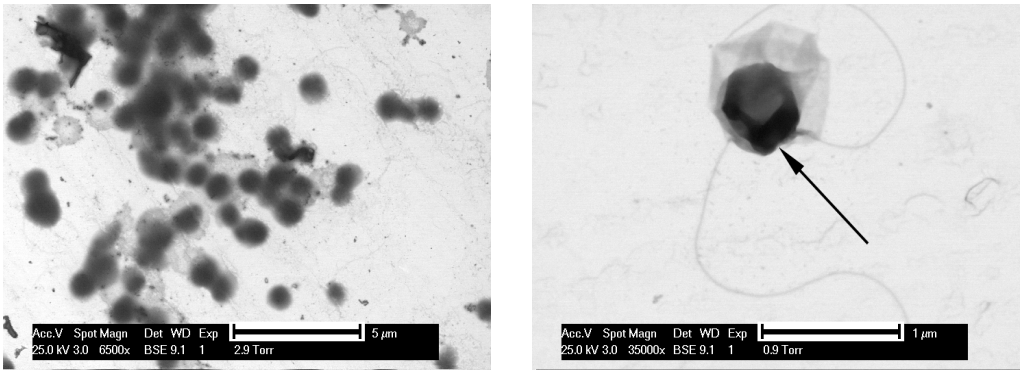

(a) *C. jejuni* 11168, hydrated **(b)** *C. jejuni* 11168, dehydrated

Figure 8.9: Bright-field STEM images of coccoid *C. jejuni* strain 11168 imaged under **(a)** hydrated (1°C, 3 Torr/466 Pa) and **(b)** dehydrated (20°C, 1 Torr/133 Pa) conditions. The arrow in **(a)** indicates a curved collapse pattern. Scale bar = 5 μm in **(a)** and 1 μm in **(b)**.

Figure 8.9 shows coccoid-form *C. jejuni* strain 11168, both hydrated (Fig. 8.9a) and dehydrated (Fig. 8.9b). Since 4h had passed between re-suspending the bacteria and imaging them in a hydrated state, it is likely that there is some osmotic damage in figure 8.9a (see part 8.3.3).

While the cells in figure 8.9a are coccoid, their appearance is closer to spiral or rod-like *C. jejuni* than it is to the hydrated *S.* Typhimurium coccoids seen in figure 8.5b. They exhibit the same dense core coupled with a less dense "halo" as seen in wild-type spiral *C. jejuni* (Fig. 8.6a). Also apparent is the presence of debris on the support film - coccoid *C. jejuni* has been previously reported to disintegrate under centrifugation [122].

Dehydrated coccoid *C. jejuni* (Fig. 8.9b) also appear different to their *S.* Typhimurium counterparts. While $\Delta mreC$ *S.* Typhimurium collapses into

a central lobed region (Fig. 8.5d), coccoid *C. jejuni* instead collapses into a shrivelled circular region around the perimeter of the collapsed "core".

The collapse pattern here may indicate something about the nature of shape changing in *C. jejuni*. If we assume that the shape changes in *C. jejuni* are actively driven and given that coccoid *C. jejuni* are in a state of either extreme starvation or cell death [132, 122], then it stands to reason that a coccoid form is the most relaxed state of *C. jejuni* and therefore the most relaxed or the resting form of its cytoskeleton.

Coccoid *C. jejuni* collapses into a C-shape or broken ring (Fig. 8.9b). This provides an alternative explanation for the shape-changing behaviour of *C. jejuni*. If the natural, "as-formed" state of the cytoskeleton is a broken ring, both helical and rod shapes can be obtained by taking each end of the ring and pushing the two ends apart in a direction perpendicular to the plane of the ring. This explains the helical appearance in collapsed rod-like *C. jejuni* (Fig. 8.8b) - it is the original cytoskeleton's coiled structure at full extension.

There are two possible explanations for why *C. jejuni* under oxidative stress extends fully - firstly that there is some sort of ratchet mechanism (possibly a short binding protein) which can "catch" the cytoskeleton at maximum extension and hold it there. The purpose of this would be to stop the cell from expending energy in maintaining the cytoskeleton in a state of extension when it is under oxidative stress, freeing cellular resources for other tasks. The second, simpler mechanism is that when the cell receives more oxygen than it is accustomed to, the extension/twisting mechanism becomes overactive as a result and forces the cell into a fully extended state.

8.5 Bacteria and Wet STEM: Conclusions

Due to their high level of electron transparency and mechanical resilience when compared to mammalian cells (Chapter 7), bacteria are an excellent prospect for Wet STEM imaging. The resolution and contrast offered by Wet STEM is clearly superior to that obtained from SE images (Fig. 8.1) of uncoated bacteria (see also the previous work on bacterial ESEM carried out in this group [126]). Bacteria with a potential pre-existing internal structure (part 8.4.1) can be taken from culture and imaged within minutes at high resolution. Should the cell of interest not exhibit internal features naturally, the pressure control afforded by the ESEM offers a new method of contrast on intact, otherwise homogeneous bacteria (Fig. 8.2).

When wild-type and cytoskeletal-deficient *S.* Typhimurium are collapsed via the use of low pressure (Fig. 8.5), an obvious difference in the internal structure can be seen between the two. The cytoskeleton in the particular type of mutant *S.* Typhimurium used in this work is not anchored to the cell wall, which is made apparent in the images taken of collapsed *S.* Typhimurium (Fig. 8.5d).

Furthermore, both differences and similarities in the internal structure between various forms of *C. jejuni* are made apparent on both hydrated (Figs. 8.6a and 8.7a) and collapsed (Figs. 8.6b, 8.7b and 8.8b) samples. Coccoid *S.* Typhimurium and *C. jejuni*, when both collapsed and hydrated, appear completely different to one another under Wet STEM. Using light microscopy, they would appear identical and require culturing, antigen response testing or other biochemical methods to identify.

Finally, using the ESEM to drive collapse, a hypothesis as to how *C. jejuni* creates and maintains the various forms of its structure has been developed.

Since the STEM images in this work are of completely untreated bacteria, they provide non-specific information about the bacterium and its general

structural properties (the location and shape of any resilient elements). The theories presented in this chapter would therefore be greatly improved by staining relevant components of the cell (for instance, cytoskeletal proteins) with either fluorescent or immunogold labelling so that correlative imaging can be carried out.

Chapter 9

Conclusions and Further Work

9.1 Conclusions

Wet STEM is not so much a completely new technique as it is an extension to ESEM, sitting alongside secondary electrons, backscattered electrons and X-rays in the list of different signals available to the microscopist. Compared to the other imaging methods available in the ESEM, it presents its own advantages and disadvantages - it requires a thin enough sample to allow beam penetration, but in turn allows details to be seen even in parts of the sample which are buried. Because thin samples are used, the reduced beam spreading (see part 3.3) offers a potentially higher resolution than SE imaging of bulk samples.

Wet STEM therefore shares its main uses and benefits with ESEM - sample preparation is either eliminated or vastly simplified, less effort needs to be made towards charge control and samples can be imaged in an environment which more closely resembles their native state, allowing for the observation of active processes or samples with fewer potential artefacts from sample preparation.

Each sample showed different aspects of Wet STEM's capabilities. The findings from each sample are summarised in order of their appearance in this work:

Wet STEM's capacity to image multi-layer samples from above was showcased in the chapter on colloidal suspensions (Chapter 5), where not only stacks of material were imaged in their entirety (see part 5.1.2), but also objects submerged in water (see figures 5.2 and 5.9). Electron microscopy need not consist of static samples, as illustrated in figure 5.3 where submerged gibbsite particles were observed to move between frames due to Brownian motion. Finally, to highlight the difference in contrast generation between STEM and SE or BSE imaging, diffraction-induced bend contours (part 5.1.3 can also be seen on sufficiently crystalline materials.

Polymer films (Chapter 6) were a more straightforward sample. Low-voltage STEM provides significantly greater contrast than secondary electrons (Fig. 6.2), but the sample used (a composite of polystyrene and polyisoprene) is highly insulating and as such requires ESEM's charge neutralisation capabilities (Fig. 6.3). Because no staining was required to image this polymer, unstained and stained samples could be compared, showing that osmium tetroxide swells the (stained) phase with which it reacts (Fig. 6.6).

Mammalian cells (Chapter 7) are significantly more fragile than the previous samples, requiring both fixation and a high humidity (Fig. 7.4) to preserve their structure. As with the polymer films, no staining is required to reveal the internal structure of a fibroblast cell (Fig. 7.1), but osmium staining (which mostly affects lipid membranes) does help by compressing the image's dynamic contrast range (Fig. 7.5), allowing more of the cell to be seen in the same image (although the same information is still available without staining). Because mammalian cells are usually quite thick (assuming that the nuclei are spherical, they will be approximately 8 μm thick at maximum), some sections will see a decline in resolution due to beam spreading, though thinner regions of the cell (Fig. 7.3) may be imaged at higher

resolution.

Bacteria (Chapter 8), due to the nature of their cell walls, are more tolerant of environmental conditions than mammalian cells. Because of this, the environment can be manipulated to collapse bacteria, creating a notably different structure to that of an intact cell (Fig. 8.2). Since bacteria are relatively thin, the SE image has a large influence from the mass-thickness of the cell and therefore appears similar to dark-field STEM but with less resolution, contrast and signal-to-noise level (Fig. 8.1).

Collapsing bacteria has been shown to reveal interesting facts about their internal structure, with a cytoskeletal-deficient mutant of *S.* Typhimurium having a visibly different collapse pattern to the wild-type bacterium (Fig. 8.5). Similar information can be inferred about *C. jejuni*, which assumes several forms depending on its situation. By collapsing *C. jejuni* in several of its forms (coccoid, helical and rod), it was theorised that the "resting" form of its cytoskeleton is a split ring (Fig. 8.9), which is then extended linearly perpendicular to the plane of the ring to form helical (Fig. 8.6) and then rod-shaped (Fig. 8.8) bacteria, depending on the degree of extension.

Related to changes caused by collapse is the effect of osmolarity. If bacteria are not in an isotonic medium, they will be visibly altered (Fig. 8.3), causing artefacts which may hamper imaging. While perhaps not as important for collapsed bacteria as it is for hydrated bacteria, non-isotonic storage media are still a potential source of artefacts and should be avoided if at all possible.

The prime benefit of the ESEM and therefore Wet STEM regarding bacteria is that of rapid imaging. Samples can be taken from culture and imaged within fifteen minutes, whether intact or collapsed and without requiring any particular treatment such as fluorescent or heavy metal staining. Collapsing bacteria with vacuum or dehydration can of course be carried out in other instruments and then the collapsed bacteria imaged with high-vacuum TEM

or STEM. However it is both more convenient and easier to control when conducted in-situ using an ESEM.

9.2 Further Work

The results in this work are intended as a preliminary investigation into how Wet STEM can be applied to various samples. Consequentially, no one sample has been examined in depth and as such several questions remain unanswered.

When imaging the paint samples (part 5.2), some of the dried paint films were found to have straight lines of dense material in a hexagonal pattern, surrounding the individual paint particles. While they did not appear in every sample (see Fig. 5.8 for an example), their nature is unknown. It would therefore be useful, in terms of obtaining a greater understanding of Wet STEM's contrast, to conduct further study on the paint sample or analogues. Likewise, the edges of gibbsite plates appeared to become blurred as the beam energy decreased (Fig. 5.4). The cause of this blurring is not immediately obvious and should be explored.

A more detailed look into how effectively the beam penetrates various thicknesses of different material would also be useful - a potential application for Wet STEM is the imaging of submerged objects and to that end, it is necessary to know how much water can cover an object while still leaving it visible.

Polymer samples can be imaged straightforwardly enough, but the literature is not in agreement on the subject of stain-induced swelling. Because of this, further information is needed on the precise effects of staining - cross-section images of stained and unstained films are potentially less ambiguous than plan-view images (such as those obtained from STEM or AFM of unbroken films), especially if the film does not consist solely of perpendicular

lamellae (see Fig. 6.10).

Mammalian cells have a very complicated internal structure. While dense objects were seen in the cytoplasm (Fig. 7.1), their identities cannot be ascertained purely by Wet STEM of unstained cells. This could potentially be clarified by fluorescently labelling various components of the cell and then examining the same cell under both confocal light microscopy and Wet STEM. Immunogold labelling could alternatively be used to eliminate the need to co-register images, but distinguishing between labelled and natural dense regions might pose problems. If a consistent mapping of STEM scattering power to individual cell components can be found, imaging of mammalian cells could potentially be greatly accelerated by eliminating the staining steps.

Looking at the results obtained so far from imaging bacteria, three possible avenues of further work present themselves. Firstly is to use the ESEM's pressure control more finely on wild-type and capsule-negative mutants of *C. jejuni*. By gently dehydrating and re-hydrating the bacteria, it might be possible to swell and contract the capsule and obtain a direct measurement of its size when in its natural, fully hydrated state.

Secondly is to test the *C. jejuni* structure hypothesis. If it becomes rod-like by tightening its cytoskeleton, the cytoskeleton and hence the bacterium as a whole should be stiffer when rod-like than when in helical or coccoid forms. If the bacteria are immobilised, an AFM could theoretically be used to obtain force-response measurements from each different shape of *C. jejuni*. Additionally, correlative imaging with stained (either fluorescent staining and confocal microscopy or immunogold labelling and (S)TEM) images of *C. jejuni* in its different shapes could be used to ascertain the form and location of the cytoskeleton.

Thirdly would be to continue the line of work carried out on the *S.* Typhimurium and investigate the effect of mutating or suppressing various different cytoskeletal genes on the bacterium's collapse pattern. Again, fluo-

rescence imaging would prove useful in identifying the location of each cytoskeletal protein in both hydrated and collapsed states.

Bibliography

[1] Watt, I. M., *The principles and practice of electron microscopy* (Cambridge University Press, 1997), 2nd edition. 2, 4, 5, 6, 7, 8, 9, 10, 12, 21, 22, 32, 37, 38, 68, 103, 104

[2] Goldstein, J. I., Newbury, D. E., Echlin, P., Joy, D. C., Fiori, C. and Lifshin, E., *Scanning Electron Microscopy and X-Ray Microanalysis* (Plenum Press, New York, USA, 1981). 3, 13, 15, 17, 49

[3] Everhart, T. E. and Thornley, R. F. M. (1960). Wide-band detector for micro-microampere low-energy electron currents. *Journal of Scientific Instruments*, **37(7)**:246. URL http://stacks.iop.org/0950-7671/37/i=7/a=307. 5

[4] Sawyer, L. C., Grubb, D. T. and Meyers, G. F., *Polymer Microscopy* (Springer, 2008). 18, 21, 39, 77, 78, 79, 87

[5] Danilatos, G. D. and Robinson, V. N. E. (1979). Principles Of Scanning Electron Microscopy At High Specimen Chamber Pressures. *Scanning*, **2(2)**:72–82. 23

[6] Danilatos, G. D. (1980). An atmospheric scanning electron microscope (ASEM). *Micron (1969)*, **11(3-4)**:335–336. URL http://www.sciencedirect.com/science/article/B6X3X-474XY6C-6S/2/f62e4f824417998e3a2e2ab1554ea176. 23, 35

[7] Stokes, D. J., Thiel, B. L. and Donald, A. M. (1998). Direct observation of water-oil emulsion systems in the liquid state by environmental scanning electron microscopy. *Langmuir*, **14(16)**:4402–4408. 24

[8] Bache, I. C. and Donald, A. M. (1998). The structure of the gluten network in dough: A study using environmental scanning electron microscopy. *Journal Of Cereal Science*, **28(2)**:127–133. 24

[9] Cowan, A. J., Wilson, N. H. F., Wilson, M. A. and Watts, D. C. (1996). The application of ESEM in dental materials research. *Journal of Dentistry*, **24(5)**:375 – 377. doi:DOI:10.1016/0300-5712(95)00088-7. URL http://www.sciencedirect.com/science/article/B6T86-3W254G7-F/2/75a0aea8fb22293f970ec0ed1c9be48c. 24

[10] Neubauer, C. M. and Jennings, H. M. (1996). The role of the environmental scanning electron microscope in the investigation of cement-based materials. *Scanning*, **18(7)**:515–521. 24

[11] Kirk, S., Skepper, J. and Donald, A. (2009). Application of environmental scanning electron microscopy to determine biological surface structure. *J Microsc*, **233(2)**:205–224. URL http://dx.doi.org/10.1111/j.1365-2818.2009.03111.x. 24, 104, 115

[12] Meredith, P., Donald, A. M. and Payne, R. S. (1996). Freeze-drying: In situ observations using cryoenvironmental scanning electron microscopy and differential scanning calorimetry. *J Pharm Sci*, **85(6)**:631–637. 24

[13] Millar, G. J., Nelson, M. L. and Uwins, P. J. R. (1998). In situ observation of structural changes in polycrystalline silver catalysts by environmental scanning electron microscopy. *Journal Of The Chemical Society-Faraday Transactions*, **94(14)**:2015–2023. 24

[14] Schmid, B., Aas, N., Grong, O. and Odegard, R. (2001). In situ environmental scanning electron microscope observations of catalytic processes

encountered in metal dusting corrosion on iron and nickel. *Applied Catalysis A-General*, **215(1-2)**:257–270. 24

[15] McGregor, J. and Donald, A. (2010). ESEM imaging of dynamic biological processes: the closure of stomatal pores. *J Microsc*, **239(2)**:135–141. URL http://dx.doi.org/10.1111/j.1365-2818.2009.03351.x. 24

[16] Philips Electron Optics (1996). Environmental Scanning Electron Microscopy: An Introduction to ESEM. Philips Electron Optics, Building AAE, P.O. Box 218, 5600 MD Eindhoven, The Netherlands. 25, 34

[17] Danilatos, G. D. (1993). Introduction to the ESEM Instrument. *Microsc Res Tech*, **25(5-6)**:354–361. 26, 32

[18] User Matthieumarechal on Wikipedia. (2008). URL http://en.wikipedia.org/wiki/File:Phase-diag2.svg. 27

[19] FEI Company (2005). *The Quanta 200 3D User's Operation Manual*, 4th edition. 28

[20] Royall, C. P. and Donald, A. M. (2002). Optimisation of the environmental scanning electron microscope for observation of drying of matt water-based lacquers. *Scanning*, **24(6)**:305–313. 28

[21] Cameron, R. E. and Donald, A. M. (1994). Minimizing Sample Evaporation in the Environmental Scanning Electron-Microscope. *J Microsc*, **173**:227–237. 28

[22] Fletcher, A. L., Thiel, B. L. and Donald, A. M. (1997). Amplification measurements of alternative imaging gases in environmental SEM. *J Phys D: Appl Phys*, **30(15)**:2249–2257. 29

[23] Danilatos, G. D. (1988). Foundations of Environmental Scanning Electron Microscopy. *Adv Electron Electron Phys*, **71**:109–250. 30

[24] Grubb, D. T. (1974). Radiation damage and electron microscopy of organic polymers. *J Mater Sci*, **9(10)**:1715–1736. URL http://dx.doi.org/10.1007/BF00540772. 32

[25] Jenkins, L. M. and Donald, A. M. (1997). Use of the environmental scanning electron microscope for the observation of the swelling behaviour of cellulosic fibres. *Scanning*, **19(2)**:92–97. 32

[26] Royall, C. P., Thiel, B. L. and Donald, A. M. (2001). Radiation damage of water in environmental scanning electron microscopy. *Journal Of Microscopy*, **204**:185–195. 32, 115

[27] Toth, M., Lobo, C. J., Lysaght, M. J., Vladar, A. E. and Postek, M. T. (2009). Contamination-free imaging by electron induced carbon volatilization in environmental scanning electron microscopy. *J Appl Phys*, **106(3)**. doi:{10.1063/1.3187926}. 32

[28] Toth, M., Uncovsky, M., Knowles, W. R. and Baker, F. S. (2007). Secondary electron imaging at gas pressures in excess of 1 kPa. *Appl Phys Lett*, **91(5)**:053122. 34, 88

[29] Craven, J. P., Baker, F. S., Thiel, B. L. and Donald, A. M. (2002). Consequences of positive ions upon imaging in low vacuum scanning electron microscopy. *Journal Of Microscopy-Oxford*, **205**:96–105. 34

[30] Le Berre, J. F., Demers, H., Demopoulos, G. P. and Gauvin, R. (2007). Examples of charging effects on the spectral quality of X-ray microanalysis on a glass sample using the variable pressure scanning electron microscope. *Scanning*, **29(6)**:270–279. 35

[31] Newbury, D. E. (2002). X-ray microanalysis in the variable pressure (environmental) scanning electron microscope. *Journal Of Research Of The National Institute Of Standards And Technology*, **107(6)**:567–603. 36

[32] Swift, J. A., Brown, A. C. and Saxton, C. A. (1969). Scanning transmission electron microscopy with the Cambridge Stereoscan Mk II. *Journal of Physics E: Scientific Instruments*, **2(8)**:744–746. 37, 44

[33] Buhr, E., Senftleben, N., Klein, T., Bergmann, D., Gnieser, D., Frase, C. G. and Bosse, H. (2009). Characterization of nanoparticles by scanning electron microscopy in transmission mode. *Meas Sci Technol*, **20(8)**:084025 (9pp). URL http://stacks.iop.org/0957-0233/20/084025. 38

[34] Merli, P. G. and Morandi, V. (2005). Low-energy STEM of multilayers and dopant profiles. *Microsc Microanal*, **11(1)**:97–104. 38

[35] Fujita, J., Ikeda, Y., Okada, S., Higashi, K., Nakasawa, S., Ishida, M. and Matsui, S. (2007). In situ visualization of local electric field in an ultrasharp tungsten emitter under a low voltage scanning transmission electron microscope. *Journal Of Vacuum Science & Technology B*, **25(6)**:2624–2627. 38

[36] Glauert, A. M., *Fixation, Dehydration and Embedding of Biological Specimens* (Elsevier Biomedical Press, Amsterdam, The Netherlands, 1987). 39, 101, 103

[37] Kanaya, K. and Okayama, S. (1972). Penetration And Energy-Loss Theory Of Electrons In Solid Targets. *Journal Of Physics D-Applied Physics*, **5(1)**:43–58. 40, 50

[38] Bogner, A., Thollet, G., Basset, D., Jouneau, P. H. and Gauthier, C. (2005). Wet STEM: A new development in environmental SEM for imaging nano-objects included in a liquid phase. *Ultramicroscopy*, **104(3-4)**:290–301. 42, 43, 45, 48, 49, 121, 124

[39] Bogner, A., Jouneau, P. H., Thollet, G., Basset, D. and Gauthier, C. (2007). A history of scanning electron microscopy developments: Towards "wet-STEM" imaging. *Micron*, **38(4)**:390–401. 42, 46, 121

[40] Crawford, B. J. and Liley, C. R. W. (1970). A Simple Transmission Stage Using Standard Collection System In Scanning Electron Microscope. *Journal Of Physics E-Scientific Instruments*, **3(6)**:461–462. 44

[41] Joy, D. C., *Monte Carlo Modeling for Electron Microscopy and Microanalysis* (Oxford University Press, New York, NY, United States, 1995). 52, 53

[42] Joy, D. C. and Luo, S. (1989). An empirical stopping power relationship for low-energy electrons. *Scanning*, **11(4)**:176–180. 52

[43] Bethe, H. (1930). Zur Theorie des Durchgangs schneller Korpuskularstrahlen durch Materie. *Annalen der Physik*, **397**:325–400. doi: 10.1002/andp.19303970303. 52

[44] Joy, D. C. and Joy, C. S. (2006). Scanning electron microscope imaging in liquids - some data on electron interactions in water. *Journal Of Microscopy-Oxford*, **221**:84–88. 52

[45] Mullejans, H., Bleloch, A., Howie, A. and Tomita, M. (1993). Secondary electron coincidence detection and time of flight spectroscopy. *Ultramicroscopy*, **52(3-4)**:360–368. URL http://www.sciencedirect.com/science/article/B6TW1-46D2C6F-R/2/00905e7c41ab687dd40ee6b2de12547f. 52

[46] Williams, S. J. and Donald, A. M. (2004). Investigation of quantitative secondary electron imaging of semiconducting polymer materials using environmental scanning electron microscopy. *Journal Of Microscopy-Oxford*, **216**:241–248. 52, 79

[47] Love, G. and Scott, V. D., *Quantitative Electron-Probe Microanalysis* (John Wiley & Sons, Chichester, UK, 1983). 52

[48] Heinrich, K. F. J. and Newbury, D. E. (eds.), *Electron Probe Quantitation* (Plenum Press, New York, NY, US, 1991). 52

[49] Holt, D. B., Muir, M. D., Grant, P. R. and Boswarva, I. M. (eds.), *Quantitative Scanning Electron Microscopy* (Academic Press, London, UK, 1974). 52

[50] Kalos, M. H. and Whitlock, P. A., *Monte Carlo methods* (Wiley, Chichester, UK, 2008). 53

[51] Drouin, D., Couture, A. R., Joly, D., Tastet, X., Aimez, V. and Gauvin, R. (2007). CASINO V2.42 - A fast and easy-to-use modeling tool for scanning electron microscopy and microanalysis users. *Scanning*, **29(3)**:92–101. 53, 55, 66

[52] Griffin, B. J. (2000). Charge contrast imaging of material growth and defects in environmental scanning electron miscroscopy - Linking electron emission and cathodoluminescence. *Scanning*, **22(4)**:234–242. 56

[53] Pawley, J. B. (ed.), *Handbook of Biological Confocal Microscopy* (Plenum Press, 223 Spring Street, New York, NY, United States, 1995), 2nd edition. 56, 58

[54] Minsky, M. (1988). Memoir on inventing the confocal scanning microscope. *Scanning*, **10(4)**:128–138. 56

[55] Russell, W. C., Newman, C. and Williamson, D. H. (1975). A simple cytochemical technique for demonstration of DNA in cells infected with mycoplasmas and viruses. *Nature*, **253(5491)**:461–462. URL http://dx.doi.org/10.1038/253461a0. 57

[56] Hamley, I. W., *Introduction to soft matter : polymers, colloids, amphiphiles and liquid crystals* (John Wiley and Sons, Baffins Lane, Chichester, West Sussex, PO19 1UD, England, 2000). URL http://search.lib.cam.ac.uk/?itemid=|cambrdgedb|1854134. 59, 71, 74, 83

[57] Houghton, H. A. and Donald, A. M. (2008). An environmental scanning electron microscopy study of aqueous gibbsite suspensions. *Scanning*, **30(3)**:223–227. 60, 65

[58] Wijnhoven, J. E. (2005). Seeded growth of monodisperse gibbsite platelets to adjustable sizes. *J Colloid Interface Sci*, **292(2)**:403 – 409. doi:DOI:10.1016/j.jcis.2005.06.018. URL http://www.sciencedirect.com/science/article/B6WHR-4GNCGBN-6/2/b21ed92770fc5e3e143dc9d9c8b7069a. 60

[59] Houghton, H. A. (2006). *Microstructural Studies of Clay Dispersions and Gels*. Ph.D. thesis, University of Cambridge. 60

[60] Goodhew, P. J., Humphreys, J. and Beanland, R., *Electron Microscopy and Analysis* (Taylor & Francis Ltd, 2001), 3rd edition. 68

[61] Reimer, L., *Transmission Electron Microscopy: Physics of Image Formation and Microanalysis*, volume 36 of *Springer Series in Optical Sciences* (Springer-Verlag, Berlin, Germany, 1993). 68

[62] Dragnevski, K. I. and Donald, A. M. (2008). Microstructural evolution of a novel acrylic latex. *Prog Org Coat*, **61(1)**:63 – 67. doi:DOI:10.1016/j.porgcoat.2007.09.002. URL http://www.sciencedirect.com/science/article/B6THD-4R113KX-1/2/7fd0c55088dcc2f26b6e029807ca2169. 69, 70, 71

[63] Dragnevski, K. I., Routh, A. F., Murray, M. W. and Donald, A. M. (2010). Cracking of Drying Latex Films: An ESEM Experiment. *Langmuir*, **26(11)**:7747–7751. doi:10.1021/la904512q. URL http://pubs.acs.org/doi/abs/10.1021/la904512q. 69

[64] Keddie, J. L., Meredith, P., Jones, R. A. L. and Donald, A. M. (1996). Film formation of acrylic latices with varying concentrations of non-film-forming latex particles. *Langmuir*, **12(16)**:3793–3801. 70

[65] Faucheu, J., Chazeau, L., Gauthier, C., Cavaillé, J.-Y., Goikoetxea, M., Minari, R. and Asua, J. M. (2009). Latex Imaging by Environmental STEM: Application to the Study of the Surfactant Outcome in Hybrid Alkyd/Acrylate Systems. *Langmuir*, **25(17)**:10251–10258. doi:10.1021/la901049h. URL http://pubs.acs.org/doi/abs/10.1021/la901049h. 73

[66] Feldman, D. and Barbalata, A., *Synthetic Polymers - Technology, properties, applications* (Chapman and Hall, London, UK, 1996). 75

[67] Lide, D. R. (ed.), *Handbook of Chemistry and Physics* (CRC Press, Boca Raton, Florida, US, 1991), 72nd edition. 76

[68] Azzam, R. M. A. and Bashara, N. M., *Ellipsometry and Polarized Light* (Elsevier Science Publishers B.V, Amsterdam, The Netherlands, 1987). 76

[69] Glover, B. J. and Whitney, H. M. (2010). Structural colour and iridescence in plants: the poorly studied relations of pigment colour. *Annals of Botany*, **105(4)**:505–511. doi:10.1093/aob/mcq007. URL http://aob.oxfordjournals.org/content/105/4/505.abstract. 77

[70] The European Synchrotron Radiation Facility. URL http://www.esrf.eu/UsersAndScience/Experiments/Beamlines/beamline-snapshot?BeamlineID=ID22NI. 77

[71] Wiesendanger, R., *Scanning Probe Microscopy and Spectroscopy: Methods and Applications* (Cambridge University Press, Cambridge, UK, 1994). 77

[72] Vesely, D. (1996). Microstructural characterization of polymer blends. *Polymer Engineering & Science*, **36(12)**:1586–1593. doi:10.1002/pen.10555. URL http://dx.doi.org/10.1002/pen.10555. 78

[73] Rakhmatullina, E., Braun, T., Chami, M., Malinova, V. and Meier, W. (2007). Self-organization behavior of methacrylate-based Amphiphilic Di- and triblock copolymers. *Langmuir*, **23(24)**:12371–12379. 79

[74] Deng, T., Breen, C., Breiner, T., Swager, T. M. and Thomas, E. L. (2005). A block copolymer nanotemplate for mechanically tunable polarized emission from a conjugated polymer. *Polymer*, **46(23)**:10113–10118. URL http://www.sciencedirect.com/science/article/B6TXW-4H2FY5W-5/2/497921bc1a4a1d120daeeaa43be8d9b6. 79

[75] Drummy, L. F., Yang, J. and Martin, D. C. (2004). Low-voltage electron microscopy of polymer and organic molecular thin films. *Ultramicroscopy*, **99(4)**:247 – 256. doi:DOI:10.1016/j.ultramic.2004.01.011. URL http://www.sciencedirect.com/science/article/B6TW1-4BW9NHM-1/2/612f0bfe90738f4cb20b487d24d3d624. 79, 85

[76] Lee, W. K., Kim, H. D. and Kim, E. Y. (2006). Morphological reorientation by extensional flow deformation of a triblock copolymer styrene-isoprene-styrene. *Current Applied Physics*, **6(4)**:718–722. 79, 84

[77] Watt, G. R., Griffin, B. J. and Kinny, P. D. (2000). Charge contrast imaging of geological materials in the environmental scanning electron microscope. *Am Mineral*, **85(11-12)**:1784–1794. 79

[78] Nitz, H., Semke, H. and Mulhaupt, R. (2001). Influence of lignin type on the mechanical properties of lignin based compounds. *Macromol Mater Eng*, **286(12)**:737–743. 79

[79] Rizzi, S. C., Heath, D. T., Coombes, A. G. A., Bock, N., Textor, M. and Downes, S. (2001). Biodegradable polymer/hydroxyapatite composites: Surface analysis and initial attachment of human osteoblasts. *Journal Of Biomedical Materials Research*, **55(4)**:475–486. 79

[80] Ramsdale, C. M., Bache, I. C., MacKenzie, J. D., Thomas, D. S., Arias, A. C., Donald, A. M., Friend, R. H. and Greenham, N. C. (2002). ESEM imaging of polyfluorene blend cross-sections for organic devices. *Physica E-Low-Dimensional Systems & Nanostructures*, **14(1-2)**:268–271. 79

[81] Callow, J. A., Osborne, M. P., Callow, M. E., Baker, F. and Donald, A. M. (2003). Use of environmental scanning electron microscopy to image the spore adhesive of the marine alga Enteromorpha in its natural hydrated state. *Colloids And Surfaces B-Biointerfaces*, **27(4)**:315–321. 79

[82] Miller, A. F. and Cooper, S. J. (2002). In situ Imaging of langmuir films of nylon-6,6 polymer using environmental scanning electron microscopy. *Langmuir*, **18(4)**:1310–1317. 79

[83] Williams, S. J., Morrison, D. E., Thiel, B. L. and Donald, A. M. (2005). Imaging of semiconducting polymer blend systems using environmental scanning electron microscopy and environmental scanning transmission electron microscopy. *Scanning*, **27(4)**:190–198. 80

[84] Bogner, A., Guimarães, A., Guimarães, R., Santos, A., Thollet, G., Jouneau, P. and Gauthier, C. (2008). Grafting characterization of natural rubber latex particles: wet-STEM imaging contributions. *Colloid & Polymer Science*, **286**:1049–1059. URL http://dx.doi.org/10.1007/s00396-008-1868-0. 80

[85] Rubinstein, M. and Colby, R. H., *Polymer Physics* (Oxford University Press, Oxford, UK, 2005). 80, 81, 83

[86] Matsen, M. W. and Bates, F. S. (1996). Unifying weak- and strong-segregation block copolymer theories. *Macromolecules*, **29(4)**:1091–1098. 83

[87] Brandrup, J., Immergut, E. H. and Grulke, E. A. (eds.), *Polymer Handbook* (John Wiley & Sons Inc., 1999), 4th edition. 84

[88] Niu, S. and Saraf, R. (2003). Stability of Order in Solvent-Annealed Block Copolymer Thin Films. *Macromolecules*, **36(7)**:2428–2440. URL http://pubs3.acs.org/acs/journals/doilookup?in_doi=10.1021/ma0212792. 84

[89] Knoll, A., Magerle, R. and Krausch, G. (2001). Tapping Mode Atomic Force Microscopy on Polymers: Where Is the True Sample Surface? *Macromolecules*, **34(12)**:4159–4165. URL http://dx.doi.org/10.1021/ma001311x. 84

[90] Handlin, D. L. and Thomas, E. L. (1983). Phase contrast imaging of styrene-isoprene and styrene-butadiene block copolymers. *Macromolecules*, **16(9)**:1514–1525. doi:10.1021/ma00243a019. URL http://pubs.acs.org/doi/abs/10.1021/ma00243a019. 84, 92

[91] Iatrou, H. and Hadjichristidis, N. (1992). Synthesis Of A Model 3-Miktoarm Star Terpolymer. *Macromolecules*, **25(18)**:4649–4651. 85

[92] Morton, M. and Fetters, L. J. (1975). Anionic Polymerisation of Vinyl Monomers. *Rubber Chem Technol*, **48**:359. 85

[93] Fukunaga, K., Elbs, H., Magerle, R. and Krausch, G. (2000). Large-scale alignment of ABC block copolymer microdomains via solvent vapor treatment. *Macromolecules*, **33(3)**:947–953. 86

[94] Meyers, G., DeKoven, B., Dineen, M., Strandjord, A., O'Connor, P., Hu, T., Chiao, Y., Pollock, H. and Hammiche, A. (1998). Probing adhesive, mechanical, and thermal properties of polymer surfaces using scanning probe microscopy. *Abstracts of papers of the American Chemical Society*, **216(Part 3)**:592–POLY. 92, 93

[95] Rasband, W. S. (1997-2008). *ImageJ, US National Institutes of Health, Bethesda, Maryland, USA, http://rsb.info.nih.gov/ij/*. 93

[96] Frigo, M. and Johnson, S. G. (2005). The Design and Implementation of FFTW3. **93(2)**:216–231. 93

[97] Spontak, R., Williams, M. and Schooley, C. (1986). Morphology of bulk SBS block copolymers prepared by wet cryo-ultramicrotomy. *J Mater Sci*, **21(9)**:3173–3178. URL http://dx.doi.org/10.1007/BF00553354. 96

[98] Little, B., Wagner, P., Ray, R., Pope, R. and Scheetz, R. (1991). Biofilms - An ESEM Evaluation Of Artifacts Introduced During SEM Preparation. *Journal Of Industrial Microbiology*, **8(4)**:213–221. 101, 115

[99] Uwins, P. J. R., Murray, M. and Gould, R. J. (1993). Effects Of 4 Different Processing Techniques On The Microstructure Of Potatoes - Comparison With Fresh Samples In The ESEM. *Microsc Res Tech*, **25(5-6)**:412–418. 101

[100] Gilpin, C. and Sigee, D. C. (1995). X-Ray Microanalysis of Wet Biological Specimens in the Environmental Scanning Electron-Microscope. 1. Reduction Of Specimen Distance Under Different Atmospheric Conditions. *Journal of Microscopy-Oxford*, **179(Part 1)**:22–28. 101

[101] Attawia, M. A., Uhrich, K. E., Botchwey, E., Fan, M., Langer, R. and Laurencin, C. T. (1995). Cytotoxicity testing of poly(anhydride-co-imides) for orthopedic applications. *J. Biomed. Mater. Res.*, **29(10)**:1233–1240. URL http://dx.doi.org/10.1002/jbm.820291010. 101, 104

[102] Alberts, B., Bray, D., Lewis, J., Raff, M., Roberts, K. and Watson, J. D., *Molecular Biology of the Cell* (Garland Publishing Inc., 717 Fifth Avenue, New York, NY 10022, United States, 1994), 3rd edition. 102, 106, 111, 113, 114, 124, 126

[103] Bleher, R., Kandela, I., Meyer, D. and Albrecht, R. (2008). Immuno-EM using colloidal metal nanoparticles and electron spectroscopic imaging for co-localization at high spatial resolution. *J Microsc*, **230(3)**:388–395. URL http://dx.doi.org/10.1111/j.1365-2818.2008.01997.x. 104

[104] Stokes, D. J., Rea, S. M., Best, S. M. and Bonfield, W. (2003). Electron microscopy of mammalian cells in the absence of fixing, freezing, dehydration, or specimen coating. *Scanning*, **25(4)**:181–184. doi:10.1002/sca.4950250404. URL http://dx.doi.org/10.1002/sca.4950250404. 104

[105] Tai, S. S. W. and Tang, X. M. (2001). Manipulating biological samples for environmental scanning electron microscopy observation. *Scanning*, **23(4)**:267–272. 104

[106] Todaro, G. J. and Green, H. (1963). Quantitative Studies of the Growth of Mouse Embryo Cells in Culture and their Development into Established Lines. *J Cell Biol*, **17(2)**:299–313. URL http://www.jcb.org/cgi/content/abstract/17/2/299. 105

[107] Mogilner, A. and Rubinstein, B. (2005). The Physics of Filopodial Protrusion. *Biophys J*, **89(2)**:782–795. doi:{10.1529/biophysj.104.056515}. 108

[108] Mattila, P. K. and Lappalainen, P. (2008). Filopodia: molecular architecture and cellular functions. *Nat Rev Mol Cell Biol*, **9(6)**:446–454. URL http://dx.doi.org/10.1038/nrm2406. 108

[109] Marko, M., Hsieh, C., Schalek, R., Frank, J. and Mannella, C. (2007). Focused-ion-beam thinning of frozen-hydrated biological specimens for cryo-electron microscopy. *Nat Meth*, **4(3)**:215–217. URL http://dx.doi.org/10.1038/nmeth1014. 113

[110] Graumann, P. L. (2007). Cytoskeletal Elements in Bacteria. *Annu Rev Microbiol*, **61(1)**:589–618. 113, 117, 125, 126, 130, 132

[111] Wiggins, P. A., Cheveralls, K. C., Martin, J. S., Lintner, R. and Kondev, J. (2010). Strong intranucleoid interactions organize the Escherichia coli chromosome into a nucleoid filament. *Proceedings of the National Academy of Sciences*, **107(11)**:4991–4995. doi:10.1073/pnas.0912062107. URL http://www.pnas.org/content/107/11/4991.abstract. 114, 124

[112] Iino, T., Mori, K. and Suzuki, K.-i. (2010). Methanospirillum lacunae sp. nov., a methane-producing archaeon isolated from a puddly soil, and emended descriptions of the genus Methanospirillum and Methanospirillum hungatei. *Int J Syst Evol Microbiol*, **60(11)**:2563–2566. doi:10.1099/ijs.0.020131-0. URL http://ijs.sgmjournals.org/cgi/content/abstract/60/11/2563. 114

[113] Bergmans, L., Moisiadis, P., Van Meerbeek, B., Quirynen, M. and Lambrechts, P. (2005). Microscopic observation of bacteria: review highlighting the use of environmental SEM. *International Endodontic Journal*, **38(11)**:775–788. doi:10.1111/j.1365-2591.2005.00999.x. URL http://dx.doi.org/10.1111/j.1365-2591.2005.00999.x. 115

[114] Darkin, M. G., Gilpin, C., Williams, J. B. and Sangha, C. M. (2001). Direct wet surface imaging of an anaerobic biofilm by environmental scanning electron microscopy: Application to landfill clay liner barriers. *Scanning*, **23(5)**:346–350. 115

[115] Ezra, D., Castillo, U. F., Strobel, G. A., Hess, W. M., Porter, H., Jensen, J. B., Condron, M. A. M., Teplow, D. B., Sears, J., Maranta, M., Hunter, M., Weber, B. and Yaver, D. (2004). Coronamycins, peptide antibiotics produced by a verticillate Streptomyces sp. (MSU-2110) endophytic on Monstera sp. *Microbiology*, **150(4)**:785–793.

doi:10.1099/mic.0.26645-0. URL http://mic.sgmjournals.org/cgi/content/abstract/150/4/785. 115

[116] Castillo, U., Myers, S., Browne, L., Strobel, G., Hess, W. M., Hanks, J. and Reay, D. (2005). Scanning electron microscopy of some endophytic streptomycetes in snakevine-Kennedia nigricans. *Scanning*, **27(6)**:305–311. doi:10.1002/sca.4950270606. URL http://dx.doi.org/10.1002/sca.4950270606. 115

[117] Akaraonye, E., Keshavarz, T. and Roy, I. (2010). Production of polyhydroxyalkanoates: the future green materials of choice. *J Chem Technol Biotechnol*, **85(6)**:732–743. URL http://dx.doi.org/10.1002/jctb.2392. 116

[118] Thomson, N., Roy, I., Summers, D. and Sivaniah, E. (2010). In vitro production of polyhydroxyalkanoates: achievements and applications. *Journal of Chemical Technology & Biotechnology*, **85(6)**:760–767. URL http://dx.doi.org/10.1002/jctb.2299. 116

[119] Datsenko, K. A. and Wanner, B. L. (2000). One-Step Inactivation of Chromosomal Genes in Escherichia coli K-12 Using PCR Products. *Proc Natl Acad Sci U S A*, **97(12)**:6640–6645. URL http://www.jstor.org/stable/122690. 117

[120] Rigg, G. P., Barrett, B. and Roberts, I. s. (1998). The localization of KpsC, S and T, and KfiA, C and D proteins involved in the biosynthesis of the Escherichia coli K5 capsular polysaccharide: evidence for a membrane-bound complex. *Microbiology*, **144(10)**:2905–2914. doi:10.1099/00221287-144-10-2905. URL http://mic.sgmjournals.org/cgi/content/abstract/144/10/2905. 118

[121] Karlyshev, A. V., Linton, D., Gregson, N. A., Lastovica, A. J. and Wren, B. W. (2000). Genetic and biochemical evidence of a Campylobacter jejuni capsular polysaccharide that accounts for Penner serotype specificity. *Mol Microbiol*, **35(3)**:529–541. doi:10.

1046/j.1365-2958.2000.01717.x. URL http://dx.doi.org/10.1046/j.1365-2958.2000.01717.x. 118, 135

[122] Hudock, J. F., Borger, A. C. and Kaspar, C. W. (2005). Temperature-Dependent Genome Degradation in the Coccoid Form of *Campylobacter jejuni*. *Curr Microbiol*, **50**:110–113. URL http://dx.doi.org/10.1007/s00284-004-4400-x. 119, 137, 138

[123] Thomson, N. M., Channon, K., Mokhtar, N. A., Staniewicz, L., Rai, R., Roy, I., Sato, S., Tsuge, T., Donald, A. M., Summers, D. and Sivaniah, E. (2011). Imaging internal features of whole, unfixed bacteria. *Scanning*, **33(2)**:59–68. doi:10.1002/sca.20221. URL http://dx.doi.org/10.1002/sca.20221. 122

[124] Peckys, D. B., Veith, G. M., Joy, D. C. and de Jonge, N. (2009). Nanoscale Imaging of Whole Cells Using a Liquid Enclosure and a Scanning Transmission Electron Microscope. *PLOS ONE*, **4(12)**. doi:{10.1371/journal.pone.0008214}. 122

[125] Pilhofer, M., Ladinsky, M. S., McDowall, A. W. and Jensen, G. J., Bacterial TEM: New Insights from Cryo-Microscopy. In T. Müller-Reichert (ed.), *Electron Microscopy of Model Systems*, volume 96 of *Methods in Cell Biology*, pp. 21 – 45 (Academic Press, 2010). doi:DOI:10.1016/S0091-679X(10)96002-0. URL http://www.sciencedirect.com/science/article/B7CV1-51333RY-8/2/21fb1e05263775294ee337e3bb47b93c. 124

[126] Guthrie, S. (2008). *Exploration of the use of ESEM for the study of biological materials*. Ph.D. thesis, University of Cambridge. 126, 133, 139

[127] Pederson, E. N. and Srienc, F. (2004). Mass spectrometry feedback control for synthesis of polyhydroxyalkanoate granule microstructures in Ralstonia eutropha. *Macromol Biosci*, **4(3)**:243–254. doi:{10.1002/mabi.200300137}. 128

[128] Schlegel, H. G., Lafferty, R. and Krauss, I. (1970). The isolation of mutants not accumulating poly-B-hydroxybutyric acid. *Arch Microbiol*, **71**:283–294. URL http://dx.doi.org/10.1007/BF00410161. 129

[129] White, C. L., Kitich, A. and Gober, J. W. (2010). Positioning cell wall synthetic complexes by the bacterial morphogenetic proteins MreB and MreD. *Mol Microbiol*, **76(3)**:616–633. URL http://dx.doi.org/10.1111/j.1365-2958.2010.07108.x. 132

[130] Gaynor, E. C., Cawthraw, S., Manning, G., MacKichan, J. K., Falkow, S. and Newell, D. G. (2004). The Genome-Sequenced Variant of Campylobacter jejuni NCTC 11168 and the Original Clonal Clinical Isolate Differ Markedly in Colonization, Gene Expression, and Virulence-Associated Phenotypes. *J Bacteriol*, **186(2)**:503–517. doi:10.1128/JB.186.2.503-517.2004. URL http://jb.asm.org/cgi/content/abstract/186/2/503. 132, 135

[131] Ziprin, R. L., Hume, M. E., Andrews, K., Droleskey, R. E., Harvey, R. B. and Sheffield, C. L. (2005). News and Notes: An Atypical *Campylobacter coli* Exhibiting Unusual Morphology. *Curr Microbiol*, **51**:161–163. URL http://dx.doi.org/10.1007/s00284-005-4527-4. 132, 135

[132] Buck, G. E., Parshall, K. A. and Davis, C. P. (1983). Electron microscopy of the coccoid form of Campylobacter jejuni. *J. Clin. Microbiol.*, **18(2)**:420–421. URL http://jcm.asm.org/cgi/content/abstract/18/2/420. 132, 136, 138

[133] Karlyshev, A. V., McCrossan, M. V. and Wren, B. W. (2001). Demonstration of Polysaccharide Capsule in Campylobacter jejuni Using Electron Microscopy. *Infect Immun*, **69(9)**:5921–5924. doi:10.1128/IAI.69.9.5921-5924.2001. URL http://iai.asm.org/cgi/content/abstract/69/9/5921. 133

[134] McCoy, E. C., Doyle, D., Wiltberger, H., Burda, K. and Winter, A. J. (1975). Flagellar ultrastructure and flagella-associated antigens of Campylobacter fetus. *J Bacteriol*, **122(1)**:307–315. URL http://jb.asm.org/cgi/content/abstract/122/1/307. 134